Materials Advances

ROYAL SOCIETY OF CHEMISTRY

REVIEW

View Article Online
View Journal | View Issue



Cite this: *Mater. Adv.*, 2025, 6, 39

# Highly conductive and stable electrolytes for solid oxide electrolysis and fuel cells: fabrication, characterisation, recent progress and challenges

Jing Li, Qiong Cai and Bahman Amini Horri *

Hydrogen fuel cells and hydrogen production stand at the forefront of efforts to achieve net-zero emissions. Among these technologies, solid oxide fuel cells (SOFCs) and electrolysers (SOEs) are distinguished as particularly promising for broad practical application, offering superior efficiency, robust stability, cost-effectiveness, and inherent safety. Lowering the operating temperature can significantly facilitate their commercialization by improving the stability and reducing the costs associated with electrodes and the fabrication process. Furthermore, reducing the operating temperature to 600 °C enables the utilization of heat sources from industrial processes, such as steel production or various combustion systems, effectively enhancing energy recycling efficiency. At low and intermediate temperatures, SOFCs and SOECs' performance heavily relies on electrolyte conductivity. Therefore, rationally improving electrolyte conductivity under a relatively low temperature plays an important role in facilitating the widespread application of SOFCs and SOECs on a large scale. Aimed at practical application, this work delivers an extensive review of cutting-edge modification strategies intended to enhance the conductivity of several promising electrolytes and outlines the characterisation methods utilised to assess their properties. It further investigates novel synthesis techniques aimed at reducing the sintering temperature. Moreover, this paper provides a comprehensive analysis and evaluation of electrolytes tailored for large-scale implementation in SOFCs and SOECs.

Received 6th July 2024,
Accepted 1st November 2024

DOI: 10.1039/d4ma00690a

rsc.li/materials-advances



## 1. Introduction

The ever-deteriorating air quality and the issue of global warming have underscored the necessity for clean and sustainable energy. Hydrogen-based fuels are widely acknowledged as an environmentally friendly and renewable energy source among various alternatives due to their high energy density and pollution-free product. Specifically, it is a promising alternative to conventional fossil fuels due to the highest gravimetric energy density (143 kJ $kg^{-1}$) compared to all other chemical-based fuels.[1] Furthermore, their transportable and storable properties make them capable of meeting the growing energy demand. Therefore, the commercialization of hydrogen production and the widespread application of hydrogen fuel cells hold the potential to significantly contribute to achieving net-zero emissions. Hydrogen can be generated through various methods such as natural gas reforming,[2] methane cracking,[3] coal gasification, and oil processing, but these methods can produce $CO_2$ or CO by-products, which are not ideal unless the carbon dioxide can be captured and utilised as a raw material. Photocatalysis and electrolysis, each harnessing different principles and technologies to split water into hydrogen and oxygen, are two prominent green pathways for hydrogen production. The highest solar energy conversion efficiency achieved through photocatalytic solar water splitting is around 2.0%,[4] while commercial hydrogen production through water electrolysis achieves 70–75% efficiency.[5] Electrolysis is a more effective technology for green hydrogen and is expected to play a crucial role in future energy, serving as a vital bridge between the electric, gas, and thermal grids. However, low-temperature water electrolysis processes (<100 °C), such as those based on polymer electrolyte membranes (PEMs) and alkaline water electrolysis, necessitate substantial electricity consumption and the use of noble metal catalysts, leading to lower efficiency and higher costs.[6] In contrast, solid oxide electrolyser (SOE) technology emerges as a promising alternative, characterised by its high-efficiency water-splitting capabilities and lower cost for large-scale hydrogen production.

There are two types of SOEs according to the different electrolytes, *i.e.* oxygen ions-conducting cells (O-SOECs) and protonic conducting cells (H-SOECs, also named PCECs) which are designed to operate at lower temperatures (450–750 °C) but remain in the development phase.[7] Key parts of H-SOECs

*School of Chemistry and Chemical Engineering, University of Surrey, Guildford, GU2 7XH, UK. E-mail: b.aminihorri@surrey.ac.uk*

(electrolyte and electrode) have been summarised in the previous review, including the operating principles and requirements of materials.[7,8] The main electrolytes are based on doped $BaCeO_3$ and $BaZrO_3$ are normally used as the electrolytes due to thermodynamic stability and protonic conductivity.[9,10] This review briefly summarised four types of protonic electrolytes, including recent development of dopants, protonic defects, challenges and possible solutions.

O-SOECs typically operate at high temperatures ($>800$ °C), due to the electrolyte limitation, in which YSZ ($Y_2O_3$ stabilised $ZrO_2$) is currently the most popular electrolyte used for SOEC at high temperatures due to its good combination of ionic conductivity and stability.[11] Furthermore, the power-to-fuel efficiency can reach up to approximately 100%, attributed to high reaction rates and favourable thermodynamics at elevated temperatures, where both electricity and heat are utilised efficiently.[12] Additionally, the higher operating temperatures contribute to reduced ohmic resistances, offering an advantage over systems using polymer electrolyte membranes and alkaline water electrolysis. It is reported that the industrial SOEC can produce 200 $Nm^3\ h^{-1}$ green $H_2$ with an electrical efficiency of $84\%_{el,LHV}$ and a nominal power input of 720 kW.[13]

A solid oxide electrolyser can be reversed to become a solid oxide fuel cell (SOFC) that uses fuel to generate electrical power, with the advantages of fuel flexibility (hydrocarbons, water and liquid alcohols) and high energy conversion.[14,15] A single SOFC consists of a dense electrolyte, a porous fuel electrode and an oxidant electrode. The schematics and reactions of SOECs and SOFCs to produce and utilise hydrogen energy are shown in Fig. 1a and b. During electrolysis for SOECs, steam or $CO_2$ gas is fed to the cathode where the gas is reacted into $H_2$ or CO and the $O^{2-}$ ions which disperse through the electrolyte to the anode. At the anode, the $O^{2-}$ ions are oxidised to $O_2$ and the synchronously generated electrons are transferred from the anode to the cathode *via* the external circuit.[16] The fuel cell reactions are a reverse reaction of SOECs, where oxide molecules are reduced to oxide ions at the cathode, and oxide ions diffuse through the electrolyte and react with $H_2$ or CO to produce the $H_2O$ at the anode.[17] Since the electrolyte is non-electron conductive, the generated electrons are pushed from the anode to the cathode, which can bring about the generation of electrical power.[17] The electrochemical reaction between hydrogen (fuel) and oxygen can be presented in the following equation:[18]

$$H_2 + \frac{1}{2}O_2 \rightarrow H_2O + \dot{W} + \dot{Q} \quad (1)$$

where $\dot{W}$ is the electric power and $\dot{Q}$ is the waste heat, which are produced during reaction.

Compared with operating at high temperatures ($>800$ °C), lowering the temperature, SOFC technologies have a broader and cheaper range of materials, more cost-effective SOFC fabrication[19] and good durability, which typically operates between 600 and 800 °C. The reduction in operating temperature has also been explored in the field of SOECs in a limited number of experimental projects reported over the recent decades,[6,20,21] where the temperature has decreased from 1000 to 800 °C. Lowering the operating temperatures is a practical approach to enhance the stability and reduce the costs of SOECs and SOFCs, enhancing the durability and decreasing the start-up time.[15] Besides, the stack design also relies on the densified electrolyte. The primary function of the electrolytes is to transport oxygen ions or protons, depending on the specific type, which is similar for both SOECs and SOFCs. In order to obtain high electrolysis efficiency and stability, wide application, the operation temperature should be around 500–800 °C. Electrolytes should satisfy requirements, including good densification with negligible gas permeability to separate the $H_2$ and $O_2$; they also should be chemically stable and have high ionic conductivity to achieve high current efficiencies.[22,23] Besides, the electrolyte should be as thin as possible with good mechanical properties to decrease the ohmic overpotential, and the thermal expansion coefficients of the anode and cathode should be close to the electrolyte to minimise mechanical stress.[11] Chemically induced stress also plays a vital role in mechanical fracture, which is subject to a gradient of oxygen potential and results in the delamination of electrolytes at the SOECs' anode.[24] There are two basic approaches to improving the performance of flat-plate cells: to use electrolytes with higher ionic conductivity or to improve the mechanical strength with thinner thickness.

VOSviewer was used to qualitatively analyse the network of the published records for the period between 2010 and 2023 in solid oxide electrolytes.[25] Fig. 1c summarises the results of this analysis representing the main keywords appearing at least 10 times in literature. The size of each circle indicates its significance in the literature, while the distance between keywords suggests relativity and the possibility of co-occurrence.[26] The most frequent keyword related to SOECs is 'performance', which can be improved by addressing the degradation issue, enhancing the microstructure, using suitable electrode materials and fabrication methods, and improving the performance and stability of SOFCs. Other essential keywords considered were the 'fabrication' aspects of the thin films and depositions of YSZ electrolytes ('electrolyte') and those related to the densification and microstructure and chemical stability and ionic conductivity, 'temperature', which is related to the degradation and fabrication and electrochemical performance'cathode'. Operating at high operation temperatures of 600–900 °C can achieve high energy conversation efficiency with fast reaction kinetics.[1] Moreover, these keyword clusters have shown specific thin film fabrication methods, such as pulsed-laser deposition, electrophoretic deposition, spray pyrolysis, tape casting, magnetron sputtering, and vapour deposition, which implies the deposition of thin film with nano-size are more popular recently, in order to decrease the thickness of electrolyte and improve the conductivity.

In the literature, many works have been conducted to improve the ionic conductivity for the different electrolytes, including zirconia-based oxides,[27] $Bi_2O_3$-based electrolytes,[28] ceria-based oxides,[29] and the perovskite-type electrolyte system.[30] Two types of zirconia-based electrolytes are studied frequently, *i.e.* yttria-stabilised-$ZrO_2$ (YSZ) and $Sc_2O_3$-stabilised $ZrO_2$ (ScSZ), due to attractive ionic conductivity and stability at

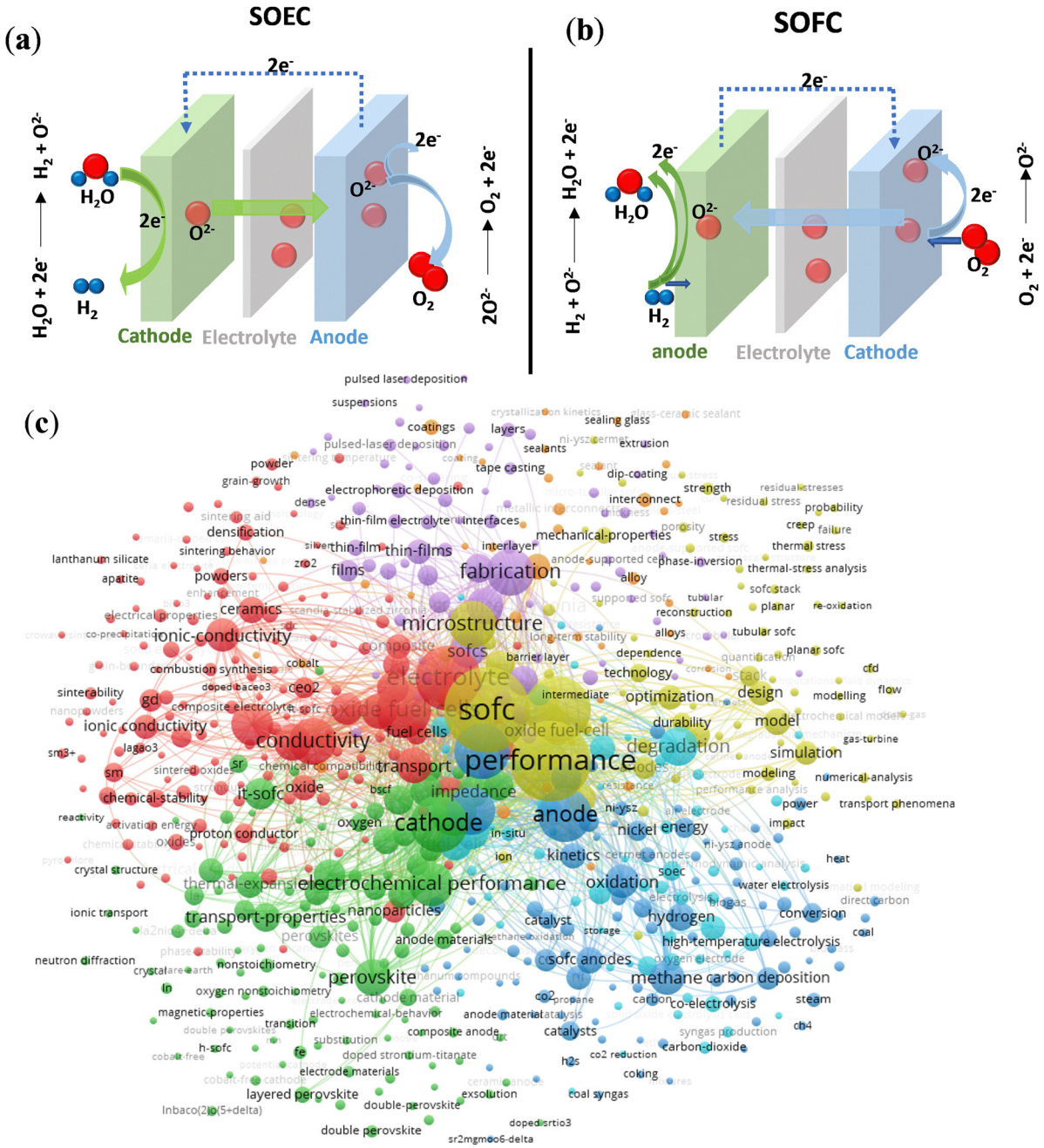


Fig. 1 (a) The overview of main keyword clusters in solid oxide electrolytes, representing the primary subfield. (b) The schematics and reactions of SOECs to produce hydrogen and oxygen; (c) the schematics and reactions of SOFCs to utilise hydrogen to produce electricity.

high temperatures (>800 °C).[31] Unfortunately, YSZ is not suitable for operating at low-to-intermediate temperatures, due to its low conductivity at these temperatures. Some works can be found to modify YSZ with enhancement conductivity for operating at lower temperatures.[32,33] The Main method is to reduce the thickness of YSZ for minimising ohmic resistance or using an alternative electrolyte, such as a ceria-based electrolyte.[34,35] Gadolinia-doped ceria or $LaGaO_3$-based materials have been considered for lower temperatures applications, due to higher ionic conductivity compared to YSZ.[31] Doping and bi-layer methods are used to improve the stability in reduction conditions by avoiding the reduction of $Ce^{4+}$ into $Ce^{3+}$ and preventing from introducing the electronic conductivity inside the cell, which is the main issue for the practical development of ceria-based electrolyte.[36] Co-doping Sr and Mg into $LaGaO_3$ is the most interesting system, in which the composition of $La_{0.8}Sr_{0.2}Ga_{0.85}Mg_{0.15}O_{2.825}$ can achieve high conductivity of 0.14 S $cm^{-1}$ at 800 °C and is four times of YSZ.[37] However, the literature also mentioned the loss of the Ga oxide sintering process and mechanical issues like bending strengths, which require solving for the SOFC applications.[37,38]

In this paper, we elaborate on the recent development and challenges of electrolytes in SOECs and SOFCs. A novel conclusion of the synthesis method is provided to decrease the sintering temperature of electrolytes with distinct preparation steps. Moreover, the decrease in thickness of the electrolyte is essential to decrease the ohmic resistance, we compare different deposition methods to obtain the electrolyte film from nano to micro thickness with limitations and strengths and ink compositions, with emphasis on the thin film *via* CVD and PVD method. Moreover, this review specifically summarises the various types of electrolytes, including protonic and oxygen ions, comparing the influence of crystal structure with different dopants, emphasising strategies for the enhancement of conductivity at lower operating temperatures in principles. Thermomechanical and thermo-electrochemical characteristics of solid electrolytes are summarised in this paper for the characterisation reference. More importantly, we have examined the electrolyte used in the ~kW stack from the laboratory scale to current commercial applications.

## 2. The development of solid-state electrolyte

There are two types of SOECs: oxygen ions conducting and proton conducting, depending on the different types of electrolytes, O-SOECs and H-SOECs, respectively. The working principles of O-SOECs and H-SOECs, as shown in Fig. 2a and b, are different. When external electricity is applied to O-SOECs, the mobile oxygen ions are generated from the fuel electrode and then diffuse across the electrolyte to the air electrode to produce oxygen. On the other hand, in H-SOECs, the mobile protons are transferred from the air electrode through the electrolyte to the fuel electrode to produce hydrogen at the fuel electrode. As a result, steam is fed to the fuel electrode for O-SOECs and the air electrode for H-SOECs. To obtain pure hydrogen from O-SOECs, an additional process is needed to collect the dry hydrogen at the fuel electrode. In contrast, pure $H_2$ could be obtained directly at the fuel electrode in H-SOECs, which could simplify the process. For the SOFC, there are also two types depending on the electrolytes (oxygen ions conducting and proton conducting) similar to SOECs, *i.e.*, O-SOFCs and H-SOFCs. The difference is the feedstock gas, $H_2$ gas is fed to the fuel electrode for both O-SOFCs and H-SOFCs, and the steam can be produced at the fuel electrode and air electrode, respectively.

### 2.1. Proton-conducting electrolyte materials for SOECs and SOFCs

Scholars have shown a growing interest in proton-conducting electrolytes (H-SOECs and H-SOFCs) that could operate at temperatures between 400 and 600 °C. The migration energy for the proton-conducting electrolytes is between 0.3 and 0.5 eV, which is lower than for oxide-conducting electrolytes (0.8–0.9 eV).[39] As a result, H-SOECs exhibit higher conductivity than O-SOECs within this temperature range. Furthermore, the durability of H-SOECs should be superior to O-SOECs, since the lower operating temperature of H-SOECs could mitigate corrosion or contamination.[40] The stability and high conducting of H-SOECs depend on two key factors: the relationship between the formation and mobility of protonic defects and the thermodynamic stability of oxides; as well as the structure and chemical parameters of electrolyte and electrodes.[39]

**2.1.1. Perovskite type of electrolyte in H-SOECs and H-SOFCs.** Perovskite-type oxides are characterised by high proton conductivity and crystallographic structure $ABO_3$, in which the A-site is occupied by divalent alkaline-earth metal ions like $Ba^{2+}$, $Sr^{2+}$, while the tetravalent cation is in the B-site (*e.g.*, $Zr^{4+}$, $Ce^{4+}$) doped with trivalent ions to format the defects and vacancies. The crystal structure is composed of $BO_6$ octahedra connected to $AO_{12}$ polyhedral in a face-centred cubic lattice system in Fig. 3a. There are three structural degrees of freedom in perovskites: (a) movements of cations A and B in their polyhedral; (b) distortions of the anionic polyhedral; and (c) the $BO_6$ octahedra tilting.[9] The structure is governed by the size of A, B, and O ions. The Goldschmidt tolerance factor

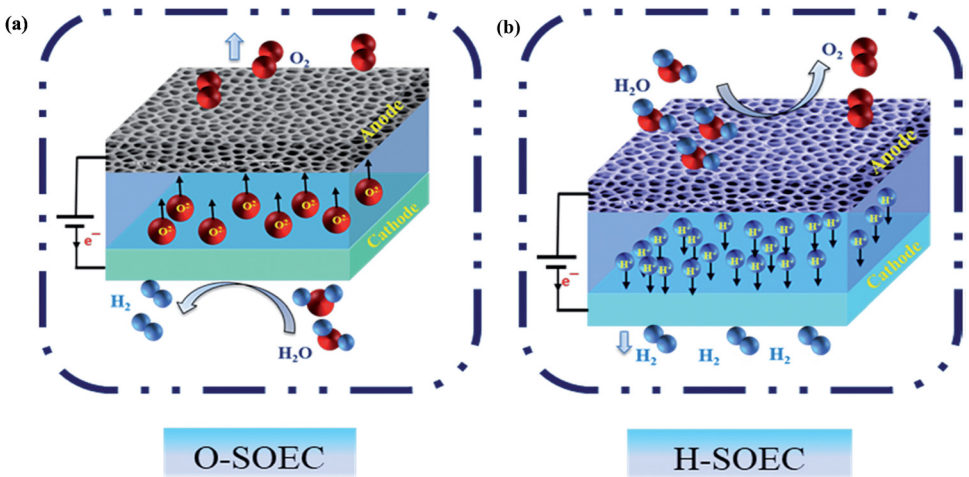


Fig. 2 (a) Schematic images of water splitting by electrolysis with different electrolytes. (a) Using oxygen ion conducting electrolyte in an O-SOEC and (b) using proton conducting electrolyte in H-SOEC. Reproduced from ref. 39 with permission from [Royal Society of Chemistry], copyright [2018].

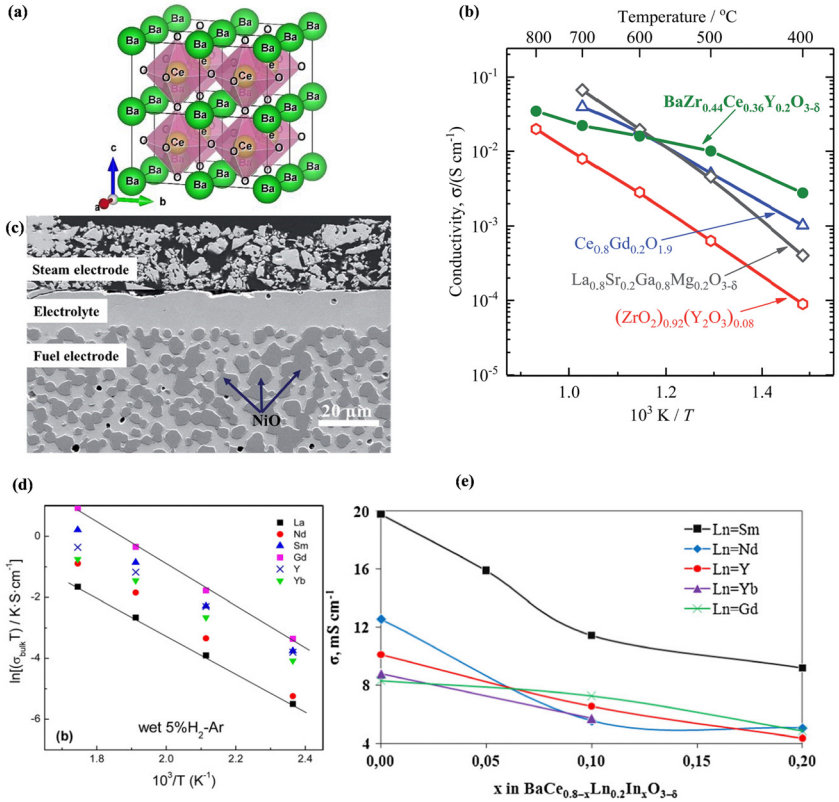


Fig. 3 (a) An ideal $BaCeO_3$ perovskite structure (space group: $Fm\bar{3}m$); (b) comparison of the conductivity of proton electrolyte $BaZr_{0.44}Ce_{0.36}Y_{0.2}O_{3-\delta}$ and oxygen ions electrolyte; (c) cross-sectional imaging of the H-SOEC fabricated by screen printing. (d) Arrhenius plots of the grain boundary resistance for $BaCe_{0.9}Ln_{0.1}O_{3-\delta}$ samples under wet 5% $H_2$-Ar. (e) The grain conductivity of $BaCe_{0.8-x}In_xLn_{0.2}O_{3-\delta}$ under 5% $H_2$/Ar + $H_2O$ at 600 °C. Reproduced from ref. 43 with permission from [APS], copyright [2012]. Reproduced from ref. 39 with permission from [Royal Society of Chemistry], copyright [2018]. Reproduced from ref. 44 with permission from [Elsevier], copyright [2011]. Reproduced from ref. 45 with permission from [Elsevier], copyright [2016].

($t$) given as $t = (r_A + r_B)/[2(r_B + r_O)^{1/2}]$ is used to determine the composition to adapt the perovskite structure, where $r_A$, $r_B$, and $r_O$ are the ionic radius of respective ions. For the ideal cubic perovskite structures, $t$ is unity, and some distortions of perovskite structures could be formed with a slight increase up to 1.04 or decrease down to 0.71.[41] Furthermore, other factors also play a vital role in determining the perovskite structures, such as the metal–metal interactions, degree of covalence, and Jahn–Teller.[42] The formula $(Sr/Ba)(Ce/Zr)_{1-x}M_xO_{3-\delta}$ is used to represent these materials, where M represents a trivalent rare-earth ion and $\delta$ is the oxygen deficiency. $SrCeO_3$- and $BaCeO_3$-based materials with high proton conductivities were discovered and tested in various electrochemical cells.[39]

**2.1.2. Formation of protonic defects.** The protonic defects could be formed in the wet atmosphere, where the water dissociates into a hydroxide ion and a proton; the hydroxide ion fills an oxygen ion vacancy, and the proton forms a covalent bond with lattice oxygen by the following eqn (2) which is hydration process.[39]

$$H_2O + V_O^{\bullet\bullet} + O_O^{\times} \leftrightarrow 2OH_O^{\bullet} \quad (2)$$

where $OH_O^{\bullet}$ represents two positive charged protonic defects, $V_O^{\bullet\bullet}$ is the two positive oxygen ion vacancy. The protonic defects can diffuse in electrolytes accompanied by the counter diffusion of $V_O^{\bullet\bullet}$. This reaction is exothermic, thereby the concentration of protonic defects decreases with the increasing in operation temperatures.

**2.1.3. Advanced proton conducting solid electrolytes for H-SOECs.** Electrolyte materials used in H-SOECs must meet specific requirements, including exhibiting reasonable protonic and negligible electronic conductivity, as well as chemical stability in both reductive (fuel electrode side) and oxidative atmosphere (air electrode side). Moreover, the electrolyte materials should be chemically and physically compatible with the electrodes. There are two main mechanisms for proton conduction: vehicle and Grotthuss (also known as hopping or structural diffusion). In the vehicle mechanism, water is dissociated in protonic species ($H_3O^+$) and hydroxide ($OH^-$), acting as a "vehicle" that carries the proton. This movement is relatively low compared to the Grotthuss mechanism since it requires the entire molecular entity to move.[43] This is commonly observed in solvent-rich system at temperatures below 100 °C. As shown in Fig. 4, the transport mechanism in these perovskite materials follows the Grotthuss-type conduction. This process involves the rotational movement of protonic defect around an oxygen ion, followed by the transfer of a proton to a neighbouring oxygen ion through the formation of a chemical bond. In this way, protons can diffuse over long distances, while the oxygen ions remain

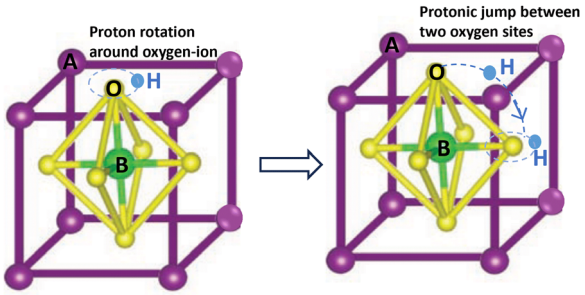


Fig. 4 Schematic representation of Grotthuss mechanism for proton mechanism.

fixed in their crystallographic positions.[44] The rate of proton conduction is determined by the frequency of proton jumps between oxygen sites.

The most extensively researched perovskite oxides for use in the electrolytes of H-SOECs are $BaCeO_3$-, $BaZrO_3$-, $SrCeO_3$-, and $SrZrO_3$-based materials. This section will focus on these systems to briefly overview reported materials and improvements. Cubic perovskite $BaCeO_3$ has been found to exhibit well-mixed oxide and protons conductivity, making it a potential candidate for use in the electrolysers for hydrogen production at intermediate temperatures (500–750 °C), due to its highest level of total proton conductivity with high basicity. The oxygen vacancies could be generated by doping different acceptor oxides ($R_2O_3$ or RO), which results in the formation of the $V_O^{\bullet\bullet}$ and protonic defects as shown in eqn (3) and (4) along with the $BaCe_{1-x}R_xO_{3-\delta}$ system.

$$R_2O_3 \xrightarrow{BaCeO_3} 2R'_{ce} + V_O^{\bullet\bullet} + 2Ba_{Ba}^{\times} + 5O_O^{\times} \quad (3)$$

$$RO \xrightarrow{BaCeO_3} R''_{ce} + V_O^{\bullet\bullet} + Ba_{Ba}^{\times} + 2O_O^{\times} \quad (4)$$

where $R_2O_3$ and RO are trivalent and bivalent oxides; $O_O^{\times}$, $Ba_{Ba}^{\times}$ and $Ce_{Ce}^{\times}$ represents that the atoms are in the normal lattice sites; $V_O^{\bullet\bullet}$, $R'_{ce}$ and $R''_{ce}$ are the oxygen ion vacancies and negatively charged impurity ions located in the Ce-site. In 1998, Y-doped $BaCeO_3$ was found to have excellent proton conductivity.[45] Gu *et al.* reported that the total conductivity of $BaCe_{0.85}Y_{0.15}O_{3-\delta}$ (BCY) was $2.07 \times 10^{-2}$ S cm$^{-1}$ in air and $2.11 \times 10^{-2}$ S cm$^{-1}$ in wet hydrogen (4% $H_2O$-saturated $H_2$) at 500 °C, but its chemical stability was not good under $H_2O$ and $CO_2$ for BCY.[46] Lanthanide series dopants have been studied such as Pr,[45] Nd,[47] Sm,[48] Eu,[49] Gd,[50] Tb,[51] Dy,[52] Ho,[53] Er,[54] Tm,[55] Yb,[56] and Lu,[57] and labelled as $BaCe_{1-x}Ln_xO_{3-\delta}$. The influence of dopants is complicated on the conductivity of $BaCe_{1-x}Ln_xO_{3-\delta}$, as it depends on the atoms in A and B and their position in the $ABO_3$ perovskite structure. Conductivity increases as the decrease in the electronegativity of A or B compound.[58] It was proved that the enthalpy of protonic defect formation declines with decreasing electronegativity.[39] The electronegativity of Ba and Ce ions is smaller than Sr and Zr ions. Consequently, $BaCeO_3$ electrolytes exhibit higher conductivity in the (Sr/Ba)(Zr/Ce)$O_3$ system. In the $BaCe_{1-x}Ln_xO_{3-\delta}$ system, the conductivity increases with an increase of $x$ up to 0.25. The introduction of low concentration of $Ln_2O_3$ dopants leads to the formation of oxygen vacancies, as expressed in eqn (3). Among other lanthanides, $BaCe_{0.9}Gd_{0.1}O_{3-\delta}$ samples exhibited the highest conductivity with a value of 0.02 S cm$^{-1}$ at 600 °C, as depicted in Fig. 3d.[59]

$BaCeO_3$ has been extensively investigated for double-cation doping, with one cation promoting high ionic conductivity and another enhancing structural stability. Co-doping Ti (0–0.3) and Y (0.05, 0.1, and 0.2) into $BaCeO_3$ has been found to improve the stability under moist conditions,[60] and the highest proton conductivity can be found in the sample $BaCe_{0.75}Ti_{0.05}Y_{0.2}O_{3-\delta}$ with a value of $2.52 \times 10^{-3}$ S cm$^{-1}$ at 650 °C in $H_2$ + 3% $H_2O$.[61] Substituting the Y with In or Sm, the stability could be improved, but the In-doped sample had the worst electrical performance compared with the Ln-doped system.[62] Many works also studied co-doping with In and rare-earth ions ($Y^{3+}$, $Ln^{3+}$) to regulate the stability and protonic conductivity. $BaIn_{0.3-x}Y_xCe_{0.7}O_{3-\delta}$ ($x$ = 0, 0.1, 0.2, 0.3) samples were prepared using a modified Pechini method with improved chemical stability and conductivity, in which the sample $BaIn_{0.1}Y_{0.2}Ce_{0.7}O_{3-\delta}$ showed acceptable stability and relatively high conductivity with a value of $1.33 \times 10^{-2}$ S cm$^{-1}$ in wet nitrogen at 800 °C.[63] The Sm- and In-co-doped $BaCe_{0.80-x}Sm_{0.20}In_xO_{3-\delta}$ samples also had good stability, but the electrical conductivity decreased in wet 5% $H_2$/Ar and wet atmosphere due to a decrease in lattice volume with the In doping and thus caused an increase in activation energy $E_a$ for the proton conduction.[64] The same decrease for the samples $BaCe_{0.80-x}Sm_{0.20}Ln_xO_{3-\delta}$ (Ln = Gd, Y, Nd, Yb) can also be detected in a humid reducing atmosphere in Fig. 3e.[64]

Co-doping with other ions could improve the stability, Yan *et al.* studied that $BaZr_{0.1}Ce_{0.7}Y_{0.2}O_{3\pm\delta}$ could operate at high temperatures with good stability as SOFC but degrade in the air at room temperature.[65] $BaCe_{0.8}Y_{0.15}Nd_{0.05}O_{3-\delta}$ (BCYN5) electrolyte had the highest electrical conductivity among different doping amounts for $Y^{3+}$ and $Nd^{3+}$, which showed a high peak power density of 660 mW cm$^{-2}$ at 700 °C with a low ohmic resistance of 0.28 Ω cm$^2$ and resulted from the decreasing in bulk and grain-boundary resistances.[66] Zirconates demonstrate good chemical stability in a wet atmosphere, and introducing Zr ions in $BaCeO_3$ can enhance their stability to a certain extent. However, even with Zr-doping, $BaCeO_3$ fails to completely stabilise the $BaCeO_3$ in high humidity for a long time, which formed $Ba(OH)_2{\cdot}8H_2O$ impurity after 110 h of operation since the cathode delamination from the electrolyte.[67] Yang *et al.* also reported that $BaCe_{0.8-x}Zr_{0.2}In_xO_{3-\delta}$ ($x$ = 0–0.4) electrolytes were unstable in moist air at 1023 K for 60 h.[68]

The $BaZrO_3$-based electrolyte has good chemical stability in a high concentration of $H_2O$, but the proton conductivity should be improved since the high grain boundary resistance and poor sintering ability at a high sintering temperature near 1700 °C, so the high sintering temperature was required to obtain densified electrolyte.[69] However, the sintering aid could help decrease the sintering temperature, such as NiO, CuO, $Li_2O$, and ZnO. Doped $BaZrO_3$ could show proton conductivity by creating oxygen vacancies and protonic defects according to eqn (3), where the $Y^{3+}$ mainly was used for $BaZrO_3$ as the

acceptor dopant with the largest conductivity.[69] The densified 20 mol% Yb-doped $BaZrO_3$ electrolyte could be obtained after sintering at 1500 °C by the addition of 1 mol% CuO as the sintering aid with a $5.5 \times 10^{-3}$ S cm$^{-1}$ proton conductivity at 600 °C under the wet $N_2$ atmosphere.[70] Gao *et al.* reported a new method to improve the conductivity of $BaZrO_3$-based conductors by substituting $O^{2-}$ with $F^-$, since the weakened chemical bonding between the cations (Ba or Zr) and the oxygen ions, and F-doping can improve the oxide mobility.[71] Co-doping of Y and other elements (Ni, Co, Fe, and Zn) could impact the grain boundary conductivity and reduce the barrier potential in $BaZr_{0.8}Y_{0.2}O_{3-\delta}$ (BZY), in which 5 mol% Fe doped $BaZr_{0.8}Y_{0.15}O_3$ had a superior conductivity of 0.0212 S cm$^{-1}$ at 600 °C.[72] It was reported that the proton concentration of Y-doped $BaZr_{0.8-x}Ce_xO_{3-\delta}$ solid solutions increases with increasing Ce content between 500 and 700 °C, but the electronic conductivity needed to be evaluated in further research.[73] As shown in Fig. 3b, the electrical conductivity of $BaZr_{0.44}Ce_{0.36}Y_{0.2}O_{3-\delta}$ displayed the highest conductivity below 600 °C compared with oxygen ions conducting electrolyte, which can permit the H-SOECs operating at lower temperatures. Fig. 3c shows the cathode-supported cell with dense electrolyte and porous electrodes in SOEC. The thickness of electrolytes is approximately 17 μm and 500 μm for cathode supports that can provide sufficient electronic and ionic conductivity as well as porosity.

$SrCeO_3$ and $SrZrO_3$-based perovskites are good options for protonic electrolytes, which the $SrZrO_3$-based electrolytes possess a good stable ability, but poor conductivity, and the $SrCeO_3$-based has excellent protonic conduction at high temperatures. Therefore, dopants were added to overcome these weak points. The dopants like Eu, Ho, Mg, Sc, Sm, Tm, Y, Gd, In, Nd, and Tb were investigated by researchers, in which the Tb doping $SrCe_{0.95}Tb_{0.05}O_{3-\delta}$ electrolyte has high conductivity ($10^{-3}$–$10^{-2}$) at 500–900 °C.[74] For the $SrZrO_3$-based electrolyte, the Yb-doping $SrZr_{0.9}Yb_{0.1}O_{3-\delta}$[75] and Y-doping $BaZr_{0.9}Y_{0.1}O_{3-\delta}$[76] could improve the protonic conductivity. Sakai *et al.* studied the influence of the partial substitution of zirconium with cerium in Y-doped $SrZrO_3$ on the steam electrolysis performance and it turned out that the $SrZr_{0.5}Ce_{0.4}Y_{0.1}O_{3-\delta}$ (SZCY541) could improve current efficiency.[76] Later, it was reported that the SZCY541 electrolyte could reach an electrolysis voltage of 1.2 V at 0.1 A cm$^{-1}$.[77] However, the electrolyte resistance should be improved for further application. It is an effective way to reduce the electrolyte thickness and substitute the electrolyte-supported cell with the anode-supported cell to decrease the ohmic polarisation. Moreover, the perovskite-type ceramics-carbonate electrolytes exhibit good ionic conduction, Deqian Huang *et al.* reported that the highest power density and conductivity of $SrCe_{0.6}Zr_{0.3}Lu_{0.1}O_{3-\alpha}$–$Li_2CO_3$–$Na_2CO_3$ were 255 mW cm$^{-2}$ and $8.6 \times 10^{-2}$ S cm$^{-1}$ at 600 °C, and the electrolyte resistances decreased to 0.79 Ω cm$^2$ compared with the $SrCe_{0.6}Zr_{0.3}Lu_{0.1}O_{3-\delta}$ electrolyte (9.62 Ω cm$^2$).[78]

**2.1.4. Stability of proton conducting solid electrolytes.** Ni is used as the anode in H-SOFCs due to the lower anodic overpotential, lower cost and good catalytic properties for the anode reaction compared to those of other metals. Besides, as mentioned above, NiO can act as an external sintering additive for acceptor-doped $Ba(Zr/Ce)O_3$-based electrolytes. For example, the sintering temperature can decrease from 1600 °C to 1400 °C by using 1–2 wt% of NiO in BZY with >95% relative density.[79] However, Ni cations in the anode may diffuse into proton conducting electrolyte, which obviously increases the ohmic resistance of the electrolyte. It was reported that Ni cations occupy the interstitial position of (1/2, 0, 0) of Ba in the BZY, resulting in Ba cations being driven to the grain boundary and a negative effect on conductivity.[80] The grain boundary conductivities of ultrafine-grained pellets were 2–4 times lower than those of microcrystalline samples.[81] The possible reason was the impurity phase $BaY_2NiO_5$ dispersed at the grain surface in ultrafine pellets, resulting in blocking proton transportation. Furthermore, the diffusion of Ni from the anode to the electrolyte during co-sintering can cause the formation of impurities and lead to cell cracking during prolonged operation.[82] A series of proton-conducting electrolytes with a general formula of $BaHf_{0.1}Ce_{0.7}R_{0.2}O_{3-\delta}$ (R = Yb, Er, Y, Gd, Sm) were investigated with chemical stability against steam and $CO_2$ and the compatibility with NiO during sintering. The results showed that $BaHf_{0.1}Ce_{0.7}Yb_{0.2}O_{3-\delta}$ possessed excellent chemical stability and minimal reactivity with NiO, leading to a remarkable peak power density of 1.74 W cm$^{-2}$ in fuel cell mode at 600 °C and excellent durability for over 1000 h in steam electrolysis mode with a high current density of 2 A cm$^{-2}$ at 1.3 V.[83]

The hydration process can produce protonic defects resulting in a considerable structural change including in the phase transitions and the lattice expansion.[41] The chemical expansion under gas humidification increased with the increasing in the basicity of oxides and the concentration of acceptor dopants. The volume change associate with hydration/dehydration might significantly affect their mechanical stress, which can lead to cracking and degradation of the mechanical properties of the electrolyte.[84]

The stability of protonic defects is affected by the temperatures. The proton charge carries decreased with the increasing in temperatures, resulting in a decrease in the proton conductivity at higher temperatures (700–900 °C).[41] This can be solved by providing a higher $pH_2O$ level since the proton concentration can be partially increased at this condition. However, the protonic defects may transfer to hydroxyl groups ($OH^-$) at low temperatures and high concentrations, which leads to the decomposition of proton conductors.[85] For example, the $Ba(OH)_2$ can be form when the temperatures are below 400 °C, since pure $BaCeO_3$ reacts with steam. As mentioned above, co-doping with other ions could improve the stability of the $BaCeO_3$-based materials by decreasing the basicity with an increased tolerance level. Therefore, the main reasons leading to the degradation of H-SOECs and H-SOFCs are the low chemical stability of electrolyte materials at high volumes of $H_2O$ and their expansion incompatibility with other elements in cells. Moreover, the degradation degree of the electrolysis mode was higher than the fuel cell mode, and the possible reason should be the bias potential applied in electrolysis mode increased the degradation.[68]

### 2.2. Progress in oxygen ion-conducting electrolyte and optimisation strategies

The second type of electrolyte facilitates the transport of oxygen ions from the fuel electrode to the electrolyte and ultimately to

the air electrode, where they react to produce oxygen. The presence of oxide defects, such as vacancies and interstitial oxygen ions, significantly influences the conductivity of electrolytes. Therefore, the oxygen ions conductivity could be increased by enhancing the oxygen defects. Yttria-stabilised zirconia (YSZ) is a commonly used electrolyte material with high oxygen ion conductivity and robust mechanical properties, particularly at temperatures ranging from 800 to 1000 °C.

Although the elevated operating temperature can enhance electrode reaction kinetics and oxygen ionic conductivity by reducing electrolyte resistance and polarization resistance between electrolyte and anode and cathode, the practical application of solid oxide electrolysis cells has been limited by several factors associated with high temperature, including poor long-term stability, mechanical stress, and high fabrication costs. Lowering the operating temperature can benefit stability, improve the material's compatibility, and offer wider materials for interconnects to reduce system costs. Moreover, if the operating temperature is below 600 °C, the insulation costs and primary performance degradation could be reduced by decreasing both radiative heat transfer and sintering rates.[86] Therefore, the operating temperature is essential for the SOECs and SOFCs. The diverse electrolytes with different temperatures will be discussed in the following sections.

**2.2.1. Stabilised zirconia electrolyte.** Zirconia-based materials are the most common oxide-ion-conducting electrolytes with the fluorite-type crystal structure ($AO_2$) that cations possess face-centred cubic positions and anions at the tetrahedral sites. As shown in Fig. 5a, there are three different crystal structures for pure $ZrO_2$, monoclinic phase within temperature below 1170 °C, tetragonal (1170–2370 °C), and cubic (>2370 °C).[17] The cubic structure only can be stabilised when the temperature is above 2370 °C, and the crystal volume will be changed following crystal structure transformation. Therefore, the thermal stability is very poor and needs to be improved. Introducing acceptor-based cations with lower valence (trivalent or divalent cation) could stabilise the cubic structure at a large temperature range and introduce oxygen vacancies according to the following eqn (5),

$$M_2O_3 + 2Zr_{Zr}^{\times} + O_O^{\times} = 2M_{Zr}^{'} + V_O^{\bullet\bullet} + 2ZrO_2 \qquad (5)$$

where $M_2O_3$ is trivalent oxide; $O_O^{\times}$, $Zr_{Zr}^{\times}$ and represents that the atoms are in the normal lattice sites; $V_O^{\bullet\bullet}$, $M_{Zr}^{'}$ are the two positive-charged oxygen ion vacancies and negative-charged M ions located in the Zr-site. Dopant cations could be divided into rare earth metals of trivalent ions and alkali metals of divalent ions. As shown in Fig. 5b, oxygen vacancies are introduced by doping, which can enhance ionic conductivity due to the mechanism of hopping oxygen vacancies in zirconia-based electrolytes.

Researchers have explored the doping effect on oxygen ion conductivity mainly in the order of $Nd^{3+} < Sm^{3+} < Gd^{3+} < Dy^{3+} < Y^{3+} < Er^{3+} < Yb^{3+} < Sc^{3+}$ in Fig. 5c.[89,91] Among them,

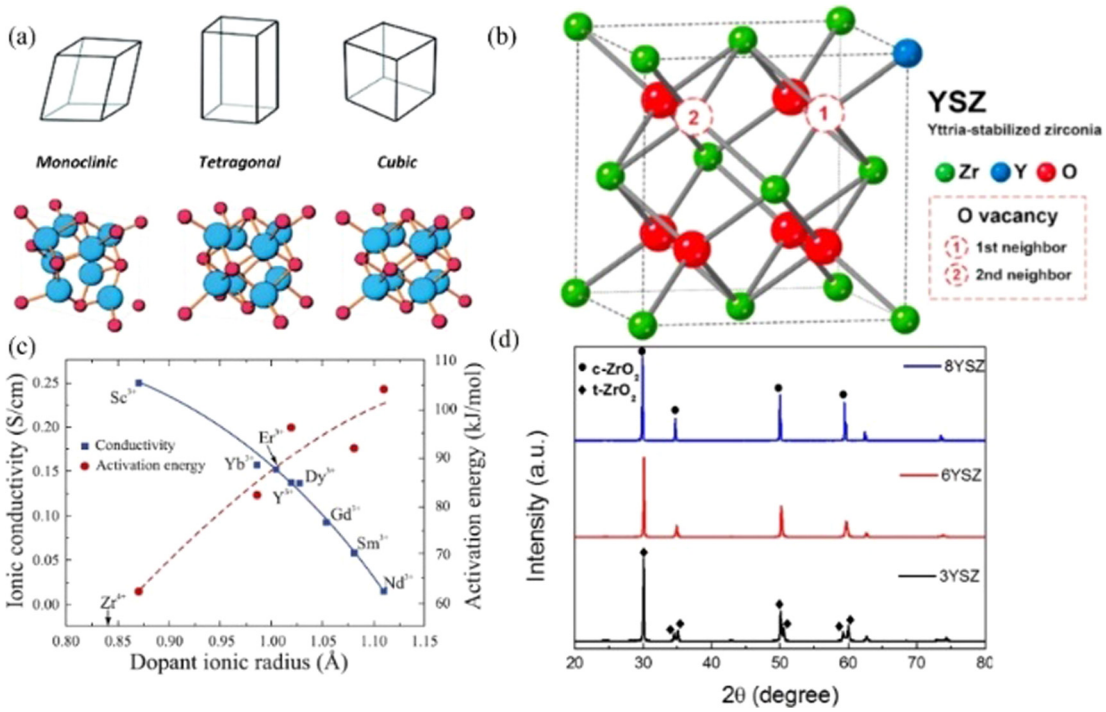


Fig. 5 (a) Crystal structure of $ZrO_2$, blue represents Oxygen ions and red represents Zr ions;[87] (b) cubic structure of YSZ with O vacancy;[88] (c) the maximum ionic conductivities and activation energies with different dopants in $ZrO_2$ electrolytes at 1000 °C;[89] (d) XRD pattern of YSZ.[90] Reproduced from ref. 87 with permission from [Royal Society of Chemistry], copyright [2016]. Reproduced from ref. 88 with permission from [Elsevier], copyright [2020]. Reproduced from ref. 89 with permission from [Elsevier], copyright [2021]. Reproduced from ref. 90 with permission from [Elsevier], copyright [2019].

$Sc_2O_3$-stabilised $ZrO_2$ (ScSZ) had the highest ion conductivity with a value of 0.003 S $cm^{-1}$ at 500 °C, because the ionic radius of $Sc^{3+}$ is the closest to the radius of $Zr^{4+}$, and its ionic conductivity can be achieved at 0.15–0.2 S $cm^{-1}$ at 1000 °C.[92,93] Researchers concluded that 5–9 mol% $Sc_2O_3$ could keep the cubic structure and 10–15% $Sc_2O_3$ would be dominated by the rhombohedral phase, and the optimum concentration was 9 mol% with high ionic conductivity and power density for the operation of SOFCs at intermediate operating temperatures.[94] An Arrhenius equation could express the relationship between temperature and conductivity as follows in eqn (6).

$$\mathrm{Ln}(\sigma T) = -\frac{E_a}{KT} + \mathrm{Ln}\sigma_0 \quad (6)$$

where $\sigma_0$, $K$, and $T$ are the pre-exponential factor (the intrinsic conductivity of the material), the Boltzmann constant ($8.6173 \times 10^{-5}$ eV $K^{-1}$), and the absolute temperature (K), respectively.[95] It could show that the ionic conductivity decreased with the reduction of temperature in the following order: ScSZ > YbSZ > YSZ. The difference between them is more distinct at a lower temperature, suggesting the ScSz could be employed as the electrolyte at intermediate temperatures applications.[96,97] Table 1 shows the various modifications applied to the ScSZ electrolyte in SOFCs. The highest ion conductivity could reach 314 mS $cm^{-1}$ at 800 °C for Ce doped-ScSZ electrolyte.[98] Co-doping $Ce^{4+}$ ions into ScSZ can improve the stability of the cubic phase and suppress the formation of the low-symmetry phase since the larger ions ($Ce^{4+}$, 0.97 Å) can force oxygen vacancies to reside in the nearest neighbour position.[99,100] $Bi_2O_3$ co-doped ScSZ also can enhance the grain growth and the stability of the cubic phase, in which the full density (>99%) electrolyte can be achieved after sintering as low as 1100 °C and that od conductivity was 105 mS $cm^{-1}$ at 800 °C.[101] Despite the good conductivity, ScSZ suffered from serious degradation because of phase transformation, the resistance of 9ScSZ was increased by more than 50% after 60 000 min, which could compensate by increasing the content of $Sc_2O_3$ or co-doping with $Al_2O_3$ or $TiO_2$.[102]

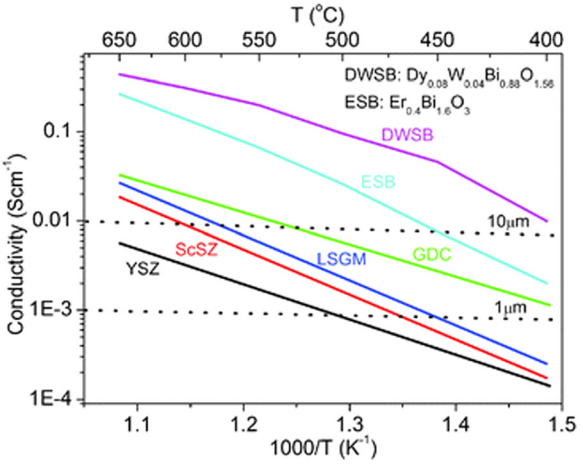


Fig. 6 Conductivities of electrolyte materials at different operating temperatures. The horizontal dashed line indicated the conductivity requirement to achieve ASR < 0.1 Ω $cm^{-1}$ at the thickness of 1 μm and 10 μm.[118] Reproduced from ref. 118 with permission from [Royal Society of Chemistry], copyright [2016].

Moreover, scandium-rich minerals are scarce, and the refinement of scandium is very hard, so its compounds are expensive and could not be widely used as electrolytes. Therefore, despite the high conductivity of ScSZ, the commercial application has been significantly limited due to phase transitions, conductivity ageing, poor accessibility and high price.[17,103]

At present, YSZ is the most widely used electrolyte at high temperatures (800–1000 °C). The cubic phase could be stabilised at 8–10 mol% yttria doping and the maximum oxygen ion conductivity of YSZ can be obtained with 0.13 S $cm^{-1}$ at 1273 K for 8 mol% $Y_2O_3$ dopant (8YSZ) which was prepared by spay drying method of the nitrate precursor solution.[117] As shown in Fig. 5d, 8YSZ is the cubic structure and 3YSZ is the tetrahedral structure with splitting peaks.[90] However, the oxygen vacancies and dopant cations could be increased with higher dopant

Table 1 Cell configuration and performance of ScSZ electrolyte in SOFCs in recent years

| Cell composition anode\|electrolyte\|cathode | Temperature, °C | Conductivity, mS $cm^{-1}$ | Cell configuration | OCV, V | Power density, mW $cm^{-1}$ | Ref. |
|---|---|---|---|---|---|---|
| NiO-ScSZ\|ScSZ thin film\|BSCF58-SDC | 800 | — | Anode support-planer | 1.1 | 1760 | 104 |
| Pt\|SDC/YSZ/SDC\|Pt | 450 | — | Electrolyte-support | 0.8 | 562 | 105 |
| NiO–YSZ\|ScSZ\|MCCO-ScSZ | 800 | — | Anode support | 1.1 | 1920 | 106 |
| NiO-ScSZ\|ScSZ\|LSCF-GDC | 750 | — | Anode support-planer | 1.1 | 509 | 107 |
| NiO-YSZ\|ScYZ | 700 | 120 | Half-cell-pellet | — | — | 108 |
| NiO\|ScSZ/SDC\|SSC-SDC | 750 | — | Anode support-planer | 1.1 | 1052 | 109 |
| NiO-YSZ\|ScSZ1\|LSCF | 750 | 68 | Stainless steel pellets | 1.1 | 1112 | 110 |
| NiO-GDC\|ScSZ thin film | 700 | 25 | Half-cell-pellets | 0.9 | 163 | 111 |
| LSCT\|ScSZ\|LSM-ScSZ | 900 | — | Electrolyte support-pellets | 1.0 | 1380 | 112 |
| NiO-YSZ\|BScSZ\|LSM1-YSZ | 800 | 94 | Electrolyte support-pellets | 1.0 | 387.6 | 113 |
| NiO-ScCeSZ\|ScCeSZ/GDC | 800 | — | Anode-supported half-cell | 1.0 | 1142 | 114 |
| Pt-ScSZ\|MnScSZ\|Pt-10ScSZ | 800 | 120 | Electrolyte support-pellets | — | — | 115 |
| Pt\|10Sc1CeSZ\|Pt | 800 | 314 | Electrolyte pellet | — | — | 98 |
| 1 mol%-$Bi_2O_3$–10 mol%-$Sc_2O_3$-doped $ZrO_2$ | 800 | 105 | Electrolyte pellet | — | — | 101 |
| MCCO-ScSZ\|ScSZ\|MCCO-ScSZ | 750 | — | Symmetric cells | 1.0 | 2210 | 116 |

BSCF58 = $Ba_{0.5}Sr_{0.5}Co_{0.8}Fe_{0.2}O_{3-\delta}$; ScSZ = $Sc_2O_3$-stabilised $ZrO_2$; SDC = $Sm_{0.2}Ce_{0.8}O_{1.9}$; MCCO = $Mn_{1.3}Co_{1.3}Cu_{0.4}O_4$; LSCF = $La_{0.6}Sr_{0.4}Co_{0.2}Fe_{0.8}O_3$; ScYZ = $Sc_{0.08}Y_{0.08}Zr_{0.84}O_2$; SSC = 60% samarium strontium cobaltite; ScSZ1 = $ZrO_2$-10% $Sc_2O_3$; LSCT = $La_{0.43}Sr_{0.37}Cu_{0.12}Ti_{0.88}O_{3-\delta}$; LSM1 = $(La_{0.80}Sr_{0.20})_{0.95}MnO_{3-\delta}$; BScSZ = $Bi_2O_3$ doped ScSZ; ScCeSZ = scandia ceria stabilised-zirconia; MnScSZ = $MnO_2$ doped ScSZ; 10Sc1CeSZ = 1 mol% ceria + 10 mol% scandia stabilized zirconia.

concentration, and this could form complex defects resulting in lower conductivity. Unfortunately, the YSZ has low conductivity at intermediate operating temperatures (400–800 °C). As shown in Fig. 6, an operating temperature $T$ should be higher than 700 °C to achieve a conductivity bigger than 0.01 S cm$^{-1}$, and the resistance of 10 μm thick YSZ becomes excessively large when the temperature is below 700 °C.[118] Several modifications were applied to enhance the performance when lowering the operating temperature, such as reducing the thickness, introducing the metal oxide, and forming a bilayer electrolyte. The target conductivity should be over 0.1 S cm$^{-1}$ for the modified YSZ electrolyte, and the maximum thickness of the electrolyte layer should be less than 20 μm calculated with the following eqn (7):

$$L = SR \times \sigma \quad (7)$$

where $L$ (cm) is the electrolyte layer thickness, $\sigma$ is the ionic conductivity (S cm$^{-1}$), $S$ (cm$^2$) is the electrode area and $R$ (Ω) is ohmic resistance. The thinner electrolyte has high conductivity due to the low ohmic loss and minimising the pathway of ionic oxide.

It is also an effective solution to enhance the performance of YSZ by modifying it with additives such as dopants and coating. Flegler *et al.* coated the surface with several additives like barium, bismuth, calcium, cobalt, copper, iron, lithium, magnesium, manganese, nickel, strontium, or zinc; and it proved that 5% Fe-8YSZ retained the cubic structure and exhibited a high oxygen ion conductivity with full density at ∼150 °C fewer temperatures than pure 8YSZ.[119] Co-doping with other oxides has been researched in recent years, in which the ionic conductivity of 8YZS can be increased from 0.0131 to 0.0289 S cm$^{-1}$ at 1073 K by doping 0.5 wt% ZnO.[120] Table 2 summarised the conductivity of the modified YSZ electrolyte with an operating temperature lower than 800 °C. The conductivities of these electrolytes are not good in the intermediate temperature compared with ScSZ. However, the YSZ electrolyte is more reliable to be used as a portable appliance in the future.[121,122] Limited cathode materials are the weakness for stabilised $ZrO_2$ electrolytes, the commonly used cathode LSCF can cause the chemical interactions from second phases $SrZrO_3$ and $La_2Zr_2O_7$, which makes YSZ electrolytes undesirable for the SOFC performance and durability.[123] Currently, the doped ceria is widely used as the buffer layer to avoid direct contact between the cathode and YSZ electrolyte.[124]

**2.2.2. Doped cerium oxide composite electrolyte systems.** Compared with YSZ, the ceria-based oxides are more widely used as the electrolyte in the intermediate temperatures due to their higher ionic conductivity at 500–800 °C and a lower cost in comparison with LSGM. Similar to zirconia, the structure $CeO_2$ is cubic fluorite with space group $Fm\bar{3}m$ at room temperature to its melting point of 2400 °C, the crystal structure is shown in Fig. 7a. $Ce^{4+}$ cation has a larger ionic radius (0.97 Å, VIII coordination) than $Zr^{4+}$ (0.84 Å, VIII coordination) and the main compensating defects formed in its structure are mainly oxygen vacancies in $CeO_{2-x}$.[36] It was concluded that pure $CeO_2$ is a mixed n-type and ionic conductor, and the ionic conductivity of reduced ceria is less than 3% of total conductivity at 1000 °C and $P_{O_2}$ of $10^{-6}$ atm, and its ionic conductivity is even lower at lower $P_{O_2}$.[139] The ionic conductivity is much lower than the electronic conductivity in $CeO_{2-x}$, while the electronic conductivity can become very low in the air when doping with trivalent or divalent cations introduce more oxygen ion vacancies, which can make doped ceria become excellent electrolytes.[36] The substitution of $Ce^{4+}$ with trivalent or divalent cations can help increase the oxygen ion vacancies to increase the ionic conductivity. The oxygen ion vacancy can be produced *via* eqn (8).

$$O_O^{\times} + 2Ce_{Ce}^{\times} + M_2O_3 = 2M_{Ce}^{'} + V_O^{\bullet\bullet} + 3O_O^{\times} \quad (8)$$

where $M_2O_3$ is trivalent oxide; $O_O^{\times}$, $Ce_{Ce}^{\times}$ and represents that the atoms are in the normal lattice sites; $V_O^{\bullet\bullet}$, $M_{Ce}^{'}$ are the two positive-charged oxygen ion vacancies and negative-charged M ions located in the Ce-site.

Table 2 Cell configuration and performance of YSZ electrolyte in SOFCs in recent years

| Cell composition anode\|electrolyte\|cathode | Cell configuration | Temperature, °C | Conductivity, mS cm$^{-1}$ | OCV, v | Power density, mW cm$^{-2}$ | Ref. |
|---|---|---|---|---|---|---|
| Ag-GDC\|3D printing-8YSZ\|Ag-GDC | Symmetric cell | 850 | — | 1.04 | 176 | 125 |
| NiO-YSZ\|YSZ/GDC\|LSM | — | 800 | — | 1.02 | 300 | 126 |
| NiO-YSZ\|YSZ\|YSZ-LSM | — | 750 | — | — | 1540 | 121 |
| NiO-YSZ\|YSZ/GDC\|LSCF–GDC | Anode support cell | 750 | — | 1.07 | 1480 | 122 |
| YSZ/GDC\| LSCF–GDC | Half cell | 800 | — | 1.1 | 1450 | 127 |
| NiO-8YSZ\|YSZ\|LSM-8YSZ | 3-Ttube SOFC stack | 800 | 40 | 1.1 | 230 | 128 |
| NiO-YSZ\|YSZ\|LSCF | — | 750 | — | 1.1 | 916 | 129 |
| NiO-YSZ\|YSZ/GDC \|LSCF-GDC | Anode support by PLD | 650 | — | 1.1 | 1700 | 130 |
| FeYSZ\|Ni-YSZ\|Pt | Half cell | 800 | 122 | 1.2 | 598 | 131 |
| NiO-YSZ\|YSZ/GDC\|LSCF | — | 650 | — | 1.1 | 1251 | 132 |
| Pt\|Carbonate –YSZ\|Pt | Electrolyte | 600 | 1.6 | — | — | 133 |
| Ni-YSZ\|BiYSZ\|LSM-ESB | Anode support cell | 750 | — | 1 | 600 | 134 |
| NiO-YSZ\|3D printing-3YSZ\|YSZ-LSM | — | 900 | 22 | 1.14 | 100 | 135 |
| Ag\|CuYSZ\|Ag | Electrolyte | 750 | 57.5 | — | — | 136 |
| Ni-YSZ\|8YSZ\|LSM | — | 800 | 21.8 | 1.1 | 114.3 | 137 |
| Pt\|1YSZ thin film\|Pt | Electrolyte | 450 | — | 1.1 | 180 | 138 |

GDC = $Ce_{0.8}Gd_{0.2}O_{1.9}$; LSM = $La_{0.7}Sr_{0.3}MnO_3$; FeYSZ = $Fe_2O_3$ doped YSZ; BiYSZ = $Bi_2O_3$ doped YSZ; ESB = $Er_{0.4}Bi_{1.6}O_3$; Cu8YSZ = CuO doped 8YSZ; 1YSZ = 10.7 mol% doped YSZ; PLD = pulsed laser deposition.

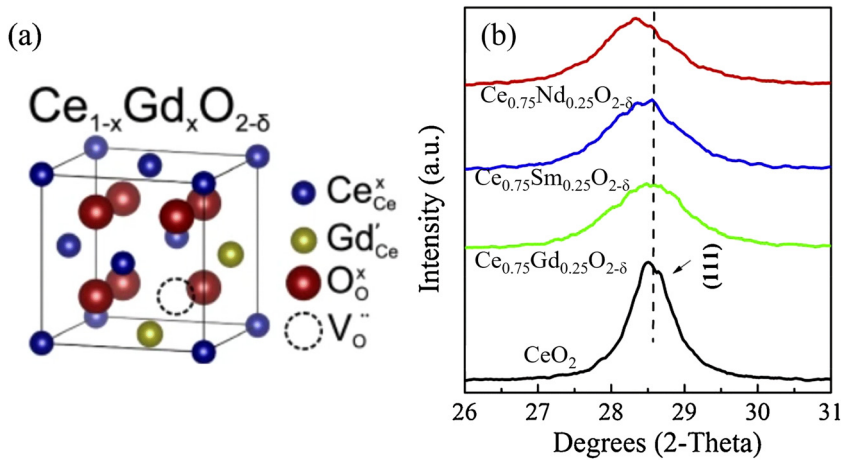


Fig. 7 (a) Crystal structure of $Ce_{1-x}Gd_xO_{2-\delta}$;[140] (b) XRD patterns of $Ce_{0.8}Sm_{0.25}O_{2-\delta}$, $Ce_{0.8}Gd_{0.25}O_{2-\delta}$ and $Ce_{0.8}Nd_{0.25}O_{2-\delta}$. Reproduced from ref. 140 with permission from [Elsevier], copyright [2017]. Reproduced from ref. 141 with permission from [Elsevier], copyright [2017].

Some dopants have been reported to improve the conductivity, such as $Sb^{3+}$, $Bi^{3+}$, $La^{3+}$, $Pr^{3+}$, $Dy^{3+}$, $Y^{3+}$, $Nd^{3+}$, $Gd^{3+}$, $Sm^{3+}$, $Mo^{3+}$, $Pr^{3+}$, $Mn^{3+}$, $Co^{3+}$, $Mg^{3+}$, and $Ca^{3+}$.[141–146] Table 3 concluded some conductivity data of ceria-based electrolytes. The effect of alkaline earth oxides like CaO and SrO could enhance the ionic conductivity and make the activation energy lower, but the addition of BaO and MgO could not help increase the ionic conductivity.[147] Kim has studied the effect of ionic radius and the valence of doping cations on the lattice parameter of ceria, which resulted in the ionic radius of dopants equal to $r_c$ (critical ionic radius) will keep the lattice parameters of fluorite structure, and $r_c$ was calculated to be 0.1106 and 0.1038 nm for the divalent and trivalent cations, respectively.[148] Besides, Kim suggested that $Gd^{3+}$ doped ceria possessed the highest ionic conductivity because its ionic radius (1.053 Å, VIII coordination) is close to $r_c$. For the rare earth oxide dopants, Sm and Gd cations were considered as the best dopants with relatively high ionic conductivity due to the closer ion radius to $Ce^{4+}$, and the optimal dopant concentration should be around 10–25 mol%. As shown in Fig. 7b, the introduction of $Sm^{3+}$, $Gd^{3+}$ and $Nd^{3+}$ into ceria can result in X-ray peaks shifted, due to the change in the lattice parameter.[149] Fine $Ce_{0.8}Sm_{0.2}O_{1.9}$ electrolytes were sintered above 1350 °C, which displayed high relative densities of about 98.5% and excellent total ionic conductivity of 0.082 S $cm^{-1}$ at 800 °C in air.[150] $Ce_{0.8}Gd_{0.2}O_{2-\delta}$ electrolytes have been synthesised by the citric acid-nitrate combustion method and can achieve a high conductivity of 0.0564 S $cm^{-1}$ at 700 °C.[151] As shown in Fig. 7, 10 μm thick GDC could provide good conductivity when temperatures are down to 500 °C.

Co-doping methods could further improve the ionic conductivity of the ceria-based electrolyte. $La^{3+}$ and $Pr^{3+}$ co-doped cerium oxide compositions were examined as prospective electrolytes at intermediate temperatures, and $Ce_{0.8}La_{0.1}Pr_{0.1}O_{2-\delta}$ electrolyte synthesised by a sol–gel method had the highest conductivity of 0.184 S $cm^{-1}$ at 600 °C with the lowest grain boundary values, reduced band gap value and the lowest PL intensity.[143] Hala *et al.* studied that the co-doped $Ce_{0.8}Y_{0.1}Mn_{0.1}O_{2-\delta}$ exhibited the highest conductivity of 0.06 S $cm^{-1}$ and 0.15 S $cm^{-1}$ in $H_2$ and air at 700 °C, respectively, which the possible reason should be Y impeded the reduction of $CeO_2$ under reducing conditions and Mn-doped $CeO_2$ showed better reducibility.[141] Moreover, the composition $Ce_{0.8}Sm_{0.05}Ca_{0.15}O_{2-\delta}$ exhibited a high conductivity with a value of $1.22 \times 10^{-1}$ S $cm^{-1}$ at 700 °C with minimum activation energy (0.56 eV).[152]

The total ionic resistance of polycrystalline electrolytes largely depends on grain and grain boundary, and it has been reported that the grain boundary conductivity is lower than grain conductivity by 2–3 orders of magnitude.[153] The grain boundary conductivity can be influenced by various factors, including the presence of impurities, secondary phase segregation, lattice mismatch, space charge effects, and the occurrence of microcracks.[154] The dopant cations have a tendency to diffuse from the grain boundary and segregate near the grain boundaries at high sintering temperatures. Moreover, the resistance could be increased with the presence of impurity and depletion of oxygen ions vacancies at the grain boundary area, which have bad effects on the ionic conductivity.[155] Therefore, the reduction of sintering temperature could increase the grain boundary interfacial area and make the

Table 3 The ionic conductivity of doped $CeO_2$ electrolytes

| Electrolyte | Conductivity, mS $cm^{-1}$ | Temperature, °C | Activation energy, eV | Ref. |
|---|---|---|---|---|
| $Ce_{0.8}Sm_{0.1}Bi_{0.1}O_{2-\delta}$ | 3.18 | 750 | — | 142 |
| $Ce_{0.8}Sm_{0.2}O_{2-\delta}$ | 2.66 | 750 | — | 142 |
| $Ce_{0.8}Sm_{0.1}Sb_{0.1}O_{2-\delta}$ | 0.038 | 750 | — | 142 |
| $Ce_{0.8}La_{0.1}Pr_{0.1}O_{2-\delta}$ | 184 | 600 | 0.64 | 143 |
| $Dy_{0.1}Ce_{0.9}O_{2-\delta}$ | 10 | 650 | 0.71 | 144 |
| $CeO_2$:Pr 2.0% | 14.95 | 750 | 0.222 | 145 |
| $Ce_{0.9}Y_{0.1}O_{2-\delta}$ | 15.1 | 700 | 0.78 | 141 |
| $Ce_{0.8}Y_{0.1}Mn_{0.1}O_{2-\delta}$ | 61.9 | 700 | 1.07 | 141 |
| $Ce_{0.8}Gd_{0.2}O_{2-\delta}$ | 56.4 | 700 | — | 151 |
| $Ce_{0.8}Gd_{0.12}Nd_{0.08}O_{2-\delta}$ | 62.6 | 700 | — | 151 |
| $Ce_{0.8}Sm_{0.05}Ca_{0.15}O_{2-\delta}$ | 122 | 700 | 0.56 | 152 |
| $Ce_{0.8}Co_{0.07}Sm_{0.13}O_{2-\delta}$ | 53.8 | 600 | 0.567 | 141 |
| $(CeO_2)_{0.96}Sm_{0.04}$ | 170 | 500 | — | 146 |

segregated impurities spread over a large area, which in turn reduces the thickness of the grain boundary and enhances the ionic conductivity. The sintering temperature can be decreased by using nano-sized powders due to their high surface area, or by adding sintering additives, such as NiO, CoO, $Cr_2O_3$, CuO, $Bi_2O_3$, MnO and $Fe_2O_3$ to improve the sinterability of ceria.[156–158] Such additives can decrease the total melting point and promote the formation of a liquid phase to improve the grain boundary adhesion by filling pores. Therefore, the continuous dissolution and formation of particles can promote mass transfer and result in rapid densification at lower temperatures.[159] However, such sintering additives may decrease the conductivity of electrolytes by increasing the grain boundary resistance, especially in the presence of $SiO_2$.[160] For example, cobalt ions were found to segregate at the grain boundaries, even though it was an effective sintering aid to promote sinterability.[161]

The major issue which limits the application of ceria-based electrolytes is the reduction of $Ce^{4+}$ to $Ce^{3+}$ ions in low oxygen partial pressures and high temperatures, which normally happens at the anode in SOFC.[162] The reaction can be presented as follows:

$$2Ce_{Ce}^{\times} + O_O^{\times} \leftrightarrow \frac{1}{2}O_2(g) + V_O^{\bullet\bullet} + 2Ce_{ce}^{'}$$

Therefore, the oxygen vacancies are formed with the generation of two additional electrons as a charge compensation defect, which results in the expansion or contraction of the host ceria lattice followed by mechanical failure.[163] Moreover, these electrons are in the periphery of $Ce^{3+}$, thereby forming the small polarons, which contribute to the electronic conductivity in the electrolyte and lower OCV, especially for thin electrolytes.[164] Decreasing the operating temperatures is one of the effective ways to decrease the reduction of $Ce^{4+}$. And bilayer electrolyte can be chosen by combining doped ceria with YSZ or doped $LaGaO_3$ to improve the stability of ceria-based electrolytes. Although the reduction of ceria-based electrolytes is a critical issue, they are suitable for metal-supported SOFCs with high power density at lower temperatures. More work needs to be done on the reduction and fabrication of thin electrolytes to decrease the ohmic resistance.

**2.2.3. $Bi_2O_3$-based electrolyte systems.** In the category of fluorite structure-based oxides, δ-$BiO_3$ is particularly interesting due to their high ionic conductivity at low temperatures, which is 10–100 times higher than YSZ.[118] The high oxygen ion conductivity arises from a highly intrinsic concentration of oxygen vacancies (25%) and high anion mobility, in which the oxygen vacancies are favoured by the weak Bi–O bond in the fluorite structure and the high anion mobility is related to the high polarisation of the $Bi^{3+}$ with its 'long pair' of electrons.[165] $Bi_2O_3$ has two stable polymorphs: monoclinic α (stable at temperatures lower than 723 °C) and cubic δ (stable at 730–825 °C).[166] The δ-$Bi_2O_3$ is prone to convert into α phase or metastable tetragonal-phase (β) when the temperatures are below 730 °C to room temperatures, and then the conductivity drops more than three orders of magnitude.[28] Moreover, 825 °C is the melting temperature. The crystal structure and XRD pattern of different phases are shown in Fig. 8. The stabilisation can be achieved by the substitution of bismuth with rare-earth dopants (like La, Pr, Y, Dy, or Er) and the combination with high valent cations like W, V, or Nb.[167] The $(Bi_2O_3)_{0.75}$-$(Y_2O_3)_{0.25}$ electrolytes fabricated by plasma spraying with 37.5–75 μm powers lamellar interfaces, which could obtain the excellent ionic conductivity of 0.19 S $cm^{-1}$ and stable δ-phase.[168] The 16 mol% $Yb_2O_3$ stabilised δ-$Bi_2O_3$ could obtain the maximum electrical conductivity with a value of 0.632 S $cm^{-1}$ at 750 °C, which could be used as solid electrolytic industrial applications.[169]

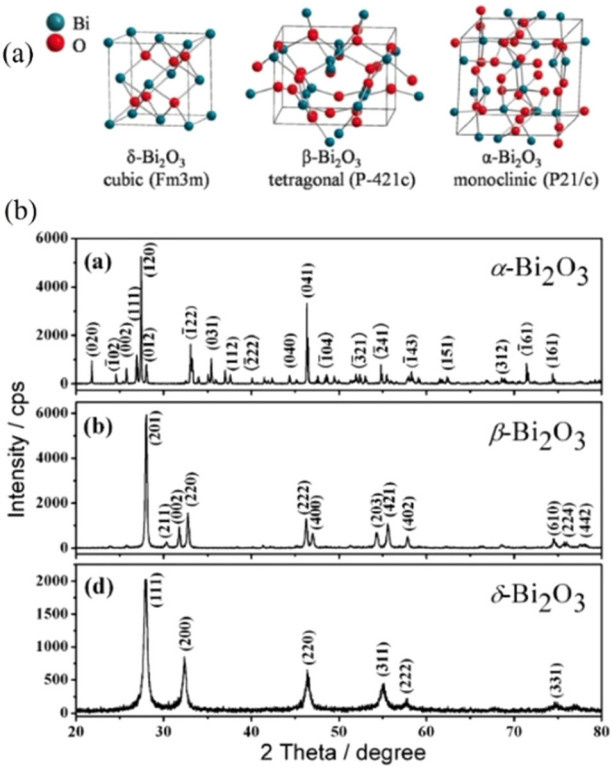


Fig. 8 (a) The crystal structure[170] and XRD pattern[7] of α-$Bi_2O_3$, β-$Bi_2O_3$ and γ-$Bi_2O_3$. Reproduced from ref. 170 with permission from [Elsevier], copyright [2023]. Reproduced from ref. 7 with permission from [Royal Society of Chemistry], copyright [2010].

$Er_2O_3$-stabilised $Bi_2O_3$ ($Er_{0.2}Bi_{0.8}O_{1.5}$, ESB) possesses the highest oxygen ion conductivity (0.32 S $cm^{-1}$ at 700 °C), but its stability needs to be enhanced due to phase transformation from the cubic phase to rhombohedral phase after long operation at 600 °C.[171] This degradation can be partly suppressed by doping higher valence cations, such as 5 mol% $CeO_2$ into ESB, but it has not yet been completely possible to avoid such phase transformation.[172,173] It was reported that only 1 mol% of Hf doping can enhance the stability of ESB to run around 1200 h at 600 °C by suppression of its phase transition kinetics, maintaining superior conductivity of 0.14 S $cm^{-1}$.[174] The co-doping of two metal oxides can facilitate the stabilisation of the cubic phase down to room temperature with lower doping concentration. The δ-$Bi_2O_3$ phase can also be stabilised in a limited compositional region in the ternary system $Bi_2O_3$–$Er_2O_3$–$WO_3$ and the maximum oxide-ion can be achieved at 0.05 S $cm^{-1}$ with the activation energy 0.9 eV for the sample $(Bi_2O_3)_{0.735}(Er_2O_3)_{0.21}(WO_3)_{0.05}$ at 550 °C.[175] It was reported that the $Dy_2O_3$–

$ZrO_2$–$Bi_2O_3$ system has shown excellent stability for 450 h at 500 °C with the highest conductivity of 0.037 S $cm^{-1}$.[176] Triple-doped bismuth oxides also can enhance the stability, such as Er, Y and Zr triple-doped $Bi_2O_3$ (EYSB) exhibited high ionic conductivity of 0.44 S $cm^{-1}$ at 600 °C with excellent stability over 1000 h.[177] The other challenges for the stabilised $Bi_2O_3$ electrolytes are their tendency to reduce to metallic bismuth under $H_2$ conditions, easy volatilisation at high temperatures instability under a reducing atmosphere and low mechanical strength.

Another type of $Bi_2O_3$-based electrolyte is γ-$Bi_4V_2O_{11}$ (BIVOX), which can be stabilized by partial substitution vanadium with transition metals such as Cu, Ni, and Co and proved to possess high ionic conductivity at temperatures below 600 °C.[178] The doped γ-$Bi_4V_2O_{11}$ (BIMEVOX) shows higher stability at moderate temperatures compared with $Bi_2O_3$-based oxides, though still questionable.[179] Some electrolytes with the highest oxygen ion conductivity have been reported for $Bi_2V_{1-x}Me_xO_{5.5-\delta}$, where Me = Cu, Ni and $0.07 \leq x \leq 0.12$.[180] $Bi_4Ni_{0.2}V_{1.8}O_{10.7}$ prepared by the sol–gel method can obtain the highest conductivity with the value of $6.9 \times 10^{-3}$ S $cm^{-1}$ and the activation energy of 0.41 eV at 300 °C in the air.[181] Researchers also studied that different preparation techniques lead to various conductivity due to different microstructures. Nanomaterials with smaller crystalline or grain sizes exhibited a higher conductivity due to lower activation energy and smaller size which can help to stabilise the disordered γ-phase and acquire high density in sintering.

However, the high chemical reactivity and low mechanical strength, make these materials hard to practically use in SOFCs, even though the high conductivity level at intermediate temperatures. The multilayer cells can be used to solve these issues, such as applying other layers acting as mechanical support on the layer of $Bi_2O_3$-based electrolyte, which can improve the mechanical strength and protect it against reduction.[182] The doped ceria layer should be thick enough to isolate the $Bi_2O_3$ from fuel conditions and maintain an effective oxygen partial pressure bigger than $10^{-13}$ atm to avoid decomposition.[118] Compared to a single layer, the OCV was increased by 90–160 mV reaching 1.003 V at 500 °C for the bi-layer electrolyte using doped ceria and doped $Bi_2O_3$ layers, and it can be stable for 1400 h under both OCV and maximum power conditions.[86] Another advantage of using a $Bi_2O_3$-based layer on the air side is the decrease in cathode overpotential, due to more active adsorption sites of oxygen species compared to a ceria-based electrolyte.[183] The fabrication of bilayer $Bi_2O_3$/$CeO_2$ is different from other bilayer systems firing together, due to the low firing temperature of $Bi_2O_3$-based electrolyte (lower than 800 °C). Normally, the $CeO_2$-based electrolyte layer co-sintered with an anode layer at higher temperatures (~1400 °C), and then deposited the $Bi_2O_3$-based layer firing at low temperatures. Moreover, the thickness and thickness ratio of these two layers are stricter compared with other bi-layer system, due to the leaky of ceria-based layer in the reducing atmosphere. There should be an optimised thickness to obtain the low ohmic resistance and high OCV. In total, $Bi_2O_3$-based electrolyte provides the feasibility to operate at low temperatures if appropriate electrodes can be used.

**2.2.4. Perovskite-type electrolyte systems.** $ABO_3$-type perovskites were investigated as ionic conductors with high conductivity, where A is a lanthanum or alkaline earth element, and B is a transition metal element. Many perovskite oxides have mixed electronic and oxygen ion conductivity, which can be used as anodes in SOECs. However, some perovskites also show high and pure oxygen ion conductivity, such as doped $LaGaO_3$, perovskites based on $LnBO_3$ (B = Al, In, Sc, Y), Brownmillerite-like phase, $La_2Mo_2O_9$ (LAMOX) based electrolyte materials and apatite structure perovskites, which are suitable to be good electrolytes at intermediate temperatures.

*2.2.4.1 $LaBO_3$ (B = Ga, Al)-based electrolytes.* The oxygen ion migrates into an adjacent vacant site along the (1 1 0) edges of $GaO_6$ octahedra for the perovskite-type $LaGaO_3$, which is the lowest path as shown in Fig. 9.[184] Doping $LaGaO_3$ exhibited good ion conductivity with divalent alkaline earth metal ions like $Ca^{2+}$, $Ba^{2+}$, and $Sr^{2+}$, in which oxygen vacancies will be generated to increase the ionic conductivity. $Sr^{2+}$ ion has the closest ionic radius with $La^{3+}$, thereby the substitution of $La^{3+}$ with $Sr^{2+}$ (LSM) has the highest oxygen ion conductivity among these alkaline earth metal ions. However, the doping amount is limited by less than 10% since the impurity phases $SrGaO_3$ and $La_4SrO_7$ can be found with higher doping amounts.[185] Co-doping $Mg^{2+}$ and $Sr^{2+}$ into the $Ga^{3+}$ site and $La^{3+}$ site could further increase the ionic conductivity and doping limitation of $Sr^{2+}$ to 20 mol%.[186] Pelosato *et al.* reported that the sintered $La_{0.8}Sr_{0.2}Ga_{0.8}Mg_{0.2}O_{3-\delta}$ (LSGM) electrolyte exhibited a relative density of 98% and a total conductivity of $1.13 \times 10^{-2}$ S $cm^{-1}$ at 600 °C.[187] LSGM exhibited only oxide ionic conductivity from ($P_{O_2} = 10 \times 10^{-20}$–1 atm), and its ionic conductivity was higher than Sc-doped $ZrO_2$, but slightly lower than $Bi_2O_3$ based electrolyte.[30] As shown in Fig. 5, LSGM exhibited good ionic conductivity when the operating temperature was down to 550 °C over a wide oxygen partial pressure range. When sintering LSGM, the impurity $LaSrGaO_4$ was identified. However, no additional grain-boundary resistance was observed, since the liquid state of $LaSrGaO_4$ enhances the grain-boundary contact, thereby suppressing its resistance.[188]

Furthermore, the ionic conductivity can be improved a lot *via* the substitution of certain transition metals (Fe, Co, Ni) into

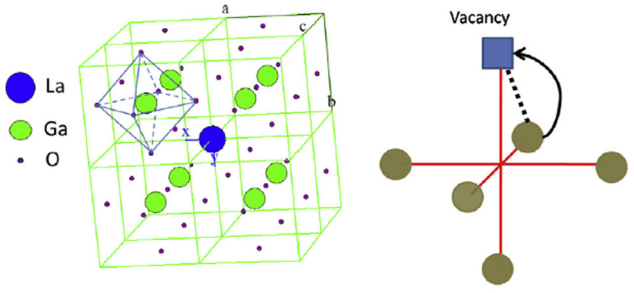


Fig. 9 The cubic $ABO_3$ perovskite structure, and the path of oxygen ions migration along $BO_6$ octahedron edge.[184] Reproduced from ref. 184 with permission from [Elsevier], copyright [1995].

the Ga site in LSCF at lower temperatures, while the increase in electronic conductivity makes these electrolytes problematic for further application in SOFCs.[189] To minimise electronic conduction, it is necessary to restrict the $Co^{3+}$ dopant concentration to below 3–7%. Interdiffusion of Ni during high temperatures co-firing with Ni-based anodes may cause undesirable electronic conductivity and impurity phase $LaNiO_3$ which does not conduct oxygen ions.[118] Besides, La may lose from LSGM to react with electrodes and form non-perovskite phases if La content is not sufficient at electrodes.[190] Therefore, the LSGM electrolytes have been used less than doped ceria, due to several challenges: (1) difficulty to obtain the high relative density; (2) gallium oxide is prone to reduction, volatilization and reaction with Ni-based cermet. (3) Impurity phases are likely to form during co-firing.[11,191] The thin barrier layer should be coated into LSGM electrolyte to enhance $LaGaO_3$-based electrolyte to apply in SOFCs, such as $La_{0.4}Ce_{0.6}O_{1.8}$.[188]

Pure $LaAlO_3$ materials may not be a good candidate for solid electrolytes due to the lower ionic conductivity and mixed conduction behaviour in an oxidising atmosphere. Suitable dopants could enhance the ionic conductivity, and doped $LaAlO_3$ exhibits p-type electronic conductivity at high oxygen partial pressure and nearly ionic conductivity with pure oxygen.[192] $Mg^{2+}$, $Ca^{2+}$, and $Sr^{2+}$ dopants show higher ionic conductivity compared with non-doped $LaAlO_3$; in which the highest conductivity was about $1.3 \times 10^{-2}$ S cm$^{-1}$ at 900 °C, but its conductivity was lower than LSGM or $Sm^{2+}$ doped $CeO_2$.[193] But $LnAlO_3$-based electrolytes exhibit better stability at reduction atmosphere and less volatilisation, so they are promising candidates as protective layers for $LaGaO_3$-based materials at the cathode side for SOECs. It was reported that $(La_{0.8}Sr_{0.2})_{0.94}Al_{0.5}Mn_{0.5}O_{3-\delta}$ could be potential anode materials for SOFCs which can match YSZ very well as well as no chemical reaction between them, and its electrochemical performance was good with the low polarisation resistances of value 0.34 Ω cm$^2$ in wet (~3% $H_2O$) Ar/20% $H_2$ atmosphere.[194]

*2.2.4.2 $La_2Mo_2O_9$ (LAMOX) based electrolyte materials.* $La_2Mo_2O_9$ (LAMOX) based electrolytes exhibit higher oxygen ion conductivity than YSZ and are comparable to those of well-known oxygen ion conductors (LSGM and GDC) at intermediate temperatures. The compounds undergo a structural phase transition from α phase (monoclinic, $P2_1$) to β phase (cubic, $P2_13$) at about 580 °C, where β phase exhibits higher ion conductivity. It was reported that the crystal structure of β-LAMOX resembles β-$SnWO_4$, in which $Sn^{4+}$ is replaced by $La^{3+}$ and generates an oxygen vacancy shared by two partially occupied oxygen sites that surround the $Mo^{6+}$ cation.[195,196] To avoid the sudden volume change related to phase transition and stabilise the β phase at room temperatures, many cations have been studied to substitute in LAMOX, where La site with alkali metals, $K^+$, $Rb^+$, alkaline earth metals like $Ca^{2+}$, $Sr^{2+}$, $Ba^{2+}$, transition as well as rare earth ions $Bi^{3+}$, $Y^{3+}$, $Sm^{3+}$, $Gd^{3+}$, $Dy^{3+}$, $Er^{3+}$, $Eu^{3+}$; and Mo site with $W^{6+}$, $V^{5+}$, $Ta^{5+}$, $Cr^{6+}$.[197] Although many substituting cations may stabilise the β-phase, the conductivity could not be improved by doping every dopant. However, co-doping is a better method to improve stability as well as conductivity at high temperatures. For example, co-doping with Dy/W-$(La_{1.8}Dy_{0.2})(Mo_{2-x}W_x)O_9$ ($0 \le x \le 1.6$) electrolytes were reported with higher ionic conductivity (0.18 S cm$^{-1}$) at 800 °C, compared with $La_2Mo_2O_9$ (0.08 S cm$^{-1}$), and the Dy/W dopants can help suppress the α–β phase transformation, but Dy addition did not assist in the structural stability in $H_2$ environment at high temperature.[198] However, the electrolyte LAMOX is limited for further application for three reasons: unstable crystal structure under reducing conditions; thermal expansion is larger than common electrode materials; and it reacts with cathode materials.[199] Side production of $SrMoO_4$ can increase the polarisation resistance, so the cathode containing Sr cannot contact the LAMOX electrolyte, which should solve this problem by coating the bi-layer or substituting it with other cathode materials.[200] These issues should be further improved or solved to make LAMOX electrolytes used widely.

*2.2.4.3 Apatite structure.* Apatite structure has a general formula $La_{10-x}(Si/Ge)_6O_{26\pm\delta}$ ($x$ = 0–0.67), and the conductivity increases with $x$ decreases as the interstitial oxide-ions are introduced.[201] Whilst germanate apatite is not suitable for practical application, because of high volatilisation, and high cost. Normally, the electrolytes of the apatite phase exhibited higher ionic conductivity compared to the YSZ at the intermediate temperatures (500–800 °C) with moderate thermal expansion coefficients (TEC) and low electronic conductivity. In the apatite lattice, La site cations are occupied in the cavities created by $SiO_4$ tetrahedra, and additional oxygen sites (O5) form the channels of the movement of interstitial oxygen ions.[167] Plenty of works show that ionic conduction is mainly due to the parallel and perpendicular interstitial oxygen and the interstitial oxides migrate along the $c$-axis.[202] Oxygen excess compositions were reported with higher conductivity, such as $La_{9.67}(SiO_4)_6O_{2.5}$ exhibited higher conductivity ($1.3 \times 10^{-3}$ S cm$^{-1}$) compared with $La_{9.33}(SiO_4)_6O_2$ ($1.1 \times 10^{-4}$ S cm$^{-1}$) at 500 °C temperature, which indicated that interstitial oxygen ions play a great role in enhancing the oxygen ion conductivity and suggest the interstitial migration mechanism.[203] The highest ionic transport is observed when there are more than 26 oxygen ions in per unit formula, and $La_{10}Si_6O_{27}$ exhibited good ionic conductivity with a value of $4.3 \times 10^{-3}$ S cm$^{-1}$ at 773 K.[204] La site deficiency is another important factor to influences ionic conductivity, which the deficiency affects the unit cell volume and may result in O5 ions displacing into interstitial sites and producing vacancies into O5 sites at fixed total oxygen content.[202,205] For example, in the system, $La_{9.33+x/3}Si_{6-x}Al_xO_{26}$, Al doping can increase the ionic conductivity without oxygen content variations by compensating A-site vacancy concentration.[205]

To improve the conductivity of apatite-type materials, a lot of work focused on the synthesis and characterisation of $La_{9.33+x}(SiO_4)_6O_{2+3x/2}$ with dopants on La or Si sites. Various dopants used for La- and Si-sites are listed below.[17,206,207] The bigger ions are preferred to substitute into La-site, whereas ions of small ionic radius are preferred to substitute in Si-site.

La-site: Mg, Ca, Sr, Ba, Co, Ni, Cu, Mn, Bi, Na, K, Nd, Sm, Yb

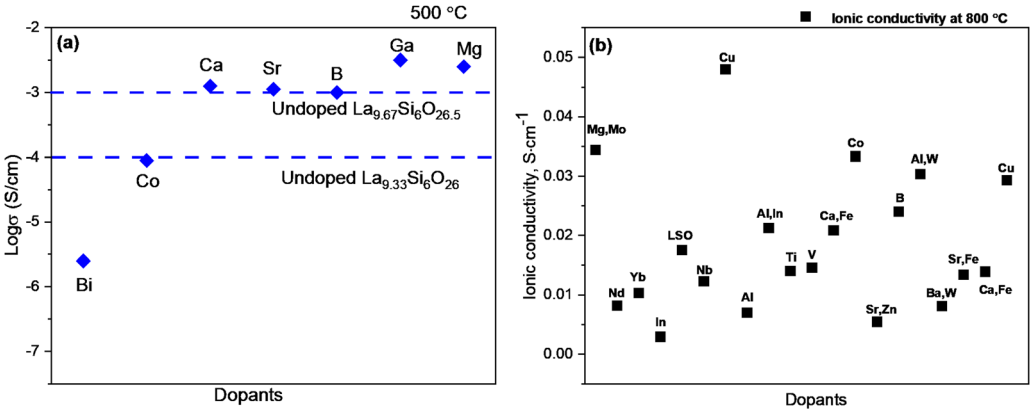


Fig. 10 (a) Comparison of conductivities of different dopants at a constant level of oxygen excess at 500 °C; (b) ionic conductivity of different dopants at 800 °C.

Si-site: B, Al, Ga, Mg, Ti, Ge, Fe, Co, Ni, Cu, Mn, P, In, Zn, Co, Ba, Nb, V, Mo, W

The conductivity data has been shown in Fig. 10a with different dopants at 500 °C and 800 °C, where the ions of Ga, B and Mg are substituted into the Si site, the ionic conductivity can be enhanced.[208] However, a decrease in conductivity can be observed with smaller cations on La-site, such as $Mg^{2+}$, which was due to the change of coordination environment from 9 ($La^{3+}$) to 6 ($Mg^{2+}$) and led to the great movement of Si site towards the oxygen ion channels.[17] Moreover, the substitution of $Ti^{4+}$ at Si-sites exhibited a decrease in conductivity, which was attributed to the extended coordination of $Ti^{4+}$ trapping mobile interstitial oxygen ions.[209]

As shown in Fig. 10b, the co-doped method can greatly enhance the conductivity and restrain the formation of the impurity phases ($La_2SiO_5$ and $La_2Si_2O_7$). The addition of $Bi^{3+}$ and $Sn^{4+}$ as dopants has increased the conductivity with a high value of $1.84 \times 10^{-2}$ S cm$^{-1}$ at 873 K.[210] Co-doped on the $Si^{4+}$ site with $Al^{3+}$ and different other cations ($W^{6+}$, $In^{3+}$, $Nb^{5+}$, or $Mg^{2+}$) were investigated and the $La_{10}Si_5Al_{0.9}W_{0.1}O_{26.65}$ exhibits the highest conductivity of $3.03 \times 10^{-2}$ S cm$^{-1}$ at 1073 K.[211] The highly purified polycrystalline powders of Mg–Mo co-doped LSO (Mg/Mo-LSO) electrolytes were synthesised with excellent densification properties and high ionic conductivity (33.94 mS cm$^{-1}$) at 800 °C.[208] Silicate apatite could not be used widely due to several limitations. The main drawbacks are that it is hard to prepare dense ceramic electrolytes, for which a high sintering temperature is required to form densified pellets, but the impurity of $La_2SiO_5$ and $La_2Si_2O_7$ could be created during the high sintering process. Another issue is the degradation of the ionic transport properties due to silica migration and volatilisation in the reducing atmospheres.[212] Several efforts are attempted through different synthesis routes, such as solid-state reaction, sol–gel, hot-pressing, hydrothermal synthesis, co-precipitation, and floating zone methods to decrease the particle size and increase the relative density at lower sintering temperatures. Co-dopants could prohibit the formation of impurities at high sintering temperatures and improve stability. A complete single cell with an LSO-based electrolyte has not yet been reported frequently, especially with different electrode materials. Therefore, further studies are needed to investigate whether these types of materials can serve as good and stable electrolytes with different electrode materials.

### 2.3. Dual-ion (proton and oxygen ion) conducting electrolyte

Dual-ion conductors exhibit conductivity with two different charges, oxygen ions and protons, which have proposed as a new class of electrolyte for low and intermediate temperatures SOFC.[213] For a dual-ion conducting electrolyte, no external gas humidification is required, since water will be produced at both anode and cathode. Besides, the simultaneous transportation of oxygen ions and proton in the electrolyte can enhance the total conductivity and improve cell performance.

**2.3.1. Single phase dual-ion conducting electrolyte.** The perovskite oxides are the main single-phase electrolyte with mixed proton and oxygen–ion conductivity. The efficient paths for the single perovskite with mixing conductivity is shown in Fig. 11a, where the oxygen ions diffuse in oxygen ion vacancies and protons transfer in Grotthuss mechanism. Doping strategy was used to generate oxygen ion vacancy and proton defects for the well-known protonic electrolytes. Doped $BaCeO_3$ may show mixed proton and oxygen conductivity under fuel cell operation condition. It was reported that doped $BaCeO_3$ exhibits proton conductivity in a $H_2$ atmosphere, while it transitions to a mixed conductor when $H_2$ is supplied to the anode and $O_2$ to the cathode.[33] It was also reported that a distinct turning point in the Arrhenius plot of $BaCe_{0.8}Sm_{0.2}O_{2.9}$ can be observed at 550 °C under fuel cell conditions, attributed to its dual-ion conducting properties.[214] The perovskite-type $BaZr_{0.1}Ce_{0.7}Y_{0.1}Yb_{0.1}O_{3-\delta}$ was confirmed with a mixed dual ion conductivity by *in situ* monitoring the water information in both anode and cathode.[215] The result showed that the absolute humidity was about 20.0 g m$^{-3}$ in the anode chamber and 65.5 g m$^{-3}$ in the cathode chamber. The conductivities of proton and oxygen ions are highly sensitive to operation conditions such as temperatures and surrounding atmosphere. This makes it particularly challenging to optimise the transfer numbers of both oxygen ions and protons to enhance fuel cell performance. In mixed oxygen ion and proton

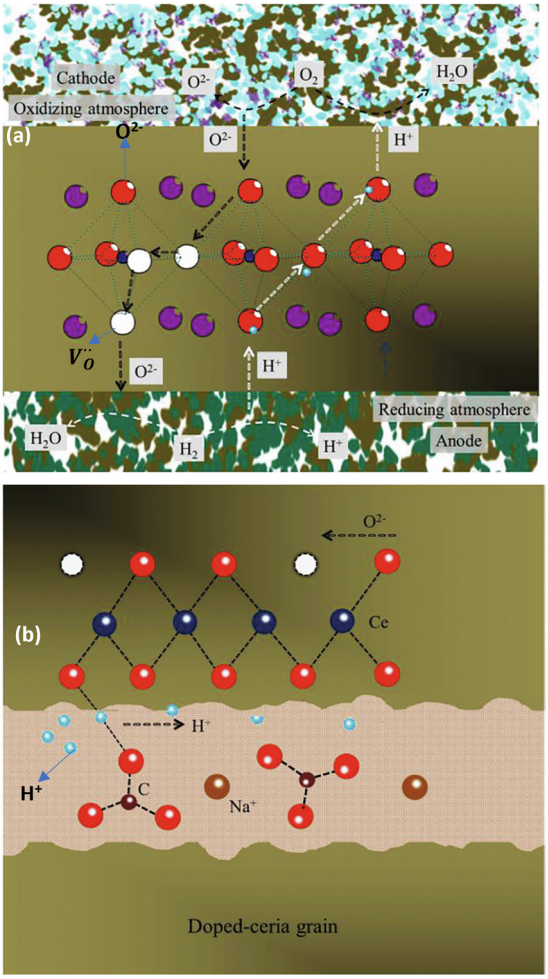


Fig. 11 (a) Schematic model of mixed conduction for single perovskite-based electrolyte. (b) Schematic model of SDC/$Na_2CO_3$ nanocomposite.[213,216] Reproduced from ref. 213 with permission from [Elsevier], copyright [2021].

conducting perovskites, oxygen ion conductivity decreases significantly as the temperature drops, with proton conduction dominating at lower temperatures. As a result, single-phase perovskite oxide is generally unsuitable for function as dual-ion electrolytes at temperatures below 500 °C.[216]

**2.3.2. Doped $CeO_2$ and perovskite oxide composites.** A composite electrolyte by mixing a proton conductor with oxygen ion conductor can develop a dual ion conducting electrolyte at a proper ratio. The commonly used composites are the combination of doped ceria with a proton conducting perovskite oxide. Different composites were investigated, but the majority of composite-based fuel cells have shown relatively lower performance compared to those utilising pure perovskite or fluorite-type electrolyte. The co-ionic ($H^+/O^{2-}$) composite of $BaZr_{0.85}Y_{0.15}O_{3-\delta}$ (BZY) and $Nd_{0.1}Ce_{0.9}O_{2-\delta}$ (NDC) was used as the electrolyte in an anode-supported fuel cell, achieving a maximum power density of 330 mW $cm^{-2}$ and an OCV of 1.01 V at 650 °C.[217] The advantages of this composite electrolyte are its ability to decrease the electronic loss of NDC under $H_2$ atmosphere and enhance the sinterability of BZY. However, the metal ion (Ba ion) migration was found out in the composite of $BaCe_{0.5}Zr_{0.4}Y_{0.1}O_{3-\delta}$ (BZCY) and $Y_{0.2}Ce_{0.8}O_{3-\delta}$ at temperatures above 500 °C, resulting in the decrease in ionic conductivity and the increase in the grain boundary resistances compared to the single-phase samples.[218] Besides, there is a significant risk of chemical interaction between the two phases either during high-temperature calcination for densification or during operation.[219] The formation of new phases may hinder charge transfer at the two-phase interface and also may adversely affect the densification process and the mechanical strength of the composite electrolyte.

**2.3.3. Doped $CeO_2$ and carbonate composites.** Molten carbonates, commonly used as electrolytes in molten carbonate fuel cells (MCFCs), can serve as a sintering aid to lower the sintering temperature of ceria-based oxides. Additionally, composite electrolytes with ceria can provide a highway for proton conduction. Zhu *et al.* discovered that solid carbonate–ceria composite can achieve high dual ion conductivity, ranging from 0.001 to 0.2 S $cm^{-1}$ between 400 and 600 °C, making them suitable as electrolytes for low-and intermediate-temperature SOFCs.[220] As shown in Fig. 11b, a swing model of "Ce–O–H–O–C" was proposed for the proton conduction in the SDC/$Na_2CO_3$ composite, in which the interface in composite electrolyte provides high conductive path for proton and oxygen ions can transported by the SDC grain interiors.[213] Novel core–shell SDC/$NaCO_3$ nanocomposite achieved a high power density of 0.8 W $cm^{-2}$ at 550 °C, using $H_2$ as the fuel and air as the oxidant.[221] Another core–shell structure composite of undoped $CeO_2$ and alkali carbonate (Li/Na/$K_2CO_3$) was fabricated to use as electrolyte at low temperature SOFCs with excellent performance, achieving exceptional ionic conductivity of 0.34 S $cm^{-1}$ in air and 0.2 S $cm^{-1}$ in hydrogen gas at 550 °C.[222] This turned out that this composite electrolyte was proton and oxygen ions conduction, and the proton conductivity was lower than the oxygen conductivity during 450–550 °C. Besides, the excellent power density of 910 mW $cm^{-2}$ can be achieved on a single cell with this composite electrolyte at 550 °C. However, due to the carbonate, the sintering temperature of these composite electrolyte should be strictly controlled, normally lower than 650 °C, and the operating temperature also should be lower this value.[223] Moreover, the limited mechanical stability of molten carbonate raises significant concerns about the morphological, mechanical and interfacial stability of this composite electrolyte under fuel cell operation.[216] Besides, carbonate vaporization and decomposition during cell testing may lead to a decline in SOFC performance.

## 3. Efficient preparation and processing techniques for electrolyte

Electrolytes have a crucial role in both SOEC and SOFC as they facilitate the transfer of oxygen ions in oxygen ion-conducting SOECs and hydrogen ions in proton-conducting SOECs. These electrolytes should possess the following characteristics: (1) densification to enable separation of the hydrogen and fuel chamber; (2) high ion conductivity and electronic insulator to facilitate ion transformation and enhance the reaction activity;

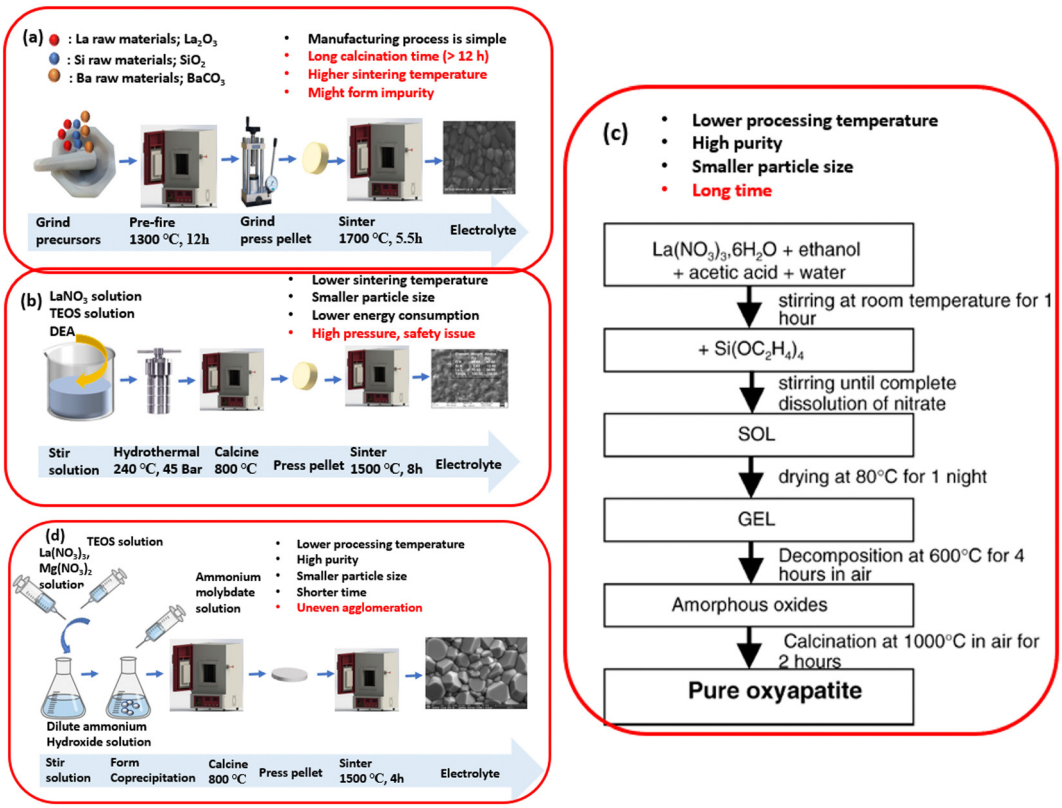


Fig. 12 A schematic of different electrolyte preparation methods: (a) solid-state reaction; (b) hydrothermal synthesis; (c) sol–gel process; (d) co-precipitation method; and the comparison of these methods.[224] Reproduced from ref. 224 with permission from [Elsevier], copyright [2005].

(3) stabilisation to maintain optimal properties under high oxygen pressure. The fabrication method can affect the electrolytes' microstructure and physiochemical, mechanical, and electrical properties. Hence, choosing suitable materials and preparation methods to synthesise the required electrolytes is essential. As shown in Fig. 12, there are four basic synthesis methods: solid-state; hydrothermal; sol–gel, and co-precipitation. Solid-state methods are commonly used at high temperatures, and the manufacturing process is relatively simple: mix the raw materials and calcine totally at high temperatures. The calcination and sintering temperatures are lower than in the solid-state reaction, which can decrease the energy consumption and the particle size to form uniform nanoparticles. In the following Sections 3.1.1–3.1.5, five such synthesise methods will be discussed.

### 3.1. Efficient synthesis methods for electrolyte materials

**3.1.1. Solid-state reaction.** A solid-state reaction is a conventional way to prepare dense electrolytes by mixing the raw reactants and allowing them to react by diffusion at a high temperature. This technique is widely used in solid oxides, powder materials, and ceramics as it is the simplest way. This method requires completely mixing the precursors in the form of oxides or carbonate, and repetitive cycles of grinding and heating steps are needed to achieve a complete reaction.[225] To facilitate this process, high temperatures ranging between 1000 and 1700 °C are required, which causes high cost and purified is not easy. Moreover, the reaction is quite slow since solid-state diffusion is limited.

The co-doped $La_{9.4}Ba_{0.6}Si_{6-x}W_xO_{27-\delta}$ ($x$ = 0, 0.05, 0.1, 0.15, 0.2) electrolytes were synthesised *via* a high-temperature solid-state reaction process using $La_2O_3$, $SiO_2$, $BaCO_3$, and $WO_3$ as raw materials, and then pressed samples were sintered at 1550 °C for 5.5 h and kept at 400 °C for 1 h.[226] This method is simple to operate, allowing for ion substitution into the lattice and producing good crystallinity, which resulted in the formation of the hexagonal $La_{10}Si_6O_{27}$ phase without any impurity $La_2SiO_5$. Jun Xiang *et al.* used a solid-state reaction to synthesise $La_{10}Si_{5.9}A_{0.1}O_{(27\pm\delta)}$ (A = $In^{3+}$, $Si^{4+}$, $Nb^{5+}$, $W^{6+}$) electrolytes, in which different oxide mixtures were wet mixed for 24 h and calcined at 1573 K for 5 h; cold isostatically pressed and sintered at 1923 K for 10 h to produce densified electrolytes.[227] However, lower ionic conductivities and higher activation energies were reported for using this method, compared with using other methods. It was reported that the grain boundary resistance accounted for more than 90% of the total resistance using this method and sintering at 1640 °C for 6 h, which led to low total conductivity.[228] Moreover, the impurities forming at high temperatures in the grain boundaries could block oxygen ions migration, such as the formation of $La_2Si_2O_7$ and $La_2SiO_5$ in the apatite phase leading to big grain boundary resistance and affecting the ionic conductivity when sintering at high temperatures to achieve good densification. High sintering temperatures also lead to huge problems when

co-firing the electrode and electrolyte, which decreases the electrode porosity.[229] Therefore, alternative synthesis methods have been proposed to overcome these drawbacks.

**3.1.2. Hydrothermal synthesis.** Another method is hydrothermal synthesis referring to the chemical reactions of substances in a sealed autoclave, heated solution above ambient temperature and pressure using water as the solvent.[230] The temperature should be beyond the boiling point of water to reach the vapour saturation pressure. This method is used for growing crystals with better crystallinity than those grown by other methods to obtain reproductivity.[231] Moreover, particle morphology, grain size and crystalline phase can be controlled by regulating reaction temperature, pressure, and time and composition of solution.[231] Due to its high reaction activity and ease of control, hydrothermal synthesis has gained increasing interest from scholars. This method is also beneficial for synthesising the electrolytes, resulting in less air pollution, lower energy consumption, and lower sintering temperature compared to traditional solid-state reactions. Hence, hydrothermal synthesis can be utilised to synthesise unstable phases at high temperatures and is an effective way to grow a single crystal.

Paramananda Jena *et al.* synthesised the nano-powders *via* the hydrothermal method, which exhibited high densification with negligible porosity for the $La_{10}Si_6O_{27}$ pellet after sintering at 1500 °C for 8 h and possessed a high electrical conductivity with a value of $1.09 \times 10^{-4}$ S cm$^{-1}$ at 500 °C.[232] Different particle sizes and morphologies of $Gd_xCe_{1-x}O_{2-\delta}$ (GDC) nanoparticles were synthesised by using continuous hydrothermal flow.[233] The nano size YSZ can be synthesised by this method and densified YSZ film can be obtained after sintering below 1000 °C without any cracks or holes, which was a relatively low sintering temperature.[234] The $Ce_{0.8}Sm_{0.2}O_{1.9}$ (SDC) powders were synthesised by hydrothermal and sol–gel methods, and results showed that there was not any sedimentation for the suspension using hydrothermally synthesised powders, while the high degree of SDC aggregation using sol–gel method decreased the density of thin file electrolytes.[235] Moreover, the hydrothermal reaction in Cerium and Gadolinium solution can improve the densification of the barrier layer, and as a result, the ohmic resistance can be decreased by 16.4% at 750 °C for electrolyte-supported symmetrical cells.[236]

**3.1.3. Sol–gel process.** The sol–gel process is a wet chemical technique that is used to prepare gels, glasses, and ceramic powders. Compared with traditional solid-state reactions and other methods, this process offers several desirable features such as a lower processing temperature, a high-purity process, and low cost. The procedure begins with the organometallic salts like the metal alkoxides for the hydrolysis of the liquid phase process, and then forming a gel.[237] With this method, reactants could be uniformly mixed at the molecular level, which could result in decreasing reaction temperatures and time. Additionally, it can be used to prepare dense ceramics with small grain sizes, large specific surface areas, and good reactive activity. As a result, this method could be utilised to produce the desired phase at low temperatures that are inaccessible *via* the solid-state reaction. The sol–gel process can typically be divided into several stages including forming a solution, gelation, drying, and densification.[238]

The one of advantages of this method is the possibility of doping different types of dopants, which possess a low-temperature sintering capacity of about 200–600 °C.[9] Stephane Celerier *et al.* proposed a sol–gel process for synthesising powders of apatite type-$La_{9.33}Si_6O_{26}$ by using silicon alkoxide and lanthanum nitride as precursors, which were beneficial to reduce the crystallisation temperature to 800 °C for pure apatite phase and result in the synthesis of reactive powders with nanometric particles size in comparison to the conventional methods.[239] The sol–gel method was also used to obtain solid solution samples of YSZ/$SrTi_xZr_{1-x}O_3$ to investigate their structure and electrophysical properties.[240] Using a novel sol–gel thermolysis method with a unique combination of urea and PVA, nano-crystalline $Ce_{0.9}Gd_{0.1}O_{1.95}$(GDC) powders were successfully prepared and showed better sinter ability as well as higher ionic conductivity with a value of $2.21 \times 10^{-2}$ S cm$^{-1}$ at 700 °C in the air after sintering.[241] However, it was reported that the samples using the sol–gel method exhibited lower conductivity and higher activation energies compared with solid-state reactions. For example, $Ce_{0.2}Sm_{0.8}O_{1.9}$ electrolyte preparation by sol–gel process revealed a lower sintering temperature (1400 °C) than that of solid state process (1650 °C), but the low conductivity (0.005 S cm$^{-1}$) and high activation energy (0.97 eV) also reported in this electrolyte at 600 °C.[242] The possible reason is the presence of impurities in the precursors and solvents to increase the grain boundary resistance, which needs detailed investigation and improvement.

**3.1.4. Co-precipitation method.** Coprecipitation is another wet chemical method to synthesise nanoparticles in an aqueous solution using inorganic salts, which could provide better control over the chemical compositions and the size distribution. Coprecipitation reactions involve the simultaneous occurrence of the growth, coarsening, and/or agglomeration process.[243] In this method, metal cations can be coprecipitated in different forms, like hydroxides, carbonates, bicarbonates, and oxalates, followed by calcination and decomposition.[244] The coprecipitation method makes the materials react uniformly at the molecular level to produce highly homogenous products and offers the advantages of lower polycrystalline synthesised temperature and shorter sintering time compared with other methods.[245] However, precipitation rates must remain similar to achieve coprecipitation and obtain the desired nanoparticles.

In oxalate coprecipitation, oxalate acid ($C_2H_2O_4$) is commonly used to form precipitates with metal cations, and the metal oxide can be obtained after calcinating. Oxalate precipitates exhibit good stability, and high production yields and its electrolyte powders were reported of high conductivity.[246–248] $Ce_{0.2}Sm_{0.8}O_{1.9}$ electrolyte can obtain a conductivity of 0.021 S cm$^{-1}$ at 600 °C *via* oxalate coprecipitation, while the conductivity was 0.005 S cm$^{-1}$ and 0.0094 S cm$^{-1}$ for using sol–gel and solid-state method, respectively.[249] However, the sintering temperature should be high to prepare a densified electrolyte for the oxalate coprecipitation. Carbonate precipitations using ammonium carbonate as the precipitant allow low agglomeration and result in nanoparticles

with lower sintering temperatures, compared with oxalate coprecipitations.[250] Nanometric powders of doped and co-doped ceria-based ceramics were prepared using a simple and cheap synthesis route, easily scalable on the industrial level based on an optimised co-precipitation process with ammonium carbonate as a precipitating agent. Ammonia solution is commonly used to react with metal nitrates to form hydroxide coprecipitates. This method can form pure and fine power at relatively lower temperatures, such as the pure apatite phase composition was obtained after calcining at 700 °C for 6 h, and densified electrolyte can be achieved at 1500 °C for 2 h.[251] Therefore, this is a low-temperature method and provides good control of morphological particles.[252] Reaction temperature may have effects on the particles' size, shape and sintering ability, which nano-size particles could facilitate the sinterability and make it possible to form densified electrolytes at relatively low temperatures.[253,254] Besides, low sintering temperatures provide the opportunity to fabricate thin electrolyte layers with submicron size and could show good grain boundary conductivity.[255]

**3.1.5. Other methods.** Electrolytes for SOECs can be prepared using various methods, such as wet methods-solution combustion,[256,257] solvothermal,[258,259] microwave synthesis,[260,261] thermal decomposition,[262] spray pyrolysis,[263] and radio frequency thermal plasma methods.[264] Ultrafine and homogeneous $La_{9.33+x}Si_6O_{26+3x/2}$ ($0 \leq x \leq 0.67$) were obtained by freeze-drying as reported in the literature.[265] It is crucial to consider chemical compatibility and low area-specific resistance when selecting an appropriate method for SOEC electrolytes, as different synthesis processes could result in electrolytes with varying structures, size distributions, and physical and chemical properties. Nanoscale electrolytes can effectively decrease the ohmic resistance and improve the ionic conductivity, due to the fast grain boundary diffusion of oxygen ions. Wet chemical routes involve the mixture of metal precursors in a solvent on the atomic level and reduce the diffusion path up to the nanometric scale which can promote substituting metal ions into atomic sites to improve the ionic conductivity, such as co-precipitation, spray-freezing, sol–gel and Pechini.[266] A core–shell SDC@$Y_2O_3$ nanocomposite synthesised by the co-precipitation method, which can give an ionic conductivity of 0.4–0.92 S $cm^{-1}$ in the temperature range of 300–600 °C and is higher than SDC electrolyte (0.1 S $cm^{-1}$) at 800 °C.[267]

### 3.2. Advanced electrolyte processing techniques for practical applications

The decrease in the thickness of electrolytes is essential to improve the performance of SOFCs and SOECs since the ohmic resistance is essential to the thickness of electrolytes. Electrode-supported and metal-supported cells are commonly used to decrease the thickness of electrolytes by coating thin film on the electrodes. Densified electrolytes with a micrometric scale (10–100 μm) can be obtained by thick film techniques, such as tape casting and slip casting, screen-printing, and spin coating which can minimise ohmic resistance and provide a high area/thickness ratio. The process of these deposition methods is shown in Fig. 13. However, these processes are not sufficient for thin electrolyte film and an additional sintering process is needed to obtain a densified electrolyte.[268] Therefore, advanced fabrication methods are applied to prepare the nanoscale electrolyte film, such as spark plasma sintering, flam spray deposition, chemical solution deposition (CSD), atomic layer deposition (ALD), pulsed laser deposition sputtering (PLD), physical vapour deposition (PVD) and chemical vapour deposition (CVD).[269] Table 4 summarises the advantages and disadvantages of the deposition method SOFC electrolyte, which can

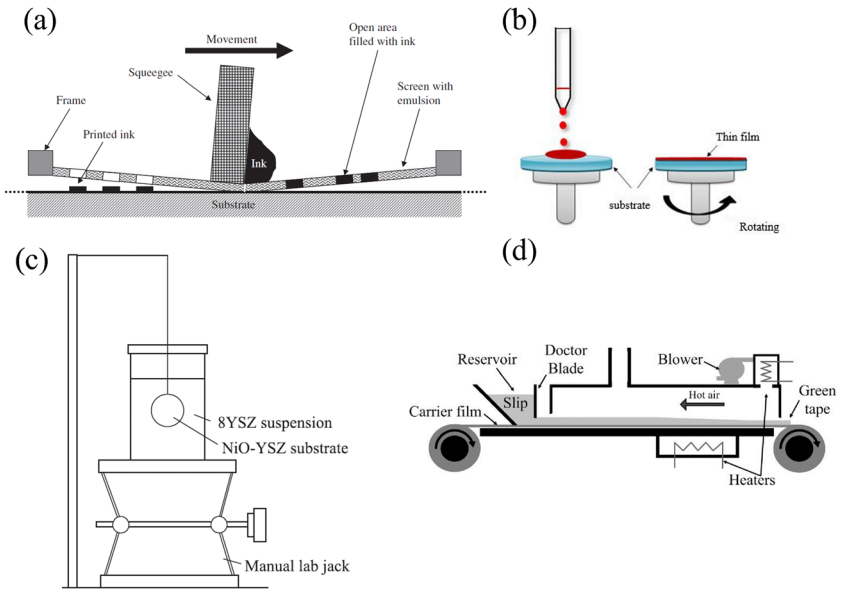


Fig. 13 Illustration of (a) the screen-printing process; (b) the spin-coating process; (c) the dip-coating process; and (d) the tape-casting process.[272–275] Reproduced from ref. 272 with permission from [Elsevier], copyright [2017]. Reproduced from ref. 273 with permission from [Elsevier], copyright [2009]. Reproduced from ref. 274 with permission from [Elsevier], copyright [2011]. Reproduced from ref. 275 with permission from [Elsevier], copyright [2017].

Table 4 An overview of each deposition method

| Deposition method | Advantage | Disadvantage | Ink content |
|---|---|---|---|
| Screen rinting<br>Thickness: 10–100 μm | • Easy fabrication method in large scale-up.<br>• Minimize the cracks if the ink is suitable. | • Only suitable for planar cells.<br>• Require high sintering temperature.<br>• Large shrinkage level during sintering. | • Binder (EC, PVA, PVB, PMMA, <1 wt%).<br>• Solvent (terpineol and texanol).<br>• Dispersant (1–4 wt%).<br>• Solid powder (>30 vol%). |
| Spin coating<br>Thickness: micro size (>10 μm) | • Easy and cheap process.<br>• Uniform thickness.<br>• Suitable in the lab scale. | • Limitation in the surface area.<br>• Not suitable for large scale. | • Binder (PVB, EC, PVA).<br>• Solvent (ethanol, terpineol, toluene).<br>• Dispersant (menhaden fish oil, phosphate ester).<br>• Plasticiser (polyethene glycol, butyl benzyl phthalate)<br>• Solid powder |
| Dip coating<br>Thickness: micro size (>10 μm) | • Low cost.<br>• Suitable for planar and tubular cells. | • Uncontrol the thickness.<br>• Picture framing effects near the edges. | • Binder (PVB, EC, PVA).<br>• Solvent (ethanol).<br>• Dispersant (menhaden fish oil, phosphate ester).<br>• Solid powder.<br>• Plasticiser (polyethylene Glycol, dibutylphthalate) |
| Tape casting<br>Thickness: micro size (>10 μm) | • The solution is less.<br>• The thickness can be controlled.<br>• Suitable for multilayer.<br>• Cost-effective. | • Slow dry process.<br>• A large shrinkage rate led to cracks. | • Binder (PVB, EC, PVA).<br>• Solvent (toluene, 2-propanol).<br>• Dispersant (menhaden fish oil, phosphate ester).<br>• Solid powder.<br>• Plasticiser (polyethylene Glycol, dibutylphthalate) |
| PVD<br>Thickness: nano size and 1 μm | • No need for further sintering.<br>• Thin film (can reach nano size).<br>• Low operation temperature. | • High cost.<br>• Require precise instruments.<br>• Low deposition rates.<br>• Low durability. | A solid material target. |
| CVD<br>Thickness: nano-size | • Form uniform, pure, reproducible and adherent films. | • High cost.<br>• Low deposition rates. | Mixed precursor solution |

present an overview of the fabrication method. A 1 nm thick single-crystalline YSZ electrolyte was prepared by ALD, which improved the power density by 150% at 400 °C.[270] Besides, an anode-supported cell with 100 nm YSZ film interlayer on a 400 nm-thick GDC electrolyte can be fabricated by the CSD method, of which the high power density of 1300 mW $cm^{-2}$ with good OCV (1 V) can be obtained at 650 °C.[271]

**3.2.1. Screen printing.** Screen printing is a flexible, simple and economical method to prepare the electrolyte film with a thickness of about 10–100 μm.[276] The main process includes (1) preparing the suitable ink, (2) feeding the inks into the open screen meshes, (3) flattening by squeegee with suitable force to form film and (4) drying and sintering process as shown in Fig. 13a.[277,278] The quality of films is intricately influenced by multiple factors, such as printer configuration, screen options, ink rheology and substrate preparation.[279–281] The ink rheology relies on binder, solvent, and dispersant, and the homogeneous ink mixture is important to fabricate good structure and morphology electrolyte film. It was reported that YSZ film with a thickness of 23–100 μm can be fabricated by using 0.3 MPa squeegee pressure, 150 mm $s^{-1}$ squeegee speed, and 2 mm snap-off distance.[282] Viscosity represents a rheological property in the static condition of ink, and it generally increases with the solid and binder content.[281,283] It has been reported that the viscosity between 4–12 Pa for YSZ inks is suitable for screen-printing measured with a shear rate of 100 $s^{-1}$.[284] The dispersion of ink can be identified by the thixotropy of the ink, which can be measured by the area of the hysteresis loop between the up-sweep and down-sweep of the viscosity-shear rate curve.[276] The poor thixotropic behaviour may produce cracked film after sintering, which is not suitable for screen-printing. The different binder content was investigated for the thixotropic and levelling behaviours of YSZ inks, which resulted in the ink having 0.5 vol% binder exhibiting better thixotropic and levelling properties compared with the binder contents of 0, 0.14, 0.36 vol%.[285] The yield stress is another rheological parameter that measures the relative strength of the

 

particle network in inks.[279] The yield stress increases with viscosity resulting in enhanced particle association in inks, but high viscosity and yield stress may impair the screen mesh and damage the screen.[276]

Besides, the rheological properties are affected by particle size, distribution of powder, solid content and the composition of ink. The determination of the maximum solid loading is also dependent on these factors. For example, the maximum applicable solid content was reported at about 50 and 45 vol% using surface areas of 4.31 ($d_{50}$ = 0.56 μm) and 6.01 ($d_{50}$ = 0.37 μm) $m^2\ g^{-1}$ for the YSZ inks with a constant binder content as 0.25 wt%, respectively.[284] The formulation of screen-printing inks employing nanoparticles may result in a low solid content attributable to a high surface area of powders, which increases interaction between particles and as a result the increase in the viscosity.[276] However, inks with high surface area powders exhibit a reduced particle packing density, thereby significant delamination and cracking after drying, which can be solved by mixing high surface powder ($>100\ m^2\ g^{-1}$) with a low surface area powder ($<10\ m^2\ g^{-1}$) to increase the particle packing density and enhance static and dynamic rheological properties.[286] he commonly used solvents for screen-printing are terpineol and texanol, and 94 wt% terpineol and 6 wt% of ethylene cellulose binder were used as vehicles in ink formulation.[287,288] Moreover, the binder is used to improve the particle network strength. Various binders have been employed in the ink formulation, such as ethylene cellulose (EC),[283,289,290] polyvinyl butyral (PVB),[284] polyvinyl acetal (PVA)[283] and polymethyl methacrylate (PMMA).[291] Viscosity increases with the length of the polymer molecule. Too high binder content may increase the tackiness of the inks and influence the printability, but a lower binder content may result in cracking. A higher solid content ($>30$ vol%) and lower binder content ($<1$ wt%) are commonly employed to enhance the relative density of electrolyte films.[276] In the case of dispersant, it is used to improve the separation of solid particles and prevent particle agglomeration, resulting in reducing the viscosity by forming an electrostatic or steric barrier around the particle surface.[290] The solid content can be increased in the ink formulation if adding dispersant, and subsequently, the relative density could be increased.[290] A low concentration of dispersant like 1–4 wt% of powder is suitable to produce a well-dispersed YSZ ink.[292] Overall, screen printing can be considered a promising method for SOFC component development. The cells with 30 μm SDC electrolyte fabricating by screen-printing can obtain 397 mW $cm^{-2}$ powder density at 600 °C.[293] However, this method is limited to planner SOFCs/SOECs configurations, requiring high sintering temperatures to obtain densified electrolyte films.

**3.2.2. Spin coating.** Spin coating is a simple wet ceramic method to fabricate the electrolyte film, in which the substrate is spun at a high and constant speed, and the centripetal acceleration makes the slurry spread and consequently produces a uniform film on the substrate as shown in Fig. 13b.[273,294,295] In most wet ceramic methods, a slurry includes a solvent (ethanol, terpineol, toluene, *etc.*), binder (PVB, EC, PVA, *etc.*), dispersant (menhaden fish oil, phosphate ester, *etc.*) and solid content (YSZ, GDC, LSO, *etc.*). There are two ways to add the slurry, applying a slurry on the surface of the substrate followed by spinning the substrate, another one is to add the slurry on the spinning substrate. The spin coating is normally used to fabricate multilayered electrolytes or electrodes on the supported substrate.[273] In the spin process, pivotal technical parameters influence the thickness of coating layers, such as slurry viscosity, coating cycles, and spinning speed.[296,297] Reducing the spin coating speed and increasing the coating cycles can increase the thickness of a spin-coated film. It was reported that a minimum spinning speed of 2500 rpm and 20 coating cycles were applied to obtain uniform 10 μm YSZ electrolyte films with dense and crack-free properties after sintering at 1300 °C for 5 h for intermediate temperature SOFCs.[296] The anode-supported YSZ films can be obtained by spin coating with 12–36 μm thickness, in which an OCV can be achieved at 1.06 V at 800 °C with the maximum power density of 2005 mW $cm^{-2}$.[297] A dense and pinhole-free SDC electrolyte film *via* five-cycle pin coating for anode-supported SOFCs and the maximum power density of 685 mW $cm^{-2}$ can be achieved at 600 °C.[298] In this work, the SDC slurry was fabricated with toluene, PVB and ethanol, and dried at 500 °C for 30 min after every coating cycle to repeat and achieve 10 μm thickness. A 2 μm thick GDC/YSZ bi-layer electrolyte can be obtained *via* the spin coating method, and its power output was 200 mW $cm^{-2}$ with OCV over 1 V at 600 °C.[299] Nevertheless, despite its cost-effectiveness as a method for fabricating the SOFCs/SOECs components, it is still frequently used on the laboratory scale, and questionable to apply in large-scale applications.

**3.2.3. Dip coating.** Dip coating is called slurry coating and is also a traditional wet ceramic fabrication method for thin electrolytes for a variety of geometric shapes including planar and tubular. It needs no expensive equipment and is a fast and cheap method for the mass production of SOEC/SOFC components.[273] This method has been optimised to fabricate both thin and dense electrolyte films by many works. The dip coating process includes several steps: the substrate is slowly submerged, kept, removed from the slurry, and then dried and sintered at high temperatures as shown in Fig. 13c. This cycle is normally repeated 5–10 times to obtain the dense and thin electrolyte films. YSZ electrolyte films with a thickness of 16 μm were fabricated by twice dip-coating with homogenous, crack-free and good adherent to the anode substrate, and this assembled single cell with YSZ film presented a good OCV of 1.01 V with a maximum power density of 262 mW $cm^{-2}$ at 800 °C.[300] Kim *et al.* employed the dip coating technique for the deposition of anode function layer and YSZ electrolyte layer.[301] The dipping and drawing speeds were kept at 300 and 50 mm $min^{-1}$, respectively, and the dwell period was about 25 s. This condition was used to prepare both the anode-supported layer and YSZ electrolytes. The results show that the dip-coated anode layer can enhance the TPB volume, and the polarisation resistance can decrease from 1.07 Ω $cm^2$ to 0.48 Ω $cm^2$ if the electrolyte thickness decreases from 10.5 μm to 6.5 μm, as a result of the maximum power density improved from 0.74 W $cm^{-2}$ to 1.12 W $cm^{-2}$ at 800 °C. However, the lack of complete control over the thickness makes it less attractive than other ceramic processing techniques.

**3.2.4. Tape casting.** Tape casting is also a wet ceramic process for the planar SOFC component of anode and bi-layer electrolytes. This method is stable, simple, and economical for mass production. As shown in Fig. 13d, the process begins with the preparation of slurry usually using ball milling, and then the de-airing process to remove the air bubbles by vacuum condition, followed by the slurry being cast in a tape casting machine to produce the required layers, and finally drying and sintering the coating layers at high temperatures.[237] In order to avoid any crack, delamination, deformation and mechanical failure on the coating layers, every step should proceed carefully, and the shrinkage behaviour is necessary to observe at the sintering step. The formulation and preparation of slurry play important roles in tape casting, which should be homogenous, free of agglomerates and have enough viscosity. Organic and aqueous-based slurries are commonly used in this method. The organic-based slurry is composed of ceramic powder (GDC, YSZ, LSO, *etc.*), binder (PVB), dispersant agent (triethanolamine TEA, triolein), plasticiser (PEG), and solvent (ethanol, toluene).[273] Aqueous tape casting is water-based and uses polymeric emulsion as binders without using hazardous and toxic solvents. The slurry using distilled water, YSZ and polymeric emulsion, exhibited fine compatible and stable properties in the tape casting process.[302] Ball milling is an effective way to mix and uniformise the composition of slurry. For example, YSZ powders, dispersant and solvent were ball milled for 24 h, followed by adding surfactant and binder to ball mill with 30 min, and uniform slurry can be used for the tape casting to obtain the tapes with 94.5% relative density after sintering.[303] Will *et al.* employed a water-based type casting method to fabricate a 0.6 μm YSZ electrolyte on the 200–250 μm NiO-YSZ anode with a relatively lower co-sintering temperature at 1350 °C.[304] Fu *et al.* utilised this technique to produce the Ni-GDC anode and coating GDC electrolyte *via* screen printing, and then co-sintering the electrolyte/anode bilayer to fabricate this cell, which its power density can rise to 953 mW $cm^{-2}$ at 650 °C.[305] This co-sintering bilayer was observed to improve the densification of GDC electrolyte, attributed to the pre-sintering anode substrate promoting homogeneity and mitigating mismatch among anode and electrolyte.

**3.2.5. Thin film processing-PVD.** Electrolyte materials require high operating temperatures due to low ionic conductivity at relatively low temperatures. Consequently, methodologies for the thinner films become imperative to mitigate the thickness of the electrolytes, as these thin films can decrease the ion conduction path and lower the operating temperatures. Thin films are generally fabricated by chemical or physical vapour deposition (CVD or PVD) with high-quality densification without further sintering. Vapour phase deposition is a method wherein a material undergoes evaporation, typically within a vacuum chamber, followed by its condensation on a substrate, resulting in the formation of deposited layer.[306] As shown in Fig. 14, the thin film electrolytes *via* PVD have a columnar grain that is perpendicular to the substrate, and its ionic conductivity is relatively high because of grain boundary effect can be reduced. The PVD processes include e-beam evaporation (EB-PVD), sputtering and pulsed laser deposition (PLD), in which the energy imparted to the target materials undergoes conversion into kinetic energy, subsequently transferred to the substrate and deposited as a thin film.[268]

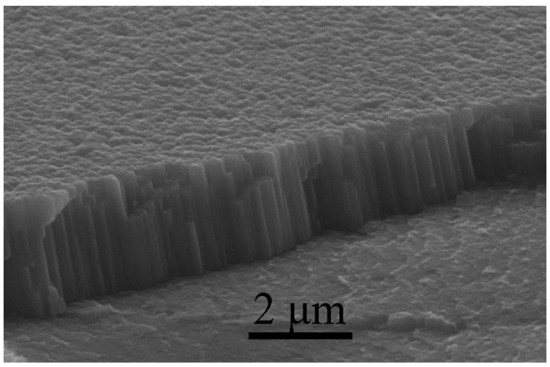


Fig. 14 PVD ceramic layer.[306] Reproduced from ref. 306 with permission from [Springer], copyright [2014].

The process of EB-PVD is initiated by employing an electron beam to melt down the materials, followed by the deposition of evaporated atoms onto the substrate. Thereby, a dense film can be obtained *via* the use of a high deposition rate. The mechanism of EB-PVD is shown in Fig. 15a, this method is the mean free path, which needs a very clean and high vacuum environment. A GDC film with 3 μm thickness was prepared *via* EB-PVD on the NiO-GDC anode substrate and its ionic conductivity was about 2.58 mS $cm^{-1}$ with 0.34 eV conduction activation energy.[307] YSZ thin film (1.5–2 μm) was deposited on three substrates to investigate the influence of substrate structure on YSZ films, which resulted in the dependence of substrate temperature, electron gun power has the influence on the crystallite size and texture of films, but the crystal orientation was irrelative with the substrate.[308]

There are two types of sputtering: direct current (DC) sputtering and radio-frequency (RF) sputtering, the DC sputtering is suitable for metallic targets, while RF sputtering is for ceramic or metallic targets, which means ceramic materials only can be fabricated by RF sputtering. The reason is that ionisation remains unhappened in the case of utilising a ceramic target for DC sputtering, and the cations accumulate on the target's surface and are subsequently discharged.[268] The sputtering process is illustrated in Fig. 15b and is influenced by the flow rate of Ar or $O_2$,[310] substrate bias,[311] deposition pressure and rate, RF or DC power,[312,313] and annealing temperature.[314,315] However, pinholes and cracks may form when sputtering on a porous electrode, because of the step coverage effect or shadow effect, which means that an annealing process is required to obtain the densified electrolytes.[316,317]

The PLD method is another physical technique proficient in enhancing the crystallisation process with the advantage of mass production of the thin film cell component. The important characteristic of PLD is that a thin film is formed on the substrate through the ablation of the target surface, thereby facilitating the preservation of the stoichiometric in muti-component materials as illustrated in Fig. 15c.[318] The thin film

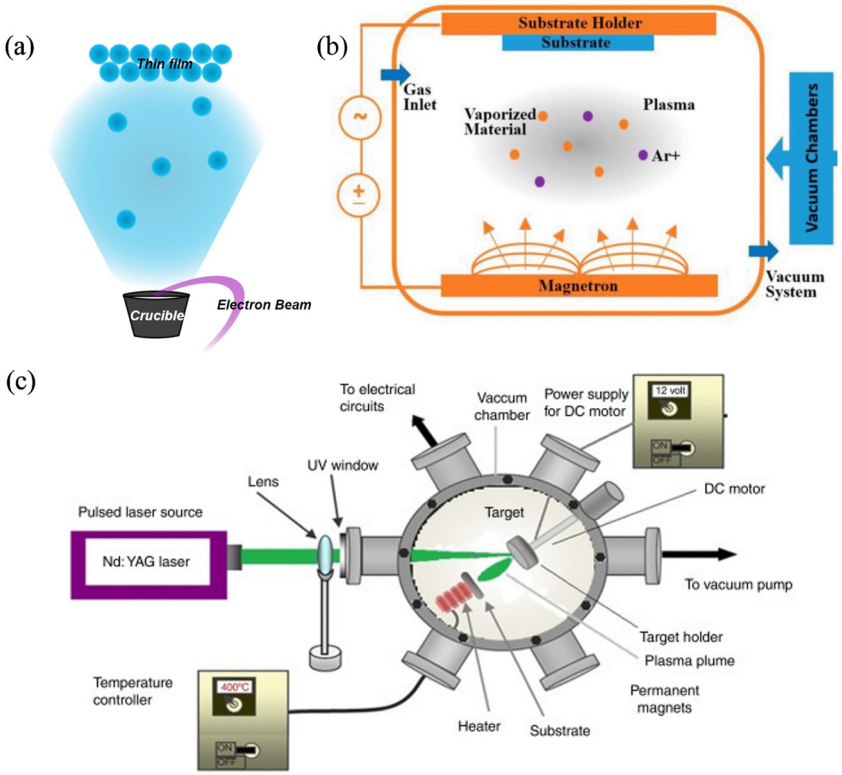


Fig. 15 Schematic illustration of the (a) EB-PVD, (b) sputtering, (c) PLD.[244,268,309] Reproduced from ref. 244 with permission from [Springer], copyright [2020]. Reproduced from ref. 309 with permission from [MDPI], copyright [2023].

can be affected by power density, wavelength, target composition and temperature for gas-surface interaction.[237] The process is heated around 400–700 °C to achieve the high quality of thin films.[319,320] Saporiti *et al.* fabricated thin films of YSZ and GDC with 1–3 μm thickness with fine grain boundaries about 100 nm which resulted in the formation of densified electrolytes.[321] SDC electrolytes also can be fabricated with this method using 650 °C thermal treatment and 10 Pa oxygen gas pressure, in which the conductivity was 0.075 S $cm^{-1}$ at 800 °C.[322]

**3.2.6. Thin film processing-CVD.** There are two main chemical deposition: chemical vapour deposition (CVD) and electrochemical vapour deposition (EVD), which are suitable for controlling the chemical composition and forming the densified film.[304] In essence, the operational mechanism of the CVD method commences with the evaporation of mixed precursor solution to generate gaseous precursor which is used to synthesise a solid material through a chemical process. When the chemical reaction occurs, the reactant vapour is delivered to the substrate surface and forms a thin film with crystallisation growth in a reaction chamber through either a high-temperature decomposition or a high-temperature chemical reaction. Following the completion chemical reaction, the densified film can be formed after the sintering process.[323] The CVD technique is favoured to form uniform, pure, reproducible and adherent films, but it needs high reaction temperature, has relatively low deposition rates, and presents corrosive gases if using a halogenous precursor.[324] Halogen compounds such as $ZrCl_4$, and $YCl_3$, metal–organic compounds such as metal alkoxides, or β-diketones are normally used as precursor materials.[304] Chour *et al.* used butanol containing Zr- and Y-ions as a precursor (heated to 150 °C) and sintered ceria pellets as the substrate (heated to 850 °C), and a 5 μm thickness of YSZ could be formed with 4 h deposition time and annealing at 1300 °C for 10 h, which an OCV of 0.93 V was reported at 650 °C.[325] Gelfond *et al.* used the volatile metal complexes with dipivaloylmethane $Zr(dmp)_4$ and $Y(dmp)_4$ as the precursors to fabricate the gas-tight YSZ electrolyte with the thickness of 4–15 μm on supporting porous YSZ/NiO anodes *via* CVD, where the OCV could achieve 0.98–1.08 V with 440 mW $cm^{-2}$ at 1073 K.[326]

EVD is a modified CVD process, which is easy to control and able to modify the interface of each component. As shown in Fig. 16a, there are two porous ceramic substrate chambers, where the first chamber is injected with oxygen gas as the reactant, and the other one is filled with metal chloride compound. The presence of an electrochemical potential gradient engenders the creation of a metal oxide because the oxygen reactant formed the water vapour side to react with metal chloride.[237] Finally, the solid thin film is deposited on the ceramic substrate. The film growth is affected by the temperature, the morphology of the porous substrate and chemical parameters. Hermawan *et al.* fabricated densified and gas-tight YSZ electrolyte film on metal-supported SOFCs.[327] However, the EVD process needs high reaction temperature, the presence of corrosive gases, and relatively low deposition rates.

To lower the operating temperatures, the thickness of the electrolyte should be decreased to nano size, atomic layer

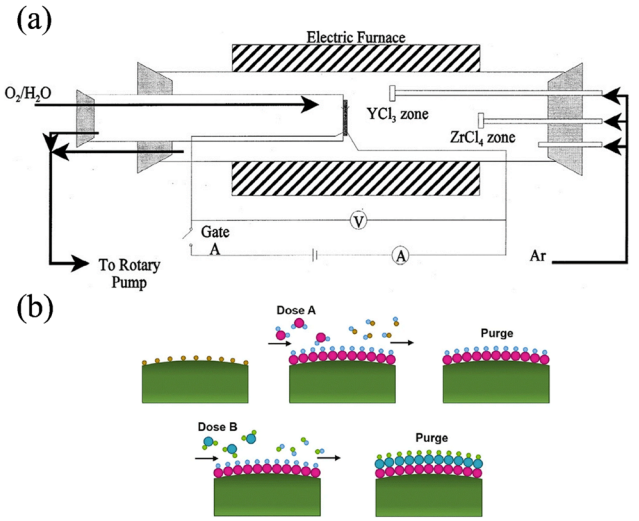


Fig. 16 The illustration of (a) the CVD reactor and (b) the ALD process.[237,268] Reproduced from ref. 237 with permission from [Springer], copyright [2020].

deposition (ALD) has the potential to grow nanoscale electrolytes, which allows very precise control over the thickness on an atomic level by self-limiting chemical reaction.[268] As shown in Fig. 16b, each ALD process has four steps by using layer-by-layer deposition while repeating the gas injection and purge. Thus, the thickness of the final deposition film is related to the number of precursor supply cycles, regardless of the supplied dose of the precursor.[244] Su *et al.* fabricated 10 nm YSZ film through the combination of two ALD processes, where this cell possessed a stable OCV of 1.05 V at 350 °C for 14 h.[328] The first noted GDC thin electrolyte deposited by ALD was reported in 2003, where sputtering-coated GDC was compared with ALD GDC thin layer (1 μm) and its ionic conductivity was 30 times higher than the sputtering method.[329] However, a low deposition rate and difficulty in deposition over large areas could lead to prohibiting a long operation time. Moreover, the low utilization of relatively precursor chemicals could increase the fabrication costs. These issues need to be solved for further practical industry applications.

Table 5 shows an overview of the different fabrication methods used to produce electrolyte layers in SOFC. The anode-supported cell is commonly used due to its ability to maintain mechanical performance, provide good stability, and exhibit low ohmic resistance with a thinner electrolyte layer compared to electrolyte-supported cells. Dip coating is used for tubular cells to deposit electrolytes and other functional layers. Spin coating, screen printing, and tape casting are used in planar cells to achieve micro-thickness layers, with screen printing being particularly suitable for large-scale applications. The cell with YSZ films produced by spin coating, with a thickness of 12–36 μm, can achieve a maximum power density of 2005 mW $cm^{-2}$, which is suitable in the laboratory.[297]

## 4. Strategies to modify the electrolyte performance

To be suitable for industrial applications, electrolyte materials should possess high ionic or protonic conductivity and good stability under operating conditions. One approach to improve stability is to lower the operating temperatures. Different types of electrolytes have been discussed in Section 2. Electrolytes are typically polycrystalline oxide, and oxygen vacancies are the primary charge carriers and proton conductivity is also closely related to oxygen vacancies. Therefore, introducing oxygen

Table 5 Overview of different fabrication methods for electrolytes in SOFC

| Type of SOFC | Cell configuration | Fabrication method of electrolyte | SOFC performance | Operating temperatures (°C) | Ref. |
|---|---|---|---|---|---|
| Anode-supported cell | NiO-SDC/SDC/$Sm_{0.5}Sr_{0.5}CoO_3$-SDC | Screen-printing | 397 mW $cm^{-2}$ | 600 | 293 |
| Anode-supported cell | NiO-8YSZ/8YSZ/LSM | Screen-printing | 1.5 A $cm^{-2}$ at 0.7 V | 800 | 330 |
| Anode-supported cell | NiO-8YSZ/8YSZ/LSCF | Screen-printing | 570 mW $cm^{-2}$ | 750 | 331 |
| Anode-supported cell | NiO-SDC/YSZ/$Y_{0.25}Bi_{0.75}O_{1.5}$-Ag | Spin coating | 535 mW $cm^{-2}$ | 750 | 296 |
| Anode-supported cell | NiO-YSZ/YSZ/LSM | Spin coating | 1567 mW $cm^{-2}$ | 750 | 297 |
| Anode-supported cell | NiO-SDC/SDC/LSCF | Spin coating | 685 mW $cm^{-2}$ | 600 | 298 |
| Anode-supported cell | NiO-YSZ/YSZ/GDC/LSCF-GDC | Spin coating | 200 mW $cm^{-2}$ | 600 | 299 |
| Anode-supported cell | NiO-YSZ/YSZ/Pt | Dip coating | 262 mW $cm^{-2}$ | 800 | 300 |
| Anode-supported cell | NiO-YSZ/YSZ/LSM-YSZ | Dip coating | 1120 mW $cm^{-2}$ | 800 | 301 |
| Anode-supported tubular cell | NiO-YSZ/YSZ/LSGM/$Sm_{0.5}Sr_{0.5}CoO_3$ | Dip coating | 274 mW $cm^{-2}$ | 600 | 332 |
| Anode-supported cell | NiO-GDC/GDC/GDC-LSCF | Tape casting | 953 mW $cm^{-2}$ | 600 | 305 |
| cathode-supported cell | SDC-NiO/SDC/$La_{0.7}Sr_{0.3}FeO_{3-\delta}$ | Tape casting | 233 mW $cm^{-2}$ | 750 | 333 |
| Anode-supported cell | NiO-BZCYYb/BZCYYb/LSCF-BZCYYb | Tape casting | 389 mW $cm^{-2}$ | 800 | 334 |
| Anode-supported cell | NiO-YSZ/YSZ/LSCF | Magnetron sputtering | 560 mW $cm^{-2}$ | 800 | 335 |
| Anode-supported cell | NiO-YSZ/YSZ/LSM | EB-PVD | 760 mW $cm^{-2}$ | 800 | 336 |
| Anode-supported cell | NiO-GDC/YSZ/GDC-LSCF | EB-PVD | 540 mW $cm^{-2}$ | 860 | 337 |
| Anode-supported cell | NiO-YSZ/YSZ/LSM | EB-PVD | 1000 mW $cm^{-2}$ | 900 | 338 |
| Anode-supported cell | NiO-YSZ/YSZ/LSM | CVD | 440 mW $cm^{-2}$ | 800 | 326 |
| | | | 1200 mW $cm^{-2}$ | 900 | |
| Anode supported cell | NiO-YSZ/YSZ/LSM | Electrophoretic deposition | 624 mW $cm^{-2}$ | 800 | 339 |
| Metal supported cell | Pt/YSZ/Pt | ALD | 270 mW $cm^{-2}$ | 350 | 340 |

SSFCu: $Sm_{0.5}Sr_{0.5}Fe_{0.8}Cu_{0.2}O_{3-\delta}$.

vacancies is critical for electrolytes, and dopants are effective and common methods to increase oxygen vacancies and improve stability and sintering ability at lower operating temperatures. As shown in Fig. 17a, co-doping Sm and Gd can increase the oxygen vacancy and the maximum concentration $(V_O^{\bullet\bullet})$ was $2.65 \times 10^{21}$ $cm^{-3}$ for $Ce_{0.8}Sm_{0.1}Gd_{0.1}O_{1.9}$ composition.[341] Different dopants have varying effects on the properties of electrolytes, with transition metals, rare earth metals, and alkaline earth metals commonly used. Typically, the ionic radius of the dopants is an important factor in determining performance, with higher conductivity achieved by doping with a similar ionic radius. However, dopants can also negatively affect performance by occupying the oxygen ion channel or capturing the moving oxygen ions. As shown in Fig. 17, the main strategies are doping cations, forming the bi-layer, decreasing the thickness of the electrolyte into nano-size and establishing the composite with two types of electrolytes. The strategies of doping or co-doping on conductivity have been discussed in detail in Section 2 and illustrated through different types of electrolytes.

### 4.1. Bi-layer strategy

An alternative approach to improve performance is to use bi-layer electrolytes. Although an excellent electrolysis performance has been achieved by using 8 mol% $Y_2O_3$ stabilised $ZrO_2$ as the electrolyte, Ni-YSZ, and LSM as the fuel electrode and oxygen electrode, respectively,[344] there is a need for higher and stable performance with cost reduction and successful implementation of the technology. To achieve this, superior electrode materials and stable electrolytes with sufficient conductivity are required, along with a reduction in the operating temperatures for the long term. However, there are some disadvantages to applying a single electrolyte layer. Such as, YSZ electrolyte is prone to react with the electrode materials LSCF and only provides sufficient conductivity at high temperatures (1000 °C); $Bi_2O_3$-based electrolyte can be reduced to metallic Bi at reduced atmosphere; $CeO_2$ electrolyte system could transfer to electronic conduction by reduction of $Ce^{4+}$ to $Ce^{3+}$ with high applied voltage in SOEC. Bi-layer electrolytes are an effective solution to solve these problems and can improve stability. For example, a bi-layered electrolyte ScSZ/GDC with high-performance LSCF can overcome unstable ScSZ and GDC electrolyte and obtain good electrolysis, in which this cell exhibited a very high electrolysis current density of approximately $-2.2$ A $cm^{-2}$ in steam, and the OCV was significantly improved, albeit at the cost of an increase in the ohmic resistance of the cell.[345] As shown in Fig. 18, anode-supported cell NiO + BZCYYb4411//BZCYYb4411//PBSCF (full formula is inside of figure) was fabricated *via* drop coating method, and a dense layer of PBSCF was deposited *via* PLD between the electrolyte and cathode, which can dramatically decrease ohmic resistance compared to the cells without PLD and improve the contact between cathode and electrolyte.[346] Bi-layer $SrCo_{0.3}Sn_{0.7}O_{3-\delta}$/$CeO_{2-\delta}$ can establish heterojunction, which improved the ionic conductivity from 0.11 S $cm^{-1}$ ($SrCo_{0.3}Sn_{0.7}O_3$ electrolyte) to

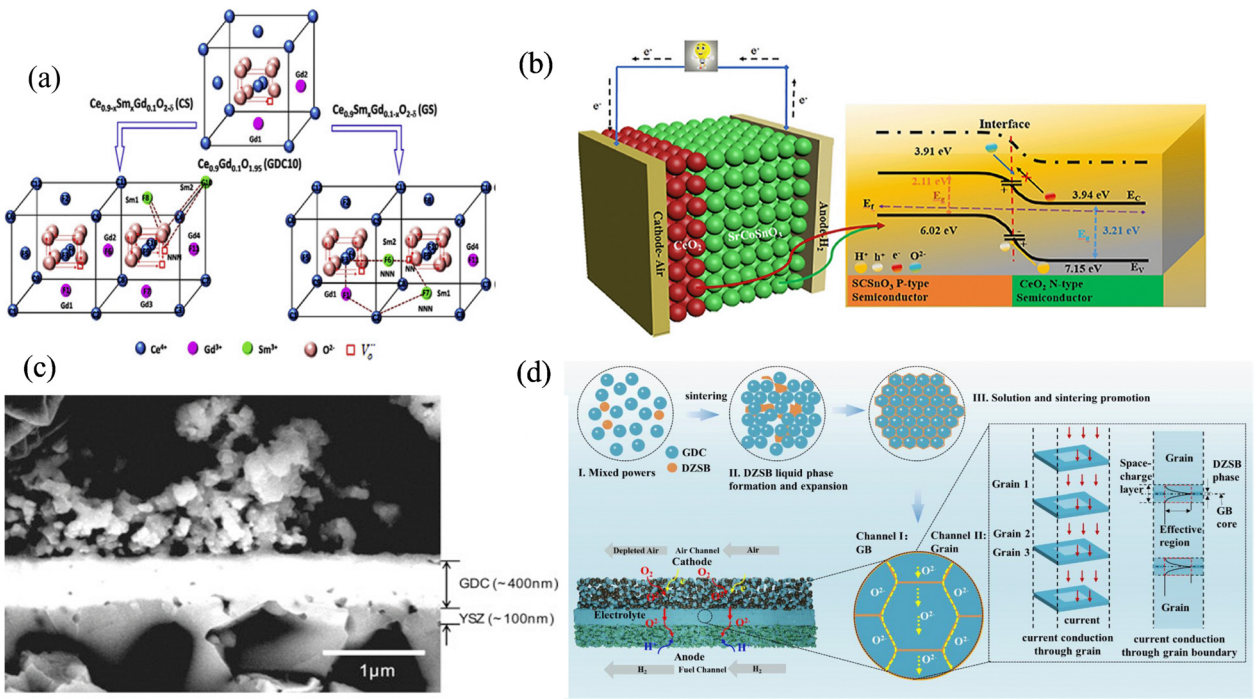


Fig. 17 The strategies of (a) co-doping of $Sm^{3+}$ and $Gd^{3+}$ in ceria strategies[341] and (b) bi-layer $SrCo_{0.3}Sn_{0.7}O_{3-\delta}$/$CeO_{2-\delta}$[342] and (c) thin electrolyte film[271] and (d) the composite of GDC and $(Dy_{0.2}Zr_{0.05}Bi_{0.75})_2O_3$.[343] Reproduced from ref. 341 with permission from [Elsevier], copyright [2020]. Reproduced from ref. 342 with permission from [Elsevier], copyright [2021]. Reproduced from ref. 271 with permission from [Wiley], copyright [2012]. Reproduced from ref. 343 with permission from [Elsevier], copyright [2024].

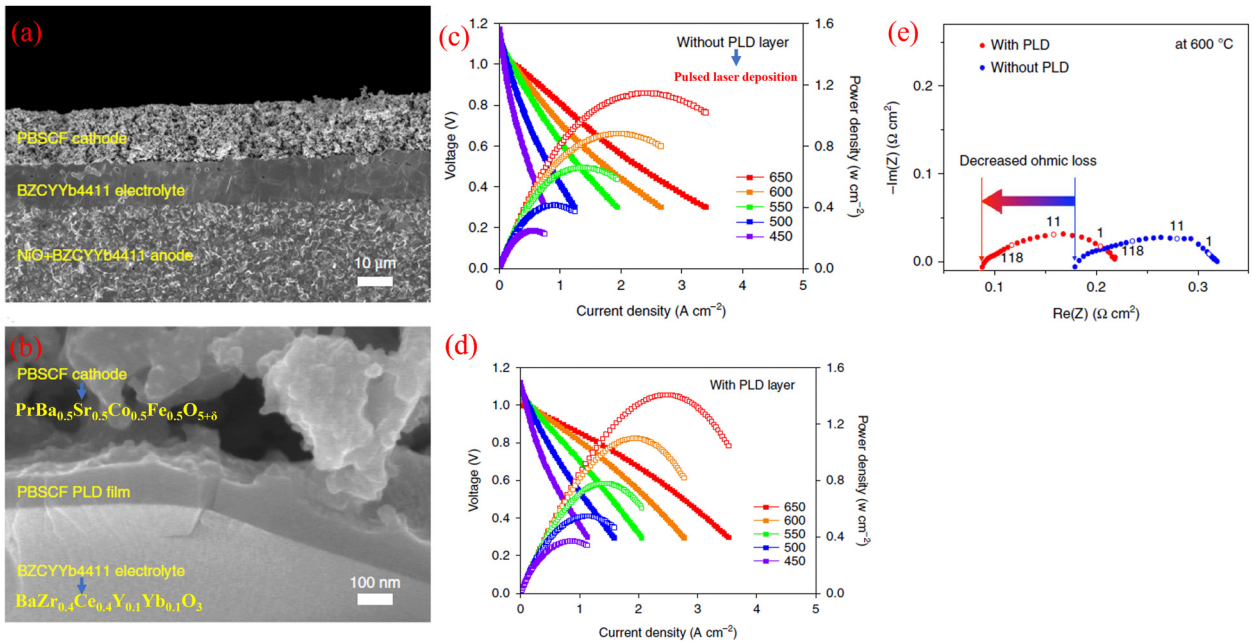


Fig. 18 Scanning electron microscope images of a cross-section of (a) PBSCF/BZCYYb/BZCYYb + NiO cermet anode fuel cell without PLD layer and (b) with PLD layer. The polarization and power density of cermet anode fuel cell (c) without PLD layer and (d) with PLD layer using humidified $H_2$ as fuel and dry air as oxidant. (e) Impedance spectra at 600 °C with and without PLD layer.[346] Reproduced from ref. 346 with permission from [Springer Nature], copyright [2018].

0.2 S cm$^{-1}$ at 520 °C and its heterojunction can block electronic transport through the cell.[342]

Various methods have been investigated to fabricate the dense bi-layer electrolyte, such as PLD, screen printing, sputtering, tape casting, and electrophoretic deposition.[183] The thickness of electrolytes has a great effect on the performance of SOFC. To reduce ohmic loss, the thickness should be minimised to reduce the resistance when YSZ is used as the blocking layer, such as the insertion of YSZ with 50–200 nm thickness could increase the power output from 377 mW cm$^{-2}$ to 1 W cm$^{-2}$.[347] Wachsman *et al.* investigated that Erbium or Yttria stabilised $Bi_2O_3$ (ESB or YSB) could be one of the electrolytes on the cathode and doped ceria electrolyte on the anode for SOFC, which could allow ESB/GDC bi-layered system to be used at low temperatures with high conductivity as well as high efficiency.[348] It was also reported that the ESB/GDC bilayer electrolyte can improve OCV and reduce the specific resistance of SOEC compared with single-layer GDC electrolyte, which is shown in Fig. 19, the thickness of the ESB film was about 4 μm and the maximum power density of bilayer SOFC was increased to 1.95 W cm$^{-2}$ with 0.079 Ω cm$^2$ total area specific resistance at 650 °C.[349] However, several challenges need to be addressed to apply bi-layer electrolytes in a practical solution, including shrinkage compatibility, thermal expansion coefficient (TEC) compatibility, and interdiffusion between the two components.[183]

### 4.2. Effect of microstructure

The total ionic resistance of polycrystalline electrolytes largely depends on grain and grain boundary, and it has been reported that the grain boundary conductivity is lower than grain conductivity by 2–3 orders of magnitude.[153] Grain boundaries refer to areas of crystallographic mismatch caused by lattice mismatch, impurities, space charge, microcracks, or a combination of all of these factors, which provide an area for faster mass transporting than bulk crystalline properties of crystalline.[350] The total conductivity can be enhanced by increasing the grain boundary conductivity. However, the impurities negatively affect the grain boundary conductivity, which can be eliminated by heating treatment or adding various additives. Recently, the ceria chloride electrolytes GDC-LiCl-$SrCl_2$ showed superionic conductivity, which was 2–10 times higher than GDC at the temperature of 400–600 °C.[351] The δ-$Bi_2O_3$-0.2 wt% $B_2O_3$ composite with molten grain boundary-based electrolyte can provide the highest oxygen ionic conductivity of 2 S cm$^{-1}$ at 750 °C with double layer, and the power density of the intermediate-temperature molten oxide fuel cell can theoretically obtain a value of 1 W cm$^{-2}$.[352] Therefore, the liquid phase or composite electrolyte can help enhance the grain boundary conductivity. The composite 0.5 wt% $Er_{0.2}Bi_{0.8}O_{1.5}$ (ESB) and $Ce_{0.85}La_{0.15}O_{1.925}$ (CLO) was reported the enhancement of ionic conductivity, which was an order of magnitude with a value of $1.41 \times 10^{-2}$ S cm$^{-1}$ at 600 °C compared to CLO and addition of ESB enhanced the conductivity of the bulk as well as grain boundaries.[341] Moreover, ESB also can decrease the sintering temperature, in which 5 wt% ESB-$Sm_{0.075}Nd_{0.075}Ce_{0.85}O_{2-\delta}$ (SNDC) achieved the high density (almost 100%) after sintering at 1100 °C and the power density of anode supported cell using 5ESB-SNDC as electrolyte can reach 129 mW cm$^{-2}$ at 450 °C.[353] As shown in Fig. 19d, A novel composite $(Dy_{0.2}Zr_{0.05}Bi_{0.75})_2O_3$ (DZSB)-GDC electrolyte was reported to reach more than 95% relative density after sintering at 1200 °C for 10 h and the sintering temperature

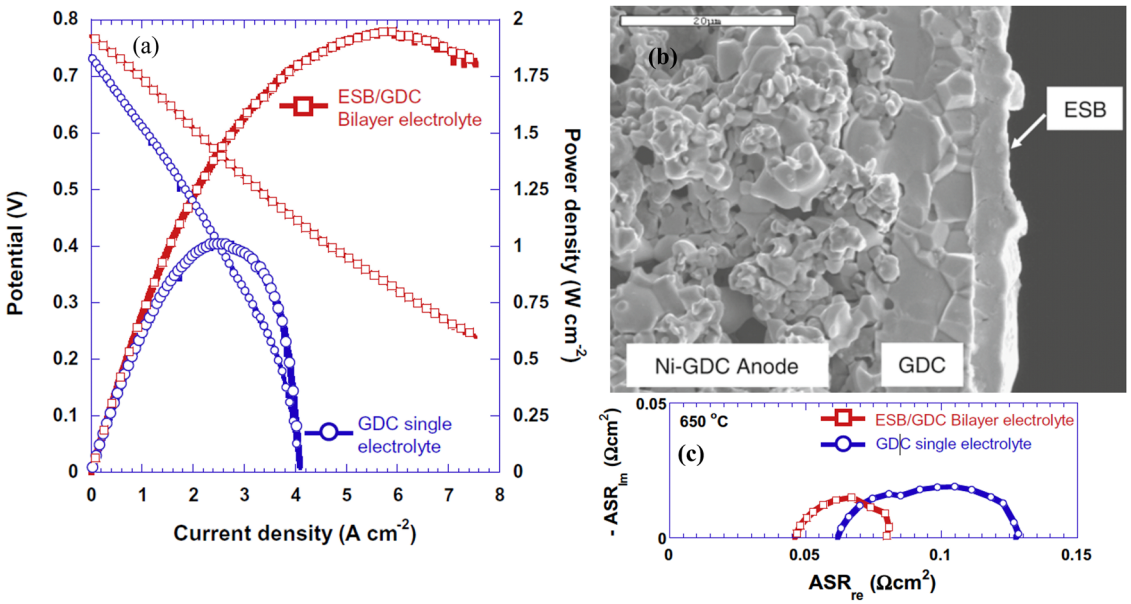


Fig. 19 *I–V* characteristics of fuel cell samples with single layer GDC and bilayer ESB/GDC electrolyte at 650 °C using 90 sccm of air and wet hydrogen. (b) SEM micrograph of the cross-section of ESB/GDC bilayer electrolyte with anode support. (c) Impedance spectra of the GDC and ESB/GDC electrolyte.[349] Reproduced from ref. 349 with permission from [Elsevier], copyright [2009].

can decrease with an increase in the DZSB composite ratio, due to the low melting point of DZSB around 825 °C to form the liquid phase, in which the grain boundary conductivity of 10 wt% DZSB-GDC was 113.8 times than pure GDC.[343]

The grain size also can affect the ionic conductivity with the nanosized electrolytes showing higher conductivity than micro-structure electrolytes. It was found that 16 mol% YSZ exhibited improved conductivity and lower activation enthalpy with nanocrystalline films (average 20 nm grain size) compared with coarse-grained polycrystals.[350] The ultra-fine grained (110–220 nm) and micron (1–1.8 μm)-Sm, Bi co-doping $CeO_2$/$BaCeO_3$ electrolytes were prepared, in which the specific grain-boundary conductivities were 1–2 orders higher than micron structures.[354] Doped ceria with an average particle size below 20 nm could obtain high density 99% sintering at a relatively low temperature of 1150 °C and higher conductivities at 500 °C, but the ionic conductivity could not show enhancement with a decrease in the grain size for the micro-level electrolytes (0.2–20 μm).[355] The effect of grain size should be further investigated with the assistance of simulation calculation due to the unclear grain boundary conduction behaviours.

As discussed in Section 2.2, the thickness of the electrolyte also influences the performance of the cell. The electrolyte thin film in nano size showed minimized ohmic resistance and grain boundary resistance at lower temperatures,[269] in which this electrolyte possesses a higher surface area to volume ratio than the bulk electrolyte. Advanced deposition methods are applied to prepare the nanoscale electrolyte film, such as CSD, ALD, PLD, PVD, and CVD.[269] It was reported that a 100 nm YSZ film on a 400 nm GDC electrolyte was deposited on Ni-based cermet support *via* the CSD method as shown in Fig. 19c, in which this cell showed a maximum power density of 1300 mW cm$^{-2}$ and high OCV (1 V) at 650 °C.[271] YSZ with 1 mm thickness was deposited to anode support and fabricated with Ni and Pt as the anode and the cathode, in which the maximum power density was 493 mW cm$^{-2}$ at 500 °C and high ionic conductivity of electrolyte was controlled by adjusting the sputtering pressure condition to obtain the large surface area and internal tensile stress.[356]

### 4.3. Other strategies

The synthesis method also has a great effect on the performances of solid oxide electrolytes, directly affecting their electrical and mechanical properties as well as the potential for large-scale production. Solid-state reaction is a common method to synthesise the electrolyte, but it requires high temperature and energy. Soft chemical synthesis of materials could make the targeted product at a relatively low temperature and with less energy consumption, like co-precipitation. However, the recycling of solvents should be considered. The choice of synthesis method could control the surface, porosity, and performance. It is better to choose a suitable method to synthesise the electrolyte. Some advanced manufacturing techniques, such as pulsed laser deposition, could improve performance by reducing the thickness. Developing good electrode materials compatible with electrolytes also plays a critical role in the performance of SOECs or SOFCs.

## 5. Thermomechanical and thermo-electrochemical characteristics of solid electrolyte

The electrolyte plays a vital role in SOECs and SOFCs, which should possess high ionic conductivity (0.1 S cm$^{-1}$ at operating

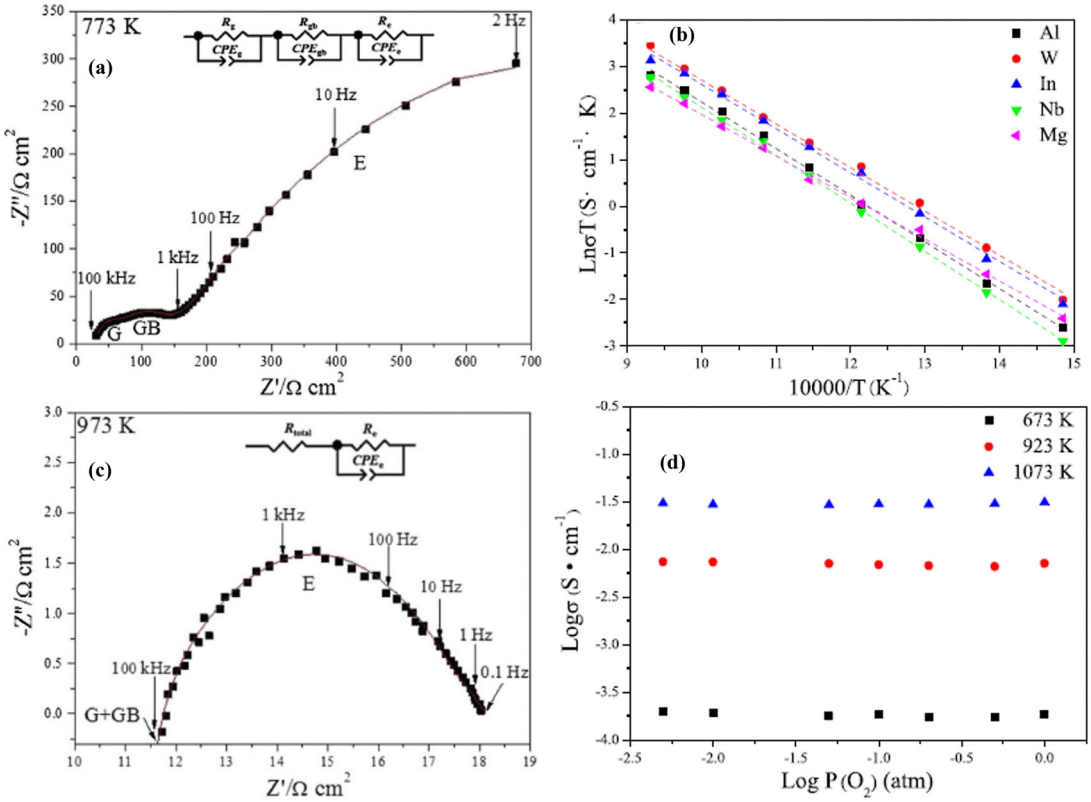


Fig. 20 Impedance spectra of $La_{10}Si_5Al_{1-x}W_xO_{27\pm\delta}$ ($x$ = 0–1) measured at (a) 773 K and (c) 973 K in the air; (b) Arrhenius plots of the total conductivity of the samples $La_{10}Si_5Al_{0.9}M_{0.1}O_{27-\delta}$ (M = W, In, Nb, Mg); (d) the total conductivity of sample $La_{10}Si_5Al_{0.9}W_{0.1}O_{27}$ as the function of the oxygen partial pressure at different temperatures.[211] Reproduced from ref. 211 with permission from [Elsevier], copyright [2016].

temperature); good densification (relative density >95%) to separate the gases; and reliable mechanical integrity with anode and cathodes. The total resistances are measured by electrochemical impedance spectroscopy (EIS) which is a normally used 2-probe method. The relative density can be calculated with skeletal density dividing absolute density, which is measured by the ASTM B962-17 method based on the Archimedes principle or mercury porosimeter, and helium pycnometer. The mechanical properties include microhardness, fracture toughness, and Young's modulus of the electrolyte. This section will cover the techniques for studying and developing electrolyte performances.

### 5.1. Conductivity measurement

The Pt or Ag pastes are commonly used as electrodes by coating on both sides of the electrolyte. In order to eliminate the influence of organics in the Pt or Ag pastes, it is better to calcine the cell at 500–800 °C for several hours. In the electrochemical impedance spectroscopy (EIS) measurements, the impedance is the function of the alternating current (AC), and a Nyquist plot displays the Impedance spectra by showing the imaginary part on the *Y*-axis and the real part on the *X*-axis at different frequencies.[123] The electrochemical impedance data were collected at different impedances from 400 to 800 °C, and three well-distinguished semicircles can be seen in Nyquist plots. The intercept on the real axis at higher frequencies represents the grain bulk resistance and this interception corresponds to the grain boundary resistance, and interface resistance between electrolyte and electrode at intermediate and low frequencies, respectively. At higher measurement temperatures (≥700 °C), the arcs contributed from both grain bulk and grain boundary disappeared due to the instrument limitation. Therefore, the intercept of the impedance arc with a real axis represents the total resistance at high frequencies. As shown in Fig. 20, these semicircles can be interpreted by equivalent circuits with a serial association of ($R$//CPE) elements, where $R$ is the resistance and CPE is a constant phase element. The conductivity can be calculated according to the resistances, and the activation energy ($E_a$) can be estimated by calculating the slope of the linear Arrhenius plots in Fig. 20c. The activation energy $E_a$ corresponds to migration reduces the energy barrier for oxygen ions diffusion across the electrolyte layer. The smaller activation energy indicated the smaller energy barrier to transport the oxygen ions.[357] Measuring the conductivity of samples at different oxygen partial pressures can verify the oxygen ions' conduction. As shown in Fig. 20d, the total conductivity is independent of the oxygen partial pressure, which implies the major charge carrier is oxygen ions rather than electronic defects.[211]

### 5.2. Densification measurement

The shrinkage/expansion behaviour can be measured by a dilatometer which can estimate the sintering temperature to

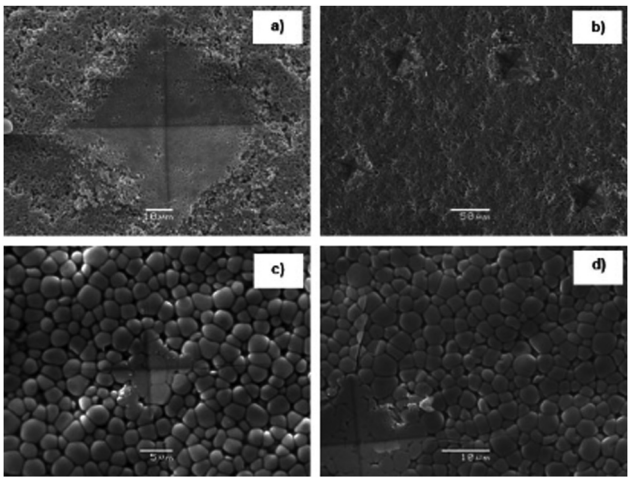


Fig. 21 The sample of $Ce_{0.9}Gd_{0.1}O_{1.95}$ of Pyramid-shaped Vickers indentation marks on tape sintered at (a) 1300, (b) 1400 °C/2 h, (c) and (d) indentation imprint and emanated crack on the tapes sintered at 1500 °C 2 $h^{-1}$.[358] Reproduced from ref. 358 with permission from [Wiley], copyright [2013].

obtain the dense electrolyte. After preparing dense electrolytes, the scanning electron microscope (SEM) can be used to measure the morphology of the surface and cross-section, where there should be no pores. The relative density should be above 95% to achieve separating gases at the anode and cathode. The relative density can be calculated by the following eqn (9):

$$\text{Relative density } (\%) = \frac{\text{Skeletal density}}{\text{Absolute density}} \quad (9)$$

where skeletal density can be estimated by a hand-made device according to the Archimedes principle and mercury porosimetry; absolute density can be measured by a helium pycnometer. Some literature also reported the use of the other eqn (10) to calculate the relative density:

$$\text{Relative density } (\%) = \frac{\text{Actual density}}{\text{Theoretical density}} \quad (10)$$

where the actual density can be measured by actual mass and volume; the theoretical density can be obtained according to the results of XRD refinement.

### 5.3. Mechanical measurement

The mechanical properties of the electrolyte in SOFCs are crucial. The electrolyte must maintain structural integrity under operational conditions, which include high temperatures and thermal cycling. If the electrolyte is too brittle, it can crack or fracture, leading to the failure of the fuel cell. Thus, maintaining a balance between thinness for ionic conductivity and sufficient mechanical strength to avoid brittleness and failure is essential.

When the thickness of electrolyte decreases to a small number, it will be brittle and introduce mechanical failure. Typically, electrolytes are kept at thicknesses around 10–20 micrometres to balance mechanical strength and ionic conductivity. Below this range, the brittleness increases, leading to a higher risk of mechanical failure. Advanced deposition techniques are used to optimize the mechanical properties while maintaining thin layers for better performance. A Shimatzu indentation equipment with a Vickers diamond indenter was used for the determination of Vickers microhardness ($H_v$) and fracture toughness of the electrolyte. The $H_v$ values were calculated by the following eqn (11):[341]

$$H_v = 1854.4P/a^2 \quad (11)$$

where $P$ is the applied load and a is the indentation diagonal distances (μm). The fracture toughness was determined by applying was determined by applying the Palmqvist method using the following eqn (12):[358]

$$K_{IC} = 0.016\left(\frac{E}{H_v}\right)^{1/2}\frac{P}{C^{3/2}}c = a + l \quad (12)$$

where $P$, $H_v$, $E$, $a$, and $c$ are the applied load, the Vickers hardness, the elastic modulus of the materials measured by a three-point bending test, and diagonal and crack length measured by SEM, respectively. The hardness is relative to the sintered density, the samples with lower porosity showed higher hardness, and Fig. 21 shows the indentation marks observed on the different sintered samples. The fracture toughness can be calculated with these cracks observed near the indentation zones.

The following eqn (13) can be used to calculate the reduced Young's modulus $E_r$:

$$E_r = \frac{1}{2}\sqrt{\frac{\pi}{A_c}}\frac{1}{C - C_f} \quad (13)$$

where $C$ is the compliance of the unloading part and $C_f$ is the frame compliance, $A_c$ is the contact area of the indentation immediately before unloading.[359] $E_r$ is the function of Young's modulus $E$, and the Poisson's ratio υ of the sample (s) and the indenter (i), through eqn (14):[360]

$$\frac{1}{E_r} = \frac{1 - \upsilon_s^2}{E_s} + \frac{1 - \upsilon_i^2}{E_i} \quad (14)$$

### 5.4. Stability measurement

Thermodynamic and chemical stability over a wide range of temperatures plays an important role for SOECs and SOFCs. The electrolyte should not react with the anode and cathode, and these components should possess a similar thermal expansion to avoid cracking. The thermal expansion can be estimated by dilatometer measurement, which can obtain the shrinkage temperature and rate. To evaluate the chemical stability, the electrolytes should be exposed to 20% $H_2$/Ar, wet Ar, or $CO_2$ at 800 °C for several hours and are analysed by XRD to check the structural changes or impurity phases. The morphology of the surface and cross-section is investigated *via* SEM and transmission electron microscopy (TEM) to estimate the interconnect with other components.

## 6. Large-scale stack applications

SOFC power technology offers several benefits, including superior energy conversation efficiency, minimal environmental

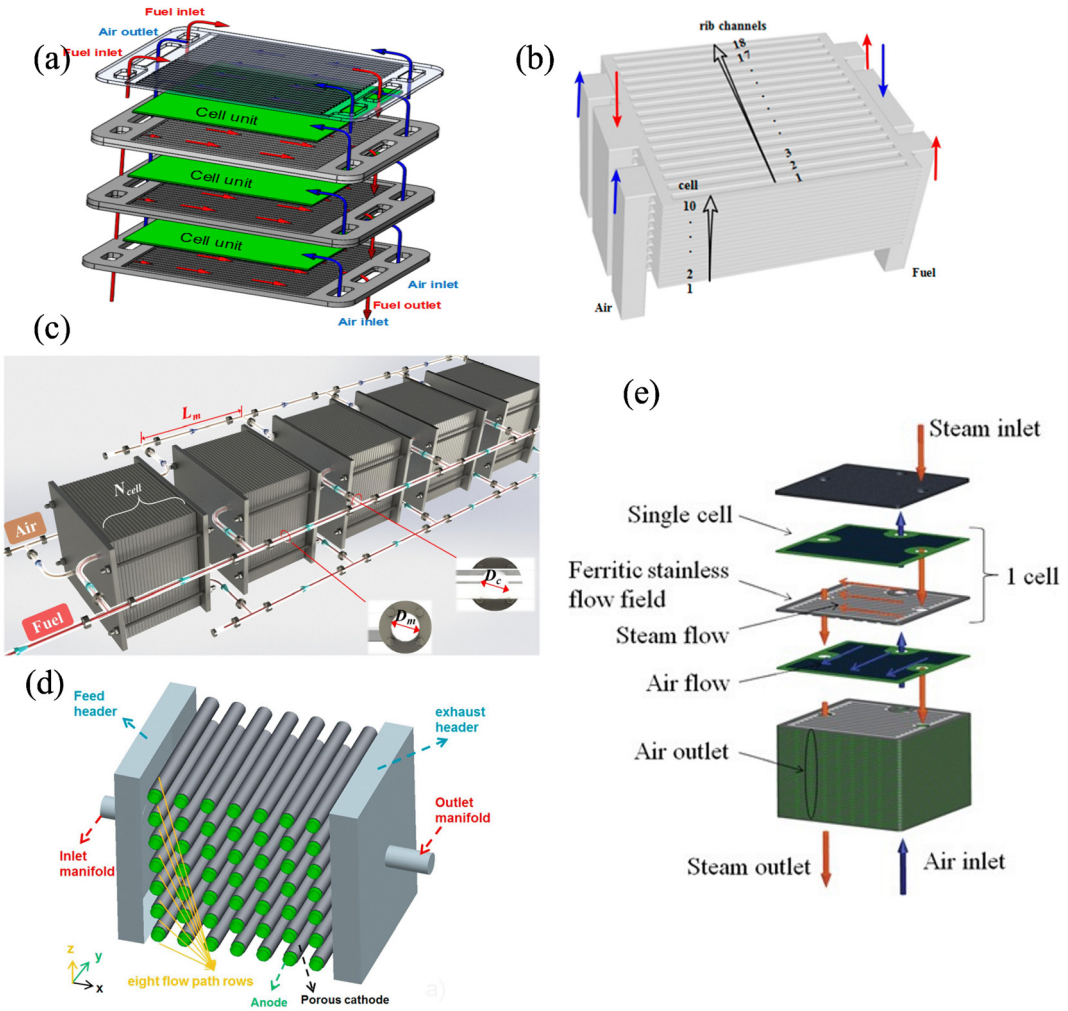


Fig. 22 (a) The schematic diagram of a planer SOFC stack with three cell unit; (b) 3D structure of the 10-cell SOFC stack; (c) the schematic diagram of an integrated muti-SOFC stack and (d) tubular SOFC stack with anode support and (e) 20-cell SOE stack.[362,363,365,366,368] Reproduced from ref. 362 with permission from [MDPI], copyright [2018]. Reproduced from ref. 363 with permission from [Elsevier], copyright [2023]. Reproduced from ref. 365 with permission from [Elsevier], copyright [2018].

footprint, and reduced noise levels when converting chemical energy into electrical energy. However, SOFCs need to achieve capacities in the megawatt and multi-megawatt range for application in the future energy system, which can be solved by increasing the active cell area and current density with stacks. Typically, dozens of planar cells and interconnectors are alternately assembled in a planar stack by incorporating appropriate sealing materials and porous current collector materials.[361] As shown in Fig. 22a, the conventional planar SOFC stack consists of electrolyte, porous electrodes, and gas flow paths where the solid bipolar plate serves multiple functions, including connecting cell units, current connector, separating the air and fuel flows as well as distributing the gases over cathode and anode surface by solid ribs.[362] The stack design mainly relies on the electrolyte, since the operating temperature is determined by the ionic conductivity of the electrolyte. The 3D structure of the 10-cell SOFC stack model is shown in Fig. 22b where red lines indicate the fuel flow within the stack and the blue lines for airflow, and the SOFC unit active area was about 100 × 105 mm using SDC/YSZ bi-layer as electrolyte.[362] The muti-SOFC stacks are also shown in Fig. 22c, which consists of 20 cells in each stack with a 100 $cm^{-2}$ cell area and 0.1 mm electrolyte thickness.[363] TOFC has collaborated with Wartsila since 2002 on the development of an SOFC system in the 200+ kW class for power generation and marine application, in which four stacks were installed and can be operated continuously providing an average power of 3.6 kW at 55–60% fuel utilisation.[364] As shown in Fig. 22d, the anode support tubular SOFC stack is constructed with 7 × 7 tubular cells in which 8YSZ served as the electrolyte with 1 mm thickness and the final active area was 205 $cm^2$.[364,365] Moreover, 30-cell SOE stack in Fig. 22e was operated at 750 °C under 0.5 A $cm^{-2}$ constant current density for more than 500 h with 4.06% k $h^{-1}$ degradation rate with high net hydrogen production rate 361.4 N L $h^{-1}$ and 73% steam conversion, in which each single cell consisted with 400 μm NiO-YSZ electrode substrate, 10 μm NiO-YSZ electrode functional layer, a 10 μm 8YSZ electrolyte and 2 μm GDC barrier layer and 20–30 μm

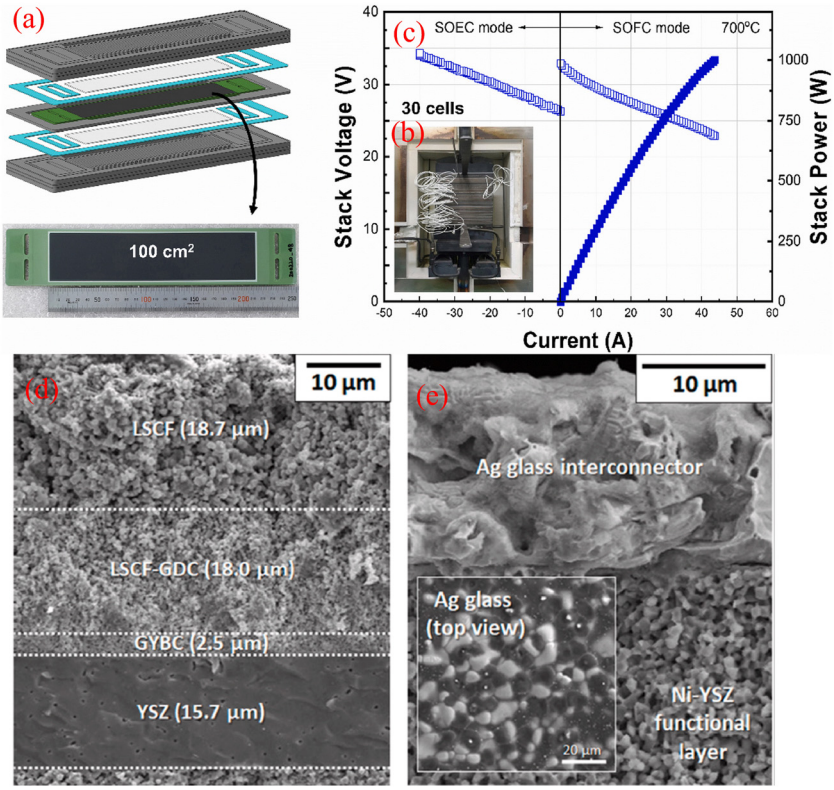


Fig. 23 (a) Schematic diagram of reversible SOC with repeating cell units; (b) photograph of 1 kW class stack; (c) *I–V* curves of both SOEC and SOFC mode for 30-cell stack at 700 °C; (d) and (e) cross-section SEM image of the cell area and Ag glass interconnector.[369] Reproduced from ref. 369 with permission from [Elsevier], copyright [2022].

LSCF-GDC oxygen electrode.[366] A multi-SOEC stack with 720 of 10 cm × 10 cm cells was conducted in a newly developed 15 kW integrated laboratory scale test facility; the test test-average $H_2$ production was about 1.2 $Nm^3\ h^{-1}$ based upon current with a peak value of 5.7 $Nm^3\ h^{-1}$.[367,368]

Reversible solid oxide cells (r-SOC) are a great option for highly efficient energy supply and production of fuel gases. The components of cassette-type r-SOC stack and single cell with 101.2 ± 0.1 $cm^2$ average active area are shown in Fig. 23a, e and f, in which the 15.7 μm YSZ served as the electrolyte with 2.5 μm $Gd_{0.135}Yb_{0.01}5Bi_{0.02}Ce_{0.83}O_{1.195}$ (GYBC) diffusion barrier layer; the photograph of 30-cell stacks are shown in Fig. 23c, which 1 kW of stack power can be achieved at 43.7 A at 700 °C in SOFC mode and 502 L $h^{-1}$ of $H_2$ production rate at −40 A in SOEC mode.[369] The key requirements for the industrial scale of r-SOE application are cell stability and durability, as well as reliability of power supply and hydrogen production. The YSZ electrolytes are normally chosen in a large-scale stack for industrial application, due to good ionic conductivity and mechanical ability to improve the cell stability, but the thin GDC barrier layer should be added to avoid the reaction between LSCF and YSZ if using LSCF as the oxygen electrodes. Moreover, varying operational conditions can lead to performance decline and microstructural deterioration in both SOFC and SOEC modes, which will reduce the r-SOC lifespan.[370,371] The detailed performance of the cells in the stack can be analysed with electrochemical impedance spectroscopy (EIS) in combination with the method of distribution of relaxation times (DRT), which can provide useful information for early-stage degradation detection.[372,373]

## 7. Conclusion and perspectives

This review specifically centres on the electrolyte for SOEC and SOFC, which offers an excellent method for hydrogen production and electricity generation. The discussion focuses on the synthesis methods for electrolytes; the various types of electrolytes (oxygen ion conduction and proton conduction); strategies to decrease the operating temperature and enhance stability and conductivity; the characterisation techniques of the electrolyte properties; and the YSZ electrolyte used as the large-scale SOEC and SOFC application. Additionally, the review also summarises the methods to modify the electrolytes for performance improvement.

- Proton-conducting electrolytes exhibit considerable conductivity at low temperatures (400–600 °C), but the performance of the cells is not satisfactory with one type of electrolyte. Ba/$SrCeO_3$-based electrolytes offer good proton conductivity but lack good chemical stability when exposed to an atmosphere containing $CO_2$, $SO_2$, and $H_2O$. Conversely, Ba/$SrZrO_3$-based electrolytes demonstrate robust chemical stability but poor proton conductivity. The combination of two types of electrolytes could compensate for their limitations and deliver good conductivity and stability. One well-known example of a

dual ion-conducting electrolyte is $BaZr_{0.1}Ce_{0.7}Y_{0.1}Yb_{0.1}O_{3-\delta}$ which exhibits both oxygen ion conductivity as well as proton conductivity at 500 °C while maintaining good sintering ability.

• Oxygen ion conductivity must be as high as 0.1 S $cm^{-1}$ at operating temperature to satisfy the SOECs or SOFCs requirement. Among these, stabilised zirconia-based electrolytes possess high stability and good conductivity at high operation temperatures, but low conductivity at low to intermediate temperatures. The $Bi_2O_3$-based electrolytes, on the other hand, exhibit good ionic conductivity at intermediate temperatures but are prone to reduce to metallic Bi, which limits their further application in IT-SOECs. Doped cerium oxide-based electrolytes are suitable for intermediate temperatures, but the reduction of $Ce^{4+}$ to $Ce^{3+}$ can lead to internet short-circuiting and block its application. For the perovskite-based electrolyte, the ionic conductivity is not good when compared with another electrolyte at IT temperature. To enhance conductivity and stability, a bilayer approach is often employed. GDC/YSZ bi-layer electrolytes are commonly used in SOECs or SOFCs and can achieve a power density of 1450 mW $cm^{-2}$ at 800 °C.

• Dual-ion conducting electrolytes, which facilitate the transport of both protons ($H^+$) and oxygen ions ($O^{2-}$), offer significant potential for improving the efficiency and flexibility of SOFCs. These materials enable enhanced ionic conductivity, particularly at intermediate temperatures, and can contribute to reduced operational temperatures while maintaining high performance. Key challenges remain in optimising the balance between proton and oxygen ion conductivity, ensuring chemical stability, and addressing issues related to phase compatibility. Continued development of dual-ion conductors could lead to more efficient, durable, and cost-effective SOFC technologies for energy conversion applications.

• In addition to the aforementioned material systems, there are other factors that impact cell performance. It is important to optimise the thickness of electrolytes to minimise the polarisation resistance; prepare the nanoparticles that exhibit high density at low sintering temperatures; and ensure good contact with electrodes to avoid interface resistance which can be influenced by the coating methods of cathodes and anodes. The factors that affect cell performance are numerous, including gas environment; synthesis methods; electrodes; cell configuration; and cell preparation.

• Wet chemical techniques are recommended to synthesise the electrolyte powders, such as the sol–gel and co-precipitation methods, since reactants are easy to react at the atomic level with these methods and nanoparticles can be achieved to decrease the ohmic resistances of electrolytes. For commercial electrolytes with large-scale applications, screen coating is suggested for the electrolyte deposition with the purpose of forming thin thickness (5–15 μm) with small ohmic resistance.

• Characterisation plays an important role in better choosing the proper electrolyte for SOECs and SOFCs. A good electrolyte should possess properties with high ionic conductivity (0.1 S $cm^{-1}$ at operating temperature); good densification (relative density >95%) to separate the gases; reliable mechanical integrity with anode and cathodes; and good stability.

From the perspective of synthesis electrolytes, co-precipitation, and sol–gel methods would be commonly effective to obtain uniform and nano-size particles. It is vital to consider chemical compatibility and low area-specific resistance when selecting an appropriate method for electrolytes in SOECs or SOFCs. The traditional synthesis by solid-state and solutions methods has some limitations during synthesis, such as high synthesis temperature, impurity, and relatively bigger particle size. The auto-combustion method was considered to be the most convenient and effective method to synthesise the electrolyte, since the ultrafine, high purity and homogenous nano-powders can be formed *via* this method at the relatively low sintering temperature, and the method is economical and energy efficient. Another effective method is microwave heating with fast-heating speed, which can reduce the sintering densification temperatures, improve the microstructures, reduce the activation energy between grain boundaries and improve the conductivities. However, it is not clear about the specific reasons why microwave heating can promote conductivities, which should be investigated further. Acceptor dopants were extensively used to stabilise the phase and increase the oxygen defects to improve the ionic conductivity, which was found to be affected by ionic radius, the charge valence of dopants, and the doping amount. The increase in oxygen vacancy concentration is an effective way to increase the ionic conductivity and co-doping can decrease the densification temperature as well as increase the ionic conductivity. Recently, a new way has been set up by triple-doping to enhance the ionic conductivity of ceria, such as La/Pr/Sm triple-doped ceria and Pr/Sm/Gd triple-doped ceria However, further investigation is needed in tri- or muti-doped ceria in order to develop new electrolytes for further SOECs and SOFCs application. A buffer layer also should be required to improve the stability and mechanical compatibility when electrolytes may react with the anode, but the thickness should be thin to avoid the increase in ohmic resistance. Finally, the oxygen ion transfer numbers also play *n* very important role in the oxide ionic conductivity, which could decrease the operating temperature if the ion transfer numbers are high. Still, we need to develop new electrolyte materials with good stability, mechanical properties, and ionic conductivity as well as cathode and anode materials with good performance to make commercially viable IT-SOECs and IT-SOFCs. It is still a big challenge to develop electrolytes with good conductivity, chemical stability, and mechanical ability. The main challenges of the operation of SOECs are the sealing problems and thermal and chemical stresses at electrolyte–electrode interfaces which may cause delamination. Additionally, the migration of oxygen ions or protons is not yet fully understood; and further simulations and experiments are necessary to address this issue.

## Data availability

The data supporting this article have been included in the manuscript, and the references cited. The authors also provide any further details and data upon request. The paper doe does not apply any coding or software application. The authors

declare that they have no known competing financial interests or personal relationships that could have appeared to influence the work reported in this paper. Signed on behalf of the authors of this work.

## Conflicts of interest

The authors declare no conflict of interest.

## Acknowledgements

This work was supported by the University of Surrey and the China Scholarship Council. The authors thank Yi Gong (ATI) for providing useful suggestions to write this review.

## References

1 W. Liu, Y. Cui, X. Du, Z. Zhang, Z. Chao and Y. Deng, High Efficiency Hydrogen Evolution from Native Biomass Electrolysis, *Energy Environ. Sci.*, 2016, **9**, 467–472.
2 J. D. Holladay, J. Hu, D. L. King and Y. Wang, An Overview of Hydrogen Production Technologies, *Catal. Today*, 2009, **139**, 244–260.
3 J. R. Rostrup-Nielsen, J. Sehested and J. K. Nørskov, Hydrogen and Synthesis Gas by Steam- and $CO_2$ Reforming, *ChemInform*, 2002, **47**, 65–139.
4 J. Liu, Y. Liu, N. Liu, Y. Han, X. Zhang, H. Huang, Y. Lifshitz, S.-T. Lee, J. Zhong and Z. Kang, Metal-Free Efficient Photocatalyst for Stable Visible Water Splitting Via a Two-Electron Pathway, *Science*, 2015, **347**, 970–974.
5 P. P. Edwards, V. L. Kuznetsov, W. I. David and N. P. Brandon, Hydrogen and Fuel Cells: Towards a Sustainable Energy Future, *Energy Policy*, 2008, **36**, 4356–4362.
6 A. Hauch, S. D. Ebbesen, S. H. Jensen and M. Mogensen, Highly Efficient High Temperature Electrolysis, *J. Mater. Chem.*, 2008, **18**, 2331–2340.
7 H. Cheng, B. Huang, J. Lu, Z. Wang, B. Xu, X. Qin, X. Zhang and Y. Dai, Synergistic Effect of Crystal and Electronic Structures on the Visible-Light-Driven Photocatalytic Performances of $Bi_2O_3$ Polymorphs, *Phys. Chem. Chem. Phys.*, 2010, **12**, 15468–15475.
8 L. Dunyushkina, S. Belyakov and N. Filatov, Proton-Conducting Alkaline Earth Hafnates: A Review of Manufacturing Technologies, Physicochemical Properties and Electrochemical Performance, *J. Eur. Ceram. Soc.*, 2023, **43**, 6681–6698.
9 S. Hossain, A. M. Abdalla, S. N. B. Jamain, J. H. Zaini and A. K. Azad, A Review on Proton Conducting Electrolytes for Clean Energy and Intermediate Temperature-Solid Oxide Fuel Cells, *Renewable Sustainable Energy Rev.*, 2017, **79**, 750–764.
10 E. Fabbri, D. Pergolesi and E. Traversa, Materials Challenges toward Proton-Conducting Oxide Fuel Cells: A Critical Review, *Chem. Soc. Rev.*, 2010, **39**, 4355–4369.
11 M. Ni, M. K. Leung and D. Y. Leung, Technological Development of Hydrogen Production by Solid Oxide Electrolyzer Cell (Soec), *Int. J. Hydrogen Energy*, 2008, **33**, 2337–2354.
12 Y. Zheng, J. Wang, B. Yu, W. Zhang, J. Chen, J. Qiao and J. Zhang, A Review of High Temperature Co-Electrolysis of $H_2O$ and $CO_2$ to Produce Sustainable Fuels Using Solid Oxide Electrolysis Cells (Soecs): Advanced Materials and Technology, *Chem. Soc. Rev.*, 2017, **46**, 1427–1463.
13 S. E. Wolf, F. E. Winterhalder, V. Vibhu, L. B. de Haart, O. Guillon, R.-A. Eichel and N. H. Menzler, Solid Oxide Electrolysis Cells–Current Material Development and Industrial Application, *J. Mater. Chem. A*, 2023, **11**, 17977–18028.
14 O. Yamamoto, Solid Oxide Fuel Cells: Fundamental Aspects and Prospects, *Electrochim. Acta*, 2000, **45**, 2423–2435.
15 A. B. Stambouli and E. Traversa, Solid Oxide Fuel Cells (SOFCs): A Review of an Environmentally Clean and Efficient Source of Energy, *Renewable Sustainable Energy Rev.*, 2002, **6**, 433–455.
16 L. Ye and K. Xie, High-Temperature Electrocatalysis and Key Materials in Solid Oxide Electrolysis Cells, *J. Energy Chem.*, 2021, **54**, 736–745.
17 N. Mahato, A. Banerjee, A. Gupta, S. Omar and K. Balani, Progress in Material Selection for Solid Oxide Fuel Cell Technology: A Review, *Prog. Mater. Sci.*, 2015, **72**, 141–337.
18 M. Sadeghi, M. Jafari, Y. S. Hajimolana, T. Woudstra and P. Aravind, Size and Exergy Assessment of Solid Oxide Fuel Cell-Based $H_2$-Fed Power Generation System with Alternative Electrolytes: A Comparative Study, *Energy Convers. Manage.*, 2021, **228**, 113681.
19 P. Aguiar, C. Adjiman and N. P. Brandon, Anode-Supported Intermediate Temperature Direct Internal Reforming Solid Oxide Fuel Cell. I: Model-Based Steady-State Performance, *J. Power Sources*, 2004, **138**, 120–136.
20 W. Dönitz and E. Erdle, High-Temperature Electrolysis of Water Vapor—Status of Development and Perspectives for Application, *Int. J. Hydrogen Energy*, 1985, **10**, 291–295.
21 J. Udagawa, P. Aguiar and N. Brandon, Hydrogen Production through Steam Electrolysis: Control Strategies for a Cathode-Supported Intermediate Temperature Solid Oxide Electrolysis Cell, *J. Power Sources*, 2008, **180**, 354–364.
22 N. Q. Minh, Ceramic Fuel Cells, *J. Am. Ceram. Soc.*, 1993, **76**, 563–588.
23 B. C. Steele and A. Heinzel, Materials for Fuel-Cell Technologies, *Nature*, 2001, **414**, 345–352.
24 S. Zhu, Y. Wang, Y. Rao, Z. Zhan and C. Xia, Chemically-Induced Mechanical Unstability of Samaria-Doped Ceria Electrolyte for Solid Oxide Electrolysis Cells, *Int. J. Hydrogen Energy*, 2014, **39**, 12440–12447.
25 N. Van Eck and L. Waltman, Software Survey: Vosviewer, a Computer Program for Bibliometric Mapping, *Scientometrics*, 2010, **84**, 523–538.
26 K. Hooshyari, B. Amini Horri, H. Abdoli, M. Fallah Vostakola, P. Kakavand and P. Salarizadeh, A Review of Recent Developments and Advanced Applications of High-

Temperature Polymer Electrolyte Membranes for Pem Fuel Cells, *Energies*, 2021, **14**, 5440.

27 P. Majumdar and S. K. Penmetsa, Solid Oxide Fuel Cell: Design, Materials, and Transport Phenomena, *Nanomater. Energy*, 2012, **1**, 247–264.

28 N. Sammes, G. Tompsett, H. Näfe and F. Aldinger, Bismuth Based Oxide Electrolytes—Structure and Ionic Conductivity, *J. Eur. Ceram. Soc.*, 1999, **19**, 1801–1826.

29 B. Singh, S. Ghosh, S. Aich and B. Roy, Low Temperature Solid Oxide Electrolytes (LT-SOE): A Review, *J. Power Sources*, 2017, **339**, 103–135.

30 T. Ishihara, H. Matsuda and Y. Takita, Doped $LaGaO_3$ Perovskite Type Oxide as a New Oxide Ionic Conductor, *J. Am. Chem. Soc.*, 1994, **116**, 3801–3803.

31 P. Vinchhi, M. Khandla, K. Chaudhary and R. Pati, Recent Advances on Electrolyte Materials for SOFC: A Review, *Inorg. Chem. Commun.*, 2023, 110724.

32 Z. Zakaria, S. H. Abu Hassan, N. Shaari, A. Z. Yahaya and Y. Boon Kar, A Review on Recent Status and Challenges of Yttria Stabilized Zirconia Modification to Lowering the Temperature of Solid Oxide Fuel Cells Operation, *Int. J. Energy Res.*, 2020, **44**, 631–650.

33 H. Shi, C. Su, R. Ran, J. Cao and Z. Shao, Electrolyte Materials for Intermediate-Temperature Solid Oxide Fuel Cells, *Prog. Nat. Sci.: Mater. Int.*, 2020, **30**, 764–774.

34 D. Saebea, S. Authayanun, Y. Patcharavorachot, N. Chatrattanawet and A. Arpornwichanop, Electrochemical Performance Assessment of Low-Temperature Solid Oxide Fuel Cell with YSZ-Based and SDC-Based Electrolytes, *Int. J. Hydrogen Energy*, 2018, **43**, 921–931.

35 B. S. Prakash, S. S. Kumar and S. Aruna, Properties and Development of Ni/YSZ as an Anode Material in Solid Oxide Fuel Cell: A Review, *Renewable Sustainable Energy Rev.*, 2014, **36**, 149–179.

36 M. Mogensen, N. M. Sammes and G. A. Tompsett, Physical, Chemical and Electrochemical Properties of Pure and Doped Ceria, *Solid State Ionics*, 2000, **129**, 63–94.

37 P. n Huang and A. Petric, Superior Oxygen Ion Conductivity of Lanthanum Gallate Doped with Strontium and Magnesium, *J. Electrochem. Soc.*, 1996, **143**, 1644.

38 A. Mohammadi, A. L. Smirnova and N. M. Sammes, *Mechanical Properties of Lsgm as an Electrolyte for Solid Oxide Fuel Cells*, International Conference on Fuel Cell Science, Engineering and Technology, 2008, pp. 61–64.

39 K.-D. Kreuer, Proton-Conducting Oxides, *Annu. Rev. Mater. Res.*, 2003, **33**, 333–359.

40 Z. Yang, M. Guo, N. Wang, C. Ma, J. Wang, M. Han and A. Short, Review of Cathode Poisoning and Corrosion in Solid Oxide Fuel Cell, *Int. J. Hydrogen Energy*, 2017, **42**, 24948–24959.

41 W. Wang, D. Medvedev and Z. Shao, Gas Humidification Impact on the Properties and Performance of Perovskite-Type Functional Materials in Proton-Conducting Solid Oxide Cells, *Adv. Funct. Mater.*, 2018, **28**, 1802592.

42 A. Pandiyan, A. Uthayakumar, R. Subrayan, S. W. Cha and S. B. Krishna Moorthy, Review of Solid Oxide Electrolysis Cells: A Clean Energy Strategy for Hydrogen Generation, *Nanomater. Energy*, 2019, **8**, 2–22.

43 Y. Meng, J. Gao, Z. Zhao, J. Amoroso, J. Tong and K. S. Brinkman, Recent Progress in Low-Temperature Proton-Conducting Ceramics, *J. Mater. Sci.*, 2019, **54**, 9291–9312.

44 S. Patel, F. Liu, H. Ding, C. Duan and I. Ghamarian, On Proton Conduction Mechanism for Electrolyte Materials in Solid Oxide Fuel Cells, *Int. J. Hydrogen Energy*, 2023, **72**, 1236–1248.

45 G. Ma, T. Shimura and H. Iwahara, Ionic Conduction and Nonstoichiometry in $Ba_xCe_{0.90}Y_{0.10}O_{3-\alpha}$, *Solid State Ionics*, 1998, **110**, 103–110.

46 Y.-J. Gu, Z.-G. Liu, J.-H. Ouyang, F.-Y. Yan and Y. Zhou, Structure and Electrical Conductivity of $BaCe_{0.85}Ln_{0.15}O_{3-\Delta}$ (Ln= Gd, Y, Yb) Ceramics, *Electrochim. Acta*, 2013, **105**, 547–553.

47 N. Sharova and V. Gorelov, Characteristics of Proton-Conducting Electrolytes $BaCe_{1-x}Nd_xO_{3-\Delta}$ ($0 \leq x \leq 0.16$) in Moist Air, *Russ. J. Electrochem.*, 2005, **41**, 1001–1007.

48 E. Gorbova, V. Maragou, D. Medvedev, A. Demin and P. Tsiakaras, Investigation of the Protonic Conduction in Sm Doped $BaCeO_3$, *J. Power Sources*, 2008, **181**, 207–213.

49 N. Maffei, L. Pelletier, J. Charland and A. McFarlan, An Ammonia Fuel Cell Using a Mixed Ionic and Electronic Conducting Electrolyte, *J. Power Sources*, 2006, **162**, 165–167.

50 C. Chen and G. Ma, Proton Conduction in $BaCe_{1-x}Gd_xO_{3-\alpha}$ at Intermediate Temperature and Its Application to Synthesis of Ammonia at Atmospheric Pressure, *J. Alloys Compd.*, 2009, **485**, 69–72.

51 N. I. Matskevich and T. A. Wolf, The Enthalpies of Formation of $BaCe_{1-x}Re_xO_{3-\Delta}$ (Re = Eu, Tb, Gd), *J. Chem. Thermodyn.*, 2010, **42**, 225–228.

52 W. Wang, J. Liu, Y. Li, H. Wang, F. Zhang and G. Ma, Microstructures and Proton Conduction Behaviors of Dy-Doped $BaCeO_3$ Ceramics at Intermediate Temperature, *Solid State Ionics*, 2010, **181**, 667–671.

53 M. Y. Wang, L. G. Qiu and G. L. Ma, Ionic Conduction in $Ba_{0.95}Ce_{0.8}Ho_{0.2}O_{3-\alpha}$, *Chin. J. Chem.*, 2007, **25**, 1273–1277.

54 J. Yin, X. Wang, J. Xu, H. Wang, F. Zhang and G. Ma, Ionic Conduction in $BaCe_{0.85-x}Zr_xEr_{0.15}O_{3-\alpha}$ and Its Application to Ammonia Synthesis at Atmospheric Pressure, *Solid State Ionics*, 2011, **185**, 6–10.

55 L.-G. Qiu and M.-Y. Wang, Ionic Conduction and Fuel Cell Performance of $Ba_{0.98}Ce_{0.8}Tm_{0.2}O_{3-\alpha}$ Ceramic, *Chin. J. Chem. Phys.*, 2010, **23**, 707.

56 S. Yamaguchi and N. Yamada, Thermal Lattice Expansion Behavior of Yb-Doped $BaCeO_3$, *Solid State Ionics*, 2003, **162**, 23–29.

57 N. I. Matskevich, T. Wolf, M. Y. Matskevich and T. I. Chupakhina, Preparation, Stability and Thermodynamic Properties of Nd-and Lu-Doped $BaCeO_3$ Proton-Conducting Ceramics, *Eur. J. Inorg. Chem.*, 2009, 1477–1482.

58 T. Norby, Proton Conductivity in Perovskite Oxides, *Perovskite Oxide for Solid Oxide Fuel Cells*, Springer, 2009, pp. 217–241.

59 M. Amsif, D. Marrero-Lopez, J. Ruiz-Morales, S. Savvin, M. Gabás and P. Nunez, Influence of Rare-Earth Doping on the Microstructure and Conductivity of $BaCe_{0.9}Ln_{0.1}O_{3-\Delta}$ Proton Conductors, *J. Power Sources*, 2011, **196**, 3461–3469.

60 P. Pasierb, E. Drożdż-Cieśla, R. Gajerski, S. Łabuś, S. Komornicki and M. Rękas, Chemical Stability of $Ba(Ce_{1-x}Ti_x)_{1-y}Y_yO_3$ Proton-Conducting Solid Electrolytes, *J. Therm. Anal. Calorim.*, 2009, **96**, 475–480.

61 M. Talimi and V. Thangadurai, Electrical Conductivity and Chemical Stability of Perovskite-Type $BaCe_{0.8-x}Ti_xY_{0.2}O_{3-\delta}$, *Ionics*, 2011, **17**, 195–200.

62 X. Chi, J. Zhang, Z. Wen and Y. Liu, Modified Pechini Synthesis of Proton-Conducting $Ba(Ce,Ti)O_3$ and Comparative Studies of the Effects of Acceptors on Its Structure, Stability, Sinterability, and Conductivity, *J. Am. Ceram. Soc.*, 2014, **97**, 1103–1109.

63 F. Zhao, Q. Liu, S. Wang, K. Brinkman and F. Chen, Synthesis and Characterization of $BaIn_{0.3-x}Y_xCe_{0.7}O_{3-\Delta}$ ($x$ = 0, 0.1, 0.2, 0.3) Proton Conductors, *Int. J. Hydrogen Energy*, 2010, **35**, 4258–4263.

64 C. Zhang and H. Zhao, Influence of in Content on the Electrical Conduction Behavior of Sm-and in-Co-Doped Proton Conductor $BaCe_{0.80-x}Sm_{0.20}In_xO_{3-\Delta}$, *Solid State Ionics*, 2012, **206**, 17–21.

65 N. Yan, Y. Zeng, B. Shalchi, W. Wang, T. Gao, G. Rothenberg and J.-L. Luo, Discovery and Understanding of the Ambient-Condition Degradation of Doped Barium Cerate Proton-Conducting Perovskite Oxide in Solid Oxide Fuel Cells, *J. Electrochem. Soc.*, 2015, **162**, F1408.

66 S. Wang, J. Shen, Z. Zhu, Z. Wang, Y. Cao, X. Guan, Y. Wang, Z. Wei and M. Chen, Further Optimization of Barium Cerate Properties Via Co-Doping Strategy for Potential Application as Proton-Conducting Solid Oxide Fuel Cell Electrolyte, *J. Power Sources*, 2018, **387**, 24–32.

67 M. Hakim, C.-Y. Yoo, J. H. Joo and J. H. Yu, Enhanced Durability of a Proton Conducting Oxide Fuel Cell with a Purified Yttrium-Doped Barium Zirconate-Cerate Electrolyte, *J. Power Sources*, 2015, **278**, 320–324.

68 S. Yang, Y. Wen, S. Zhang, S. Gu, Z. Wen and X. Ye, Performance and Stability of $BaCe_{0.8-x}Zr_{0.2}In_xO_{3-\Delta}$-Based Materials and Reversible Solid Oxide Cells Working at Intermediate Temperature, *Int. J. Hydrogen Energy*, 2017, **42**, 28549–28558.

69 S. Tao, J. T. Irvine and A. Stable, Easily Sintered Proton-Conducting Oxide Electrolyte for Moderate-Temperature Fuel Cells and Electrolyzers, *Adv. Mater.*, 2006, **18**, 1581–1584.

70 J.-S. Park, J.-H. Lee, H.-W. Lee and B.-K. Kim, Low Temperature Sintering of $BaZrO_3$-Based Proton Conductors for Intermediate Temperature Solid Oxide Fuel Cells, *Solid State Ionics*, 2010, **181**, 163–167.

71 J. Gao, Y. Liu, Y. Meng, M. Hu and K. S. Brinkman, Fluoride-Based Anion Doping: A New Strategy for Improving the Performance of Protonic Ceramic Conductors of the Form $BaZrO_3$, *ChemElectroChem*, 2020, **7**, 2242–2247.

72 U. Aarthi and K. S. Babu, Grain Boundary Space Charge Modulation in $BaZr_{0.8}Y_{0.2-x}M_xO_{3-\Delta}$ with Transition Metal (M = Ni, Co, Fe, and Zn) Co-Doping, *Int. J. Hydrogen Energy*, 2020, **45**, 29356–29366.

73 D. Han, X. Liu, T. S. Bjørheim and T. Uda, Yttrium-Doped Barium Zirconate-Cerate Solid Solution as Proton Conducting Electrolyte: Why Higher Cerium Concentration Leads to Better Performance for Fuel Cells and Electrolysis Cells, *Adv. Energy Mater.*, 2021, **11**, 2003149.

74 X. Qi and Y. Lin, Electrical Conducting Properties of Proton-Conducting Terbium-Doped Strontium Cerate Membrane, *Solid State Ionics*, 1999, **120**, 85–93.

75 T. Kobayashi, K. Abe, Y. Ukyo and H. Matsumoto, Study on Current Efficiency of Steam Electrolysis Using a Partial Protonic Conductor $SrZr_{0.9}Yb_{0.1}O_{3-\alpha}$, *Solid State Ionics*, 2001, **138**, 243–251.

76 L. Bi, S. P. Shafi and E. Traversa, Y-Doped $BaZrO_3$ as a Chemically Stable Electrolyte for Proton-Conducting Solid Oxide Electrolysis Cells (Soecs), *J. Mater. Chem. A*, 2015, **3**, 5815–5819.

77 H. Matsumoto, T. Sakai and Y. Okuyama, Proton-Conducting Oxide and Applications to Hydrogen Energy Devices, *Pure Appl. Chem.*, 2012, **85**, 427–435.

78 D. Huang, Y. Han, F. Wu and H. Wang, Intermediate Temperature Electrochemical Properties of Lutetium-Doped $SrCeO_3$/$SrZrO_3$-Molten Carbonate Composite Electrolyte, *Ceram. Int.*, 2019, **45**, 10149–10153.

79 J. Tong, D. Clark, M. Hoban and R. O'Hayre, Cost-Effective Solid-State Reactive Sintering Method for High Conductivity Proton Conducting Yttrium-Doped Barium Zirconium Ceramics, *Solid State Ionics*, 2010, **181**, 496–503.

80 D. Han, K. Shinoda, S. Tsukimoto, H. Takeuchi, C. Hiraiwa, M. Majima and T. Uda, Origins of Structural and Electrochemical Influence on Y-Doped $BaZrO_3$ Heat-Treated with Nio Additive, *J. Mater. Chem. A*, 2014, **2**, 12552–12560.

81 J. Cao, Y. Ji and Z. Shao, Perovskites for Protonic Ceramic Fuel Cells: A Review, *Energy Environ. Sci.*, 2022, **15**, 2200–2232.

82 X. Xu and L. Bi, Proton-Conducting Electrolyte Materials, *Intermediate Temperature Solid Oxide Fuel Cells*, Elsevier, 2020, pp. 81–111.

83 Z. Luo, Y. Zhou, X. Hu, N. Kane, T. Li, W. Zhang, Z. Liu, Y. Ding, Y. Liu and M. Liu, Critical Role of Acceptor Dopants in Designing Highly Stable and Compatible Proton-Conducting Electrolytes for Reversible Solid Oxide Cells, *Energy Environ. Sci.*, 2022, **15**, 2992–3003.

84 A. K. Andersson, S. M. Selbach, C. S. Knee and T. Grande, Chemical Expansion Due to Hydration of Proton-Conducting Perovskite Oxide Ceramics, *J. Am. Ceram. Soc.*, 2014, **97**, 2654–2661.

85 H. Matsumoto, Y. Kawasaki, N. Ito, M. Enoki and T. Ishihara, Relation between Electrical Conductivity and Chemical Stability of $BaCeO_3$-Based Proton Conductors with Different Trivalent Dopants, *Electrochem. Solid-State Lett.*, 2007, **10**, B77.

86 E. D. Wachsman and K. T. Lee, Lowering the Temperature of Solid Oxide Fuel Cells, *Science*, 2011, **334**, 935–939.

87 M. Asadikiya, H. Sabarou, M. Chen and Y. Zhong, Phase Diagram for a Nano-Yttria-Stabilized Zirconia System, *RSC Adv.*, 2016, **6**, 17438–17445.
88 S. Lamnini, D. Pugliese and F. Baino, Zirconia-Based Ceramics Reinforced by Carbon Nanotubes: A Review with Emphasis on Mechanical Properties, *Ceramics*, 2023, **6**, 1705–1734.
89 A. O. Zhigachev, V. V. Rodaev, D. V. Zhigacheva, N. V. Lyskov and M. A. Shchukina, Doping of Scandia-Stabilized Zirconia Electrolytes for Intermediate-Temperature Solid Oxide Fuel Cell: A Review, *Ceram. Int.*, 2021, **47**, 32490–32504.
90 K.-J. Hwang, M. Shin, M.-H. Lee, H. Lee, M. Y. Oh and T. H. Shin, Investigation on the Phase Stability of Yttria-Stabilized Zirconia Electrolytes for High-Temperature Electrochemical Application, *Ceram. Int.*, 2019, **45**, 9462–9467.
91 O. Yamamoto, Y. Arachi, H. Sakai, Y. Takeda, N. Imanishi, Y. Mizutani, M. Kawai and Y. Nakamura, Zirconia Based Oxide Ion Conductors for Solid Oxide Fuel Cells, *Ionics*, 1998, **4**, 403–408.
92 D. Lee, I. Lee, Y. Jeon and R. Song, Characterization of Scandia Stabilized Zirconia Prepared by Glycine Nitrate Process and Its Performance as the Electrolyte for IT-SOFC, *Solid State Ionics*, 2005, **176**, 1021–1025.
93 S. Badwal, F. Ciacchi and D. Milosevic, Scandia–Zirconia Electrolytes for Intermediate Temperature Solid Oxide Fuel Cell Operation, *Solid State Ionics*, 2000, **136**, 91–99.
94 S. J. Skinner, Recent Advances in the Understanding of the Evolution of Surfaces and Interfaces in Solid Oxide Cells, *Adv. Mater. Interfaces*, 2019, **6**, 1900580.
95 B. A. Horri, C. Selomulya and H. Wang, Electrochemical Characteristics and Performance of Anode-Supported SOFCs Fabricated Using Carbon Microspheres as a Pore-Former, *Int. J. Hydrogen Energy*, 2012, **37**, 19045–19054.
96 Z. Zakaria and S. K. Kamarudin, Advanced Modification of Scandia-Stabilized Zirconia Electrolytes for Solid Oxide Fuel Cells Application—a Review, *Int. J. Energy Res.*, 2021, **45**, 4871–4887.
97 O. Yamamoto, Y. Arati, Y. Takeda, N. Imanishi, Y. Mizutani, M. Kawai and Y. Nakamura, Electrical Conductivity of Stabilized Zirconia with Ytterbia and Scandia, *Solid State Ionics*, 1995, **79**, 137–142.
98 C. Ng, S. Ramesh, C. Tan, A. Muchtar and M. R. Somalu, Microwave Sintering of Ceria-Doped Scandia Stabilized Zirconia as Electrolyte for Solid Oxide Fuel Cell, *Int. J. Hydrogen Energy*, 2016, **41**, 14184–14190.
99 Y. Arachi, T. Asai, O. Yamamoto, Y. Takeda, N. Imanishi, K. Kawate and C. Tamakoshi, Electrical Conductivity of $ZrO_2$–$Sc_2O_3$ Doped with $HfO_2$, $CeO_2$, and $Ga_2O_3$, *J. Electrochem. Soc.*, 2001, **148**, A520–A523.
100 Q. Xue, X. Huang, L. Wang, H. Zhang and J. Zhang, Computational and Experimental Investigations of Defect Interaction and Ionic Conductivity in Doped Zirconia, *Phys. Rev. Appl.*, 2018, **10**, 014032.
101 M. Hirano, T. Oda, K. Ukai and Y. Mizutani, Suppression of Rhombohedral-Phase Appearance and Low-Temperature Sintering of Scandia-Doped Cubic-Zirconia, *J. Am. Ceram. Soc.*, 2002, **85**, 1336–1338.
102 C. Haering, A. Roosen, H. Schichl and M. Schnöller, Degradation of the Electrical Conductivity in Stabilised Zirconia System: Part II: Scandia-Stabilised Zirconia, *Solid State Ionics*, 2005, **176**, 261–268.
103 S. Omar, W. B. Najib and N. Bonanos, Conductivity Ageing Studies on 1M10ScSZ ($M^{4+}$ = Ce, Hf), *Solid State Ionics*, 2011, **189**, 100–106.
104 H. Shi, R. Ran and Z. Shao, Wet Powder Spraying Fabrication and Performance Optimization of IT-SOFCs with Thin-Film Scsz Electrolyte, *Int. J. Hydrogen Energy*, 2012, **37**, 1125–1132.
105 S. Oh, J. Park, J. W. Shin, B. C. Yang, J. Zhang, D. Y. Jang and J. An, High Performance Low-Temperature Solid Oxide Fuel Cells with Atomic Layer Deposited-Yttria Stabilized Zirconia Embedded Thin Film Electrolyte, *J. Mater. Chem. A*, 2018, **6**, 7401–7408.
106 I. Thaheem, K. J. Kim, J. J. Lee, D. W. Joh, I. Jeong and K. T. Lee, High Performance $Mn_{1.3}Co_{1.3}Cu_{0.4}O_4$ Spinel Based Composite Cathodes for Intermediate Temperature Solid Oxide Fuel Cells, *J. Mater. Chem. A*, 2019, **7**, 19696–19703.
107 A. Hussain, M. Z. Khan, R. H. Song, J.-E. Hong, S.-B. Lee and T.-H. Lim, High Performing and Durable Anode-Supported Solid Oxide Fuel Cell by Using Tape Casting, Lamination and Co-Firing Method, *ECS Trans.*, 2019, **91**, 373.
108 D. M. Alfeche and R. B. Cervera, Highly Conducting Sc and Y Co-Doped $ZrO_2$ Thin Film Solid Electrolyte on a Porous Ni/YSZ Electrode Prepared Via Simple Drop-Coating Method, *Ceram. Int.*, 2020, **46**, 10561–10567.
109 A. Sawka, Chemical Vapour Deposition of Scandia-Stabilised Zirconia Layers on Tubular Substrates at Low Temperatures, *Materials*, 2022, **15**, 2120.
110 Y.-P. Wang, J.-T. Gao, W. Chen, C.-X. Li, S.-L. Zhang, G.-J. Yang and C.-J. Li, Development of Scsz Electrolyte by Very Low Pressure Plasma Spraying for High-Performance Metal-Supported SOFCs, *J. Therm. Spray Technol.*, 2020, **29**, 223–231.
111 K. Yuan, C. Song, G. Chen, Z. Xu, H. Peng, X. Lu and X. Ji, Preparation of Dense ScSZ Thin Films by Plasma Spraying with Densified ScSZ Powders, *Int. J. Hydrogen Energy*, 2021, **46**, 9749–9757.
112 S. Jo, H. G. Jeong, Y. H. Kim, D. Neagu and J.-H. Myung, Stability and Activity Controls of Cu Nanoparticles for High-Performance Solid Oxide Fuel Cells, *Appl. Catal., B*, 2021, **285**, 119828.
113 H. Wang, Z. Lei, W. Jiang, X. Xu, J. Jing, Z. Zheng, Z. Yang and S. Peng, High-Conductivity Electrolyte with a Low Sintering Temperature for Solid Oxide Fuel Cells, *Int. J. Hydrogen Energy*, 2022, **47**, 11279–11287.
114 Z. Jiang, A. L. Snowdon, A. Siddiq, A. El-Kharouf and R. Steinberger-Wilckens, Optimization of a Sccesz/GDC Bi-Layer Electrolyte Fabrication Process for Intermediate Temperature Solid Oxide Fuel Cells, *Ceram. Int.*, 2022, **48**, 32844–32852.
115 E. Vøllestad, V. Øygarden, J. S. Graff, M. F. Sunding, J. D. Pietras, J. M. Polfus and M.-L. Fontaine, On the

Mechanism of Mn(II)-Doping in Scandia Stabilized Zirconia Electrolytes, *Acta Mater.*, 2022, **227**, 117695.

116 K. J. Kim, I. Thaheem, I. Jeong, H. Yu, J. H. Park and K. T. Lee, Nanostructured Spinel $Mn_{1.3}Co_{1.3}Cu_{0.4}O_4$ as a Bifunctional Electrocatalyst for High-Performance Solid Oxide Electrochemical Cells at Intermediate Temperatures, *J. Power Sources*, 2022, **539**, 231611.

117 K. Prabhakaran, M. Beigh, J. Lakra, N. Gokhale and S. Sharma, Characteristics of 8 mol% Yttria Stabilized Zirconia Powder Prepared by Spray Drying Process, *J. Mater. Process. Technol.*, 2007, **189**, 178–181.

118 Z. Gao, L. V. Mogni, E. C. Miller, J. G. Railsback and S. A. Barnett, A Perspective on Low-Temperature Solid Oxide Fuel Cells, *Energy Environ. Sci.*, 2016, **9**, 1602–1644.

119 A. J. Flegler, T. E. Burye, Q. Yang and J. D. Nicholas, Cubic Yttria Stabilized Zirconia Sintering Additive Impacts: A Comparative Study, *Ceram. Int.*, 2014, **40**, 16323–16335.

120 Y. Liu and L. Lao, Structural and Electrical Properties of Zno-Doped 8 mol% Yttria-Stabilized Zirconia, *Solid State Ionics*, 2006, **177**, 159–163.

121 J. Y. Koo, T. Mun, J. Lee, M. Choi, S. J. Kim and W. Lee, Enhancement of Oxygen Reduction Reaction Kinetics Using Infiltrated Yttria-Stabilized Zirconia Interlayers at the Electrolyte/Electrode Interfaces of Solid Oxide Fuel Cells, *J. Power Sources*, 2020, **472**, 228606.

122 J. Li, L. Fan, N. Hou, Y. Zhao and Y. Li, Solid Oxide Fuel Cell with a Spin-Coated Yttria Stabilized Zirconia/Gadolinia Doped Ceria Bi-Layer Electrolyte, *RSC Adv.*, 2022, **12**, 13220–13227.

123 S. Z. Golkhatmi, M. I. Asghar and P. D. Lund, A Review on Solid Oxide Fuel Cell Durability: Latest Progress, Mechanisms, and Study Tools, *Renewable Sustainable Energy Rev.*, 2022, **161**, 112339.

124 I. Jang, S. Kim, C. Kim, H. Lee, H. Yoon, T. Song and U. Paik, Interface Engineering of Yttrium Stabilized Zirconia/Gadolinium Doped Ceria Bi-Layer Electrolyte Solid Oxide Fuel Cell for Boosting Electrochemical Performance, *J. Power Sources*, 2019, **435**, 226776.

125 L. Wei, J. Zhang, F. Yu, W. Zhang, X. Meng, N. Yang, S. Liu and A. Novel, Fabrication of Yttria-Stabilized-Zirconia Dense Electrolyte for Solid Oxide Fuel Cells by 3D Printing Technique, *Int. J. Hydrogen Energy*, 2019, **44**, 6182–6191.

126 H. Mohebbi and S. Mirkazemi, Controlling Yttria-Stabilized Zirconia/Gadolinia-Doped Ceria Interdiffusion Layer in the Solid Oxide Fuel Cell Electrolyte Via Flash Sintering Method, *Ionics*, 2021, **27**, 5219–5227.

127 J. Kim, J. Kim, K. J. Yoon, J.-W. Son, J.-H. Lee, J.-H. Lee, H.-W. Lee and H.-I. Ji, Solid Oxide Fuel Cells with Zirconia/Ceria Bilayer Electrolytes Via Roll Calendering Process, *J. Alloys Compd.*, 2020, **846**, 156318.

128 K. Jia, L. Zheng, W. Liu, J. Zhang, F. Yu, X. Meng, C. Li, J. Sunarso, N. Yang and A. New, and Simple Way to Prepare Monolithic Solid Oxide Fuel Cell Stack by Stereolithography 3D Printing Technology Using 8 mol% Yttria Stabilized Zirconia Photocurable Slurry, *J. Eur. Ceram. Soc.*, 2022, **42**, 4275–4285.

129 Y. Lim, J. Park, H. Lee, M. Ku and Y.-B. Kim, Rapid Fabrication of Lanthanum Strontium Cobalt Ferrite (LSCF) with Suppression of LSCF/YSZ Chemical Side Reaction Via Flash Light Sintering for SOFCs, *Nano Energy*, 2021, **90**, 106524.

130 J. H. Park, S. M. Han, B.-K. Kim, J.-H. Lee, K. J. Yoon, H. Kim, H.-I. Ji and J.-W. Son, Sintered Powder-Base Cathode over Vacuum-Deposited Thin-Film Electrolyte of Low-Temperature Solid Oxide Fuel Cell: Performance and Stability, *Electrochim. Acta*, 2019, **296**, 1055–1063.

131 O. S. Jeon, M. G. Park, R. H. Song, K. H. Ryu, C. W. Na, Y. G. Shul and J. G. Lee, Effects of $Fe_2O_3$ Doping on Structural and Electrical Properties of 8 mol% Yttria-Stabilized Zirconia Electrolyte for Solid Oxide Fuel Cells, *J. Mater. Sci.: Mater. Electron.*, 2022, **33**, 3208–3214.

132 C. Kim, S. Kim, I. Jang, H. Yoon, T. Song and U. Paik, Facile Fabrication Strategy of Highly Dense Gadolinium-Doped Ceria/Yttria-Stabilized Zirconia Bilayer Electrolyte Via Cold Isostatic Pressing for Low Temperature Solid Oxide Fuel Cells, *J. Power Sources*, 2019, **415**, 112–118.

133 S. Basu, M. N. Alam, S. Basu and H. S. Maiti, 8YSZ–Carbonate Composite Electrolyte-Conductivity Enhancement, *J. Alloys Compd.*, 2020, **816**, 152561.

134 Y. Lim, H. Lee, J. Park and Y.-B. Kim, Low-Temperature Constrained Sintering of YSZ Electrolyte with $Bi_2O_3$ Sintering Sacrificial Layer for Anode-Supported Solid Oxide Fuel Cells, *Ceram. Int.*, 2022, **48**, 9673–9680.

135 S. Masciandaro, M. Torrell, P. Leone and A. Tarancón, Three-Dimensional Printed Yttria-Stabilized Zirconia Self-Supported Electrolytes for Solid Oxide Fuel Cell Applications, *J. Eur. Ceram. Soc.*, 2019, **39**, 9–16.

136 Y.-Z. Xing, Y.-N. Men, X. Feng, J.-H. Geng, Z.-R. Zou and F.-H. Chen, Evolutions in the Microstructure and Ionic Conductivity of Cuo-Doped Yttria-Stabilized Zirconia, *J. Solid State Chem.*, 2022, **315**, 123497.

137 B. Xing, C. Cao, W. Zhao, M. Shen, C. Wang and Z. Zhao, Dense 8 mol% Yttria-Stabilized Zirconia Electrolyte by Dlp Stereolithography, *J. Eur. Ceram. Soc.*, 2020, **40**, 1418–1423.

138 G. Y. Cho, Y. H. Lee, W. Yu, J. An and S. W. Cha, Optimization of $Y_2O_3$ Dopant Concentration of Yttria Stabilized Zirconia Thin Film Electrolyte Prepared by Plasma Enhanced Atomic Layer Deposition for High Performance Thin Film Solid Oxide Fuel Cells, *Energy*, 2019, **173**, 436–442.

139 M. Mogensen, T. Lindegaard, U. R. Hansen and G. Mogensen, Physical Properties of Mixed Conductor Solid Oxide Fuel Cell Anodes of Doped $CeO_2$, *J. Electrochem. Soc.*, 1994, **141**, 2122.

140 A. J. Araújo, J. P. Grilo, F. J. Loureiro, L. I. Holz, D. A. Macedo, D. P. Fagg and C. A. Paskocimas, Proteic Sol–Gel Synthesis of Gd-Doped Ceria: A Comprehensive Structural, Chemical, Microstructural and Electrical Analysis, *J. Mater. Sci.*, 2020, **55**, 16864–16878.

141 H. T. Handal and V. Thangadurai, Evaluation of Chemical Stability, Thermal Expansion Coefficient, and Electrical Properties of Solid State and Wet-Chemical Synthesized Y

and Mn-Codoped $CeO_2$ for Solid Oxide Fuel Cells, *J. Power Sources*, 2013, **243**, 458–471.

142 K. Sandhya, N. Chitra Priya, D. N. Rajendran and P. Thappily, Structural and Electrical Properties of Cerium Oxides Doped by $Sb^{3+}$ and $Bi^{3+}$ Cations, *J. Electron. Mater.*, 2020, **49**, 4936–4944.

143 A. Kalpana Devi, G. Ram Kumar, C. Prerna, K. Amarsingh Bhabu, V. Sabarinathan and T. R. Rajasekaran, Superionic Conductive $La^{3+}$ and $Pr^{3+}$ Co-Doped Cerium Oxide for IT-SOFC Applications, *J. Mater. Sci.: Mater. Electron.*, 2020, **31**, 10628–10638.

144 D. Puente-Martínez, J. Díaz-Guillén, S. Montemayor, J. Díaz-Guillén, O. Burciaga-Díaz, M. Bazaldúa-Medellín, M. Díaz-Guillén and A. Fuentes, High Ionic Conductivity in $CeO_2$ SOFC Solid Electrolytes; Effect of Dy Doping on Their Electrical Properties, *Int. J. Hydrogen Energy*, 2020, **45**, 14062–14070.

145 R. N. Bharathi and S. Sankar, Investigation of Transport Properties of Pr Doped Cerium Oxide Nanoparticles as a Solid Electrolyte for IT-SOFC Applications, *J. Inorg. Organomet. Polym. Mater.*, 2018, **28**, 1829–1838.

146 K. Amarsingh Bhabu, J. Theerthagiri, J. Madhavan, T. Balu, G. Muralidharan and T. Rajasekaran, Cubic Fluorite Phase of Samarium Doped Cerium Oxide ($CeO_2$) 0.96Sm 0.04 for Solid Oxide Fuel Cell Electrolyte, *J. Mater. Sci.: Mater. Electron.*, 2016, **27**, 1566–1573.

147 H. Inaba and H. Tagawa, Ceria-Based Solid Electrolytes, *Solid State Ionics*, 1996, **83**, 1–16.

148 D. J. Kim, Lattice Parameters, Ionic Conductivities, and Solubility Limits in Fluorite-Structure $Mo_2$ Oxide [M = $Hf^{4+}$, $Zr^{4+}$, $Ce^{4+}$, $Th^{4+}$, $U^{4+}$] Solid Solutions, *J. Am. Ceram. Soc.*, 1989, **72**, 1415–1421.

149 A. Arabaci, Ceria-Based Solid Electrolytes for IT-SOFC Applications, *Acta Phys. Pol., A*, 2020, **137**, 530–534.

150 M. Chen, B. H. Kim, Q. Xu, B. K. Ahn, W. J. Kang and D. Ping Huang, Synthesis and Electrical Properties of $Ce_{0.8}Sm_{0.2}O_{1.9}$ Ceramics for IT-SOFC Electrolytes by Urea-Combustion Technique, *Ceram. Int.*, 2009, **35**, 1335–1343.

151 H.-C. Yao, Y.-X. Zhang, J.-J. Liu, Y.-L. Li, J.-S. Wang and Z.-J. Li, Synthesis and Characterization of $Gd^{3+}$ and $Nd^{3+}$ Co-Doped Ceria by Using Citric Acid–Nitrate Combustion Method, *Mater. Res. Bull.*, 2011, **46**, 75–80.

152 S. Banerjee, P. S. Devi, D. Topwal, S. Mandal and K. Menon, Enhanced Ionic Conductivity in $Ce_{0.8}Sm_{0.2}O_{1.9}$: Unique Effect of Calcium Co-Doping, *Adv. Funct. Mater.*, 2007, **17**, 2847–2854.

153 M. C. Martin and M. L. Mecartney, Grain Boundary Ionic Conductivity of Yttrium Stabilized Zirconia as a Function of Silica Content and Grain Size, *Solid State Ionics*, 2003, **161**, 67–79.

154 X. Guo and R. Waser, Electrical Properties of the Grain Boundaries of Oxygen Ion Conductors: Acceptor-Doped Zirconia and Ceria, *Prog. Mater. Sci.*, 2006, **51**, 151–210.

155 C. Tian and S.-W. Chan, Ionic Conductivities, Sintering Temperatures and Microstructures of Bulk Ceramic $CeO_2$ Doped with $Y_2O_3$, *Solid State Ionics*, 2000, **134**, 89–102.

156 H. Yoshida and T. Inagaki, Effects of Additives on the Sintering Properties of Samaria-Doped Ceria, *J. Alloys Compd.*, 2006, **408**, 632–636.

157 E. Jud, C. B. Huwiler and L. J. Gauckler, Sintering Analysis of Undoped and Cobalt Oxide Doped Ceria Solid Solutions, *J. Am. Ceram. Soc.*, 2005, **88**, 3013–3019.

158 T. Zhang, P. Hing, H. Huang and J. Kilner, Sintering and Grain Growth of Coo-Doped $CeO_2$ Ceramics, *J. Eur. Ceram. Soc.*, 2002, **22**, 27–34.

159 Y. Dong, S. Hampshire, B. Lin, Y. Ling and X. Zhang, High Sintering Activity Cu–Gd Co-Doped $CeO_2$ Electrolyte for Solid Oxide Fuel Cells, *J. Power Sources*, 2010, **195**, 6510–6515.

160 T. Zhang, J. Ma, Y. Leng, S. Chan, P. Hing and J. Kilner, Effect of Transition Metal Oxides on Densification and Electrical Properties of Si-Containing $Ce_{0.8}Gd_{0.2}O_{2-\Delta}$ Ceramics, *Solid State Ionics*, 2004, **168**, 187–195.

161 E. Jud, Z. Zhang, W. Sigle and L. J. Gauckler, Microstructure of Cobalt Oxide Doped Sintered Ceria Solid Solutions, *J. Electroceram.*, 2006, **16**, 191–197.

162 S. Omar and J. C. Nino, Consistency in the Chemical Expansion of Fluorites: A Thermal Revision of the Doped Ceria, *Acta Mater.*, 2013, **61**, 5406–5413.

163 K. Sato, T. Hashida, K. Yashiro, H. Yugami, T. Kawada and J. Mizusaki, Mechanical Damage Evaluation of Solid Oxide Fuel Cells under Simulated Operating Conditions, *J. Ceram. Soc. Jpn.*, 2005, **113**, 562–564.

164 J. Wright and A. V. Virkar, Conductivity of Porous $Sm_2O_3$-Doped $CeO_2$ as a Function of Temperature and Oxygen Partial Pressure, *J. Power Sources*, 2011, **196**, 6118–6124.

165 S. Sanna, V. Esposito, J. W. Andreasen, J. Hjelm, W. Zhang, T. Kasama, S. B. Simonsen, M. Christensen, S. Linderoth and N. Pryds, Enhancement of the Chemical Stability in Confined $\Delta$-$Bi_2O_3$, *Nat. Mater.*, 2015, **14**, 500–504.

166 H. Ozlu, S. Cakar, C. Bilir, E. Ersoy and O. Turkoglu, Synthesis and Characterization of $\Gamma$-$Bi_2O_3$ Based Solid Electrolyte Doped with $Nb_2O_5$, *Bull. Mater. Sci.*, 2014, **37**, 843–848.

167 V. Kharton, F. Marques and A. Atkinson, Transport Properties of Solid Oxide Electrolyte Ceramics: A Brief Review, *Solid State Ionics*, 2004, **174**, 135–149.

168 R. Chen, S.-L. Zhang, C.-J. Li and C.-X. Li, Plasma-Sprayed High-Performance $(Bi_2O_3)_{0.75}(Y_2O_3)_{0.25}$ Electrolyte for Intermediate-Temperature Solid Oxide Fuel Cells (IT-SOFCs), *J. Therm. Spray Technol.*, 2021, **30**, 196–204.

169 H. Ozlu Torun, S. Cakar, E. Ersoy and O. Turkoglu, The Bulk Electrical Conductivity Properties of $\Delta$-$Bi_2O_3$ Solid Electrolyte System Doped with $Yb_2O_3$, *J. Therm. Anal. Calorim.*, 2015, **122**, 525–536.

170 M. Abdullah, H. Chawla, H. B. Albargi, J. S. Algethami, M. Z. Ahmad, A. Chandra and S. Garg, Bismuth-Based Nanophotocatalysts for Environmental Reintegration, *Inorg. Chem. Commun.*, 2023, 111016.

171 N. Jiang, R. Buchanan, F. Henn, A. Marshall, D. Stevenson and E. Wachsman, Aging Phenomenon of Stabilized Bismuth Oxides, *Mater. Res. Bull.*, 1994, **29**, 247–254.

172 N. Jiang, E. D. Wachsman and S.-H. Jung, A Higher Conductivity $Bi_2O_3$-Based Electrolyte, *Solid State Ionics*, 2002, **150**, 347–353.
173 A. Yaremchenko, V. Kharton, E. Naumovich and A. Tonoyan, Stability of Δ-$Bi_2O_3$-Based Solid Electrolytes, *Mater. Res. Bull.*, 2000, **35**, 515–520.
174 B.-H. Yun, C.-W. Lee, I. Jeong and K. T. Lee, Dramatic Enhancement of Long-Term Stability of Erbia-Stabilized Bismuth Oxides Via Quadrivalent Hf Doping, *Chem. Mater.*, 2017, **29**, 10289–10293.
175 A. Watanabe and M. Sekita, Stabilized Δ-$Bi_2O_3$ Phase in the System $Bi_2O_3$–$Er_2O_3$–$Wo_3$ and Its Oxide-Ion Conduction, *Solid State Ionics*, 2005, **176**, 2429–2433.
176 Y. Gao, M. Zhong, J. Chen, S. Wang, B. Zhang, Q. Li, W. Liu, J.-T. Gao, C.-X. Li and C.-J. Li, Stabilities and Performance of Single Cubic Phase Dysprosium and Zirconium Co-Doped Bismuth Oxide Electrolytes for Low Temperature Solid Oxide Fuel Cells, *Mater. Adv.*, 2023, **4**, 2839–2852.
177 H. Yu, I. Jeong, S. Jang, D. Kim, H. N. Im, C. W. Lee, E. D. Wachsman and K. T. Lee, Lowering the Temperature of Solid Oxide Electrochemical Cells Using Triple-Doped Bismuth Oxides, *Adv. Mater.*, 2024, **36**, 2306205.
178 I. Abrahams and F. Krok, A Model for the Mechanism of Low Temperature Ionic Conduction in Divalent-Substituted Γ-Bimevoxes, *Solid State Ionics*, 2003, **157**, 139–145.
179 A. Watanabe and K. Das, Time-Dependent Degradation Due to the Gradual Phase Change in Bicuvox and Bicovox Oxide-Ion Conductors at Temperatures Below About 500 °C, *J. Solid State Chem.*, 2002, **163**, 224–230.
180 E. Pernot, M. Anne, M. Bacmann, P. Strobel, J. Fouletier, R. Vannier, G. Mairesse, F. Abraham and G. Nowogrocki, Structure and Conductivity of Cu and Ni-Substituted $Bi_4V_2O_{11}$ Compounds, *Solid State Ionics*, 1994, **70**, 259–263.
181 R. Rusli, I. Abrahams, A. Patah and B. Prijamboedi, Ismunandar, *Ionic Conductivity of* $Bi_2Ni_xV_{1-x}O_{5.5-3x/2}$ $(0.1 \leq x \leq 0.2)$ Oxides Prepared by a Low Temperature Sol–Gel Route, AIP Conference Proceedings, American Institute of Physics, 2014, pp. 178–181.
182 E. Wachsman, P. Jayaweera, N. Jiang, D. Lowe and B. Pound, Stable High Conductivity Ceria/Bismuth Oxide Bilayered Electrolytes, *J. Electrochem. Soc.*, 1997, **144**, 233.
183 B. S. Prakash, R. Pavitra, S. S. Kumar and S. Aruna, Electrolyte Bi-Layering Strategy to Improve the Performance of an Intermediate Temperature Solid Oxide Fuel Cell: A Review, *J. Power Sources*, 2018, **381**, 136–155.
184 M. Cherry, M. S. Islam and C. Catlow, Oxygen Ion Migration in Perovskite-Type Oxides, *J. Solid State Chem.*, 1995, **118**, 125–132.
185 T. Ishihara, Low Temperature Solid Oxide Fuel Cells Using $LaGaO_3$-Based Oxide Electrolyte on Metal Support, *J. Jpn. Pet. Inst.*, 2015, **58**, 71–78.
186 P. Majewski, M. Rozumek and F. Aldinger, Phase Diagram Studies in the Systems $La_2O_3$–SrO–MgO–$Ga_2O_3$ at 1350–1400 °C in Air with Emphasis on Sr and Mg Substituted $LaGaO_3$, *J. Alloys Compd.*, 2001, **329**, 253–258.
187 R. Pelosato, C. Cristiani, G. Dotelli, S. Latorrata, R. Ruffo and L. Zampori, Co-Precipitation in Aqueous Medium of $La_{0.8}Sr_{0.2}Ga_{0.8}Mg_{0.2}O_{3-\Delta}$ Via Inorganic Precursors, *J. Power Sources*, 2010, **195**, 8116–8123.
188 J. B. Goodenough, Oxide-Ion Electrolytes, *Annu. Rev. Mater. Res.*, 2003, **33**, 91–128.
189 T. Ishihara, *Perovskite Oxide for Solid Oxide Fuel Cells*, Springer Science & Business Media, 2009.
190 K. Huang, J. B. Goodenough and A. Solid Oxide Fuel Cell Based, on Sr-and Mg-Doped $LaGaO_3$ Electrolyte: The Role of a Rare-Earth Oxide Buffer, *J. Alloys Compd.*, 2000, **303**, 454–464.
191 J. W. Fergus, Electrolytes for Solid Oxide Fuel Cells, *J. Power Sources*, 2006, **162**, 30–40.
192 O. N. Verma, S. Singh, V. K. Singh, M. Najim, R. Pandey and P. Singh, Influence of Ba Doping on the Electrical Behaviour of $La_{0.9}Sr_{0.1}Al_{0.9}Mg_{0.1}O_{3-\Delta}$ System for a Solid Electrolyte, *J. Electron. Mater.*, 2021, **50**, 1010–1021.
193 T. L. Nguyen, M. Dokiya, S. Wang, H. Tagawa and T. Hashimoto, The Effect of Oxygen Vacancy on the Oxide Ion Mobility in $LaAlO_3$-Based Oxides, *Solid State Ionics*, 2000, **130**, 229–241.
194 Q. Fu, F. Tietz, P. Lersch and D. Stöver, Evaluation of Sr- and Mn-Substituted $LaAlO_3$ as Potential SOFC Anode Materials, *Solid State Ionics*, 2006, **177**, 1059–1069.
195 P. Lacorre, The Lps Concept, a New Way to Look at Anionic Conductors, *Solid State Sci.*, 2000, **2**, 755–758.
196 F. Goutenoire, O. Isnard, R. Retoux and P. Lacorre, Crystal Structure of $La_2Mo_2O_9$, a New Fast Oxide-Ion Conductor, *Chem. Mater.*, 2000, **12**, 2575–2580.
197 R. Pandey, S. Singh and P. Singh, Modified Polyol-Mediated Synthesis of Sr-and W-Substituted $La_2Mo_2O_9$ Solid Electrolyte for Solid Oxide Fuel Cells, *J. Mater. Sci.: Mater. Electron.*, 2020, **31**, 11325–11335.
198 T.-Y. Jin, M. M. Rao, C.-L. Cheng, D.-S. Tsai and M.-H. Hung, Structural Stability and Ion Conductivity of the Dy and W Substituted $La_2Mo_2O_9$, *Solid State Ionics*, 2007, **178**, 367–374.
199 D. Marrero-López, J. Peña-Martínez, J. Ruiz-Morales, D. Pérez-Coll, M. Martín-Sedeño and P. Núñez, Applicability of $La_2Mo_{2-y}W_yO_9$ Materials as Solid Electrolyte for SOFCs, *Solid State Ionics*, 2007, **178**, 1366–1378.
200 H.-C. Chang, D.-S. Tsai, W.-H. Chung, Y.-S. Huang, M.-V. Le and A. Ceria Layer, as Diffusion Barrier between Lamox and Lanthanum Strontium Cobalt Ferrite Along with the Impedance Analysis, *Solid State Ionics*, 2009, **180**, 412–417.
201 H. Yoshioka and S. Tanase, Magnesium Doped Lanthanum Silicate with Apatite-Type Structure as an Electrolyte for Intermediate Temperature Solid Oxide Fuel Cells, *Solid State Ionics*, 2005, **176**, 2395–2398.
202 J. R. Tolchard, M. S. Islam and P. R. Slater, Defect Chemistry and Oxygen Ion Migration in the Apatite-Type Materials $La_{9.33}Si_6O_{26}$ and $La_8Sr_2Si_6O_{26}$, *J. Mater. Chem.*, 2003, **13**, 1956–1961.
203 A. Najib, J. Sansom, J. Tolchard, P. Slater and M. Islam, Doping Strategies to Optimise the Oxide Ion Conductivity in Apatite-Type Ionic Conductors, *Dalton Trans.*, 2004, 3106–3109.

204 S. Tao and J. T. Irvine, Preparation and Characterisation of Apatite-Type Lanthanum Silicates by a Sol–Gel Process, *Mater. Res. Bull.*, 2001, **36**, 1245–1258.

205 E. Abram, D. Sinclair and A. West, A Novel Enhancement of Ionic Conductivity in the Cation-Deficient Apatite $La_{9.33}(SiO_4)_6O_2$, *J. Mater. Chem.*, 2001, **11**, 1978–1979.

206 J. Xiang, Z.-G. Liu, J.-H. Ouyang and F.-Y. Yan, Synthesis, Structure and Electrical Properties of Rare-Earth Doped Apatite-Type Lanthanum Silicates, *Electrochim. Acta*, 2012, **65**, 251–256.

207 J. Li, Q. Cai and B. Amini Horri, Synthesis and Densification of Mo/Mg Co-Doped Apatite-Type Lanthanum Silicate Electrolyte with Enhanced Ionic Conductivity, *Chem. – Eur. J.*, 2023, **29**, e202300021.

208 J. Li, Q. Cai and B. A. Horri, Synthesis and Densification of Mo/Mg Co-Doped Apatite-Type Lanthanum Silicate Electrolytes with Enhanced Ionic Conductivity, *Chem. – Eur. J.*, 2023, e202300021.

209 A. Noviyanti, D. Eddy, F. Lastiyanti, I. Rahayu, D. Syarif and T. Saragi, *Synthesis and Conductivities of the Ti-Doped Apatite-Type Phases* $La_{9.33}Si_{6-x}Ti_xO_{26}$, Journal of Physics: Conference Series, IOP Publishing, 2018, p. 012018.

210 A. R. Noviyanti, S. Winarsih, D. G. Syarif, Y. T. Malik and R. Septawendar, Highly Enhanced Electrical Properties of Lanthanum-Silicate-Oxide-Based SOFC Electrolytes with Co-Doped Tin and Bismuth in $La_{9.33-x}Bi_xSi_{6-Y}Sn_yO_{26}$, *RSC Adv.*, 2021, **11**, 38589–38595.

211 L. Dai, W. Han, Y. Li and L. Wang, Synthesis and Characterization of $Al^{3+}$ and M (M = $W^{6+}$, $In^{3+}$, $Nb^{5+}$, $Mg^{2+}$) Co-Doped Lanthanum Silicate Oxy-Apatite Electrolytes, *Int. J. Hydrogen Energy*, 2016, **41**, 11340–11350.

212 D. Marrero-López, M. Martín-Sedeño, J. Peña-Martínez, J. Ruiz-Morales, P. Núñez, M. Aranda and J. Ramos-Barrado, Evaluation of Apatite Silicates as Solid Oxide Fuel Cell Electrolytes, *J. Power Sources*, 2010, **195**, 2496–2506.

213 X. Wang, Y. Ma, S. Li, A.-H. Kashyout, B. Zhu and M. Muhammed, Ceria-Based Nanocomposite with Simultaneous Proton and Oxygen Ion Conductivity for Low-Temperature Solid Oxide Fuel Cells, *J. Power Sources*, 2011, **196**, 2754–2758.

214 P. Ranran, W. Yan, Y. Lizhai and M. Zongqiang, Electrochemical Properties of Intermediate-Temperature SOFCs Based on Proton Conducting Sm-Doped $BaCeO_3$ Electrolyte Thin Film, *Solid State Ionics*, 2006, **177**, 389–393.

215 C. Zhou, J. Sunarso, Y. Song, J. Dai, J. Zhang, B. Gu, W. Zhou and Z. Shao, New Reduced-Temperature Ceramic Fuel Cells with Dual-Ion Conducting Electrolyte and Triple-Conducting Double Perovskite Cathode, *J. Mater. Chem. A*, 2019, **7**, 13265–13274.

216 J. Cao, C. Su, Y. Ji, G. Yang and Z. Shao, Recent Advances and Perspectives of Fluorite and Perovskite-Based Dual-Ion Conducting Solid Oxide Fuel Cells, *J. Energy Chem.*, 2021, **57**, 406–427.

217 K.-Y. Park, T.-H. Lee, S. Jo, J. Yang, S.-J. Song, H.-T. Lim, J. H. Kim and J.-Y. Park, Electrical and Physical Properties of Composite $BaZr_{0.85}Y_{0.15}O_{3-\Delta}$-$Nd_{0.1}Ce_{0.9}O_{2-\delta}$ Electrolytes for Intermediate Temperature-Solid Oxide Fuel Cells, *J. Power Sources*, 2016, **336**, 437–446.

218 G. Huang, X. Huang, J. Cao, J. Zhu, Y. Liu, H. Xia, X. Deng, S. Shao and Y. Ji, Metal Ion Migration: A New Insight into the $H^+/O_2$–Dual-Ion Transport in Perovskite–Fluorite Composites, *ACS Appl. Energy Mater.*, 2022, **5**, 3647–3659.

219 J. Cao, Y. Ji, X. Zhou, C. Cao, X. He and W. Liu, An Investigation of Metal Ion Diffusion in Ceria-Based Solid Oxide Fuel Cell with Barium-Containing Anode, *J. Am. Ceram. Soc.*, 2018, **101**, 5791–5800.

220 B. Zhu, X. Liu, P. Zhou, X. Yang, Z. Zhu and W. Zhu, Innovative Solid Carbonate–Ceria Composite Electrolyte Fuel Cells, *Electrochem. Commun.*, 2001, **3**, 566–571.

221 X. Wang, Y. Ma, R. Raza, M. Muhammed and B. Zhu, Novel Core–Shell SDC/Amorphous $Na_2Co_3$ Nanocomposite Electrolyte for Low-Temperature SOFCs, *Electrochem. Commun.*, 2008, **10**, 1617–1620.

222 Y. Jing, P. Lund, M. I. Asghar, F. Li, B. Zhu, B. Wang, X. Zhou, C. Chen and L. Fan, Non-Doped $CeO_2$-Carbonate Nanocomposite Electrolyte for Low Temperature Solid Oxide Fuel Cells, *Ceram. Int.*, 2020, **46**, 29290–29296.

223 L. Fan, C. He and B. Zhu, Role of Carbonate Phase in Ceria–Carbonate Composite for Low Temperature Solid Oxide Fuel Cells: A Review, *Int. J. Energy Res.*, 2017, **41**, 465–481.

224 S. Celerier, C. Laberty-Robert, F. Ansart, C. Calmet and P. Stevens, Synthesis by Sol–Gel Route of Oxyapatite Powders for Dense Ceramics: Applications as Electrolytes for Solid Oxide Fuel Cells, *J. Eur. Ceram. Soc.*, 2005, **25**, 2665–2668.

225 R. Elilarassi and G. Chandrasekaran, Structural, Optical and Magnetic Characterization of Cu-Doped Zno Nanoparticles Synthesized Using Solid State Reaction Method, *J. Mater. Sci.: Mater. Electron.*, 2010, **21**, 1168–1173.

226 Y. Zhao, L. Dai, Z. He, L. Wang and J. Cao, Synthesis and Characterization of $Ba^{2+}$ and $W^{6+}$ Co-Doped Apatite-Type Lanthanum Silicate Electrolytes, *Ceram. Int.*, 2020, **46**, 5420–5429.

227 J. Xiang, H.-Q. Chen, J.-H. Ouyang, Z.-G. Liu, J.-Y. Yu, F.-F. Wu, R.-D. Zhao, J. Shang and L. Liu, Stability and Compatibility of Lanthanum Silicates Electrolyte with Standard Cathode Materials, *Ceram. Int.*, 2019, **45**, 6183–6189.

228 Z. Zhan, T.-L. Wen, H. Tu and Z.-Y. Lu, Ac Impedance Investigation of Samarium-Doped Ceria, *J. Electrochem. Soc.*, 2001, **148**, A427.

229 J. Tolchard and T. Grande, Chemical Compatibility of Candidate Oxide Cathodes for $BaZrO_3$ Electrolytes, *Solid State Ionics*, 2007, **178**, 593–599.

230 S. Feng and R. Xu, New Materials in Hydrothermal Synthesis, *Acc. Chem. Res.*, 2001, **34**, 239–247.

231 M. Rafique, H. Nawaz, M. Shahid Rafique, M. Bilal Tahir, G. Nabi and N. Khalid, Material and Method Selection for Efficient Solid Oxide Fuel Cell Anode: Recent Advancements and Reviews, *Int. J. Energy Res.*, 2019, **43**, 2423–2446.

232 P. Jena, P. K. Patro, A. Sinha, R. K. Lenka, A. K. Singh, T. Mahata and P. K. Sinha, Hydrothermal Synthesis and

Characterization of an Apatite-Type Lanthanum Silicate Ceramic for Solid Oxide Fuel Cell Electrolyte Applications. *Energy*, *Technology*, 2018, **6**, 1739–1746.

233 Y. Xu, N. Farandos, M. Rosa, P. Zielke, V. Esposito, P. Vang Hendriksen, S. H. Jensen, T. Li, G. Kelsall and R. Kiebach, Continuous Hydrothermal Flow Synthesis of Gd-Doped $CeO_2$ (GDC) Nanoparticles for Inkjet Printing of SOFC Electrolytes, *Int. J. Appl. Ceram. Technol.*, 2018, **15**, 315–327.

234 B. A. Fan, The Hydrothermal Synthesis of Nano-YSZ Crystallite and the Preparation of YSZ Electrolyte Film for SOFC, *Adv. Mater. Res.*, 2011, **228**, 288–292.

235 H. Shi, W. Zhou, R. Ran and Z. Shao, Comparative Study of Doped Ceria Thin-Film Electrolytes Prepared by Wet Powder Spraying with Powder Synthesized Via Two Techniques, *J. Power Sources*, 2010, **195**, 393–401.

236 Q. Lyu, T. Zhu, H. Qu, Z. Sun, K. Sun, Q. Zhong and M. Han, Lower Down Both Ohmic and Cathode Polarization Resistances of Solid Oxide Fuel Cell Via Hydrothermal Modified Gadolinia Doped Ceria Barrier Layer, *J. Eur. Ceram. Soc.*, 2021, **41**, 5931–5938.

237 Z. Zakaria, Z. Awang Mat, S. H. Abu Hassan and Y. Boon Kar, A Review of Solid Oxide Fuel Cell Component Fabrication Methods toward Lowering Temperature, *Int. J. Energy Res.*, 2020, **44**, 594–611.

238 B. Dunn, G. C. Farrington and B. Katz, Sol–Gel Approaches for Solid Electrolytes and Electrode Materials, *Solid State Ionics*, 1994, **70**, 3–10.

239 S. Célérier, C. Laberty-Robert, J. W. Long, K. A. Pettigrew, R. M. Stroud, D. R. Rolison, F. Ansart and P. Stevens, Synthesis of $La_{9.33}Si_6O_{26}$ Pore–Solid Nanoarchitectures Via Epoxide-Driven Sol–Gel Chemistry, *Adv. Mater.*, 2006, **18**, 615–618.

240 I. Sudzhanskaya, Y. S. Nekrasova and A. Gogolev, Manufacture, Structure and Electrophysical Properties of YSZ/$SrTi_xZr_{1-x}O_3$ Solid Solution, *Ceram. Int.*, 2020, **46**, 28120–28124.

241 D. H. Prasad, J.-W. Son, B.-K. Kim, H.-W. Lee and J.-H. Lee, Synthesis of Nano-Crystalline $Ce_{0.9}Gd_{0.1}O_{1.95}$ Electrolyte by Novel Sol–Gel Thermolysis Process for IT-SOFCs, *J. Eur. Ceram. Soc.*, 2008, **28**, 3107–3112.

242 W. Huang, P. Shuk and M. Greenblatt, Properties of Sol–Gel Prepared $Ce_{1-x}Sm_xO_{2-x/2}$ Solid Electrolytes, *Solid State Ionics*, 1997, **100**, 23–27.

243 S. M. Bhagyaraj, O. S. Oluwafemi, N. Kalarikkal and S. Thomas, *Synthesis of Inorganic Nanomaterials*, Woodhead publication, 2018, p. 1e18.

244 M. Choolaei, M. F. Vostakola and B. A. Horri, Recent Advances and Challenges in Thin-Film Fabrication Techniques for Low-Temperature Solid Oxide Fuel Cells, *Crystals*, 2023, **13**, 1008.

245 M. Kotobuki, B. Kobayashi, M. Koishi, T. Mizushima and N. Kakuta, Preparation of $Li_{1.5}Al_{0.5}Ti_{1.5}(Po_4)_3$ Solid Electrolyte Via Coprecipitation Using Various $Po_4$ Sources, *Mater. Technol.*, 2014, **29**, A93–A97.

246 N. Jongen, P. Bowen, J. Lemaître, J.-C. Valmalette and H. Hofmann, Precipitation of Self-Organized Copper Oxalate Polycrystalline Particles in the Presence of Hydroxypropylmethylcellulose (HPMC): Control of Morphology, *J. Colloid Interface Sci.*, 2000, **226**, 189–198.

247 A. Magyarosy, R. Laidlaw, R. Kilaas, C. Echer, D. Clark and J. Keasling, Nickel Accumulation and Nickel Oxalate Precipitation by Aspergillus Niger, *Appl. Microbiol. Biotechnol.*, 2002, **59**, 382–388.

248 J. Huang, Z. Mao, Z. Liu and C. Wang, Development of Novel Low-Temperature SOFCs with Co-Ionic Conducting SDC-Carbonate Composite Electrolytes, *Electrochem. Commun.*, 2007, **9**, 2601–2605.

249 S. Zha, C. Xia and G. Meng, Effect of Gd(Sm) Doping on Properties of Ceria Electrolyte for Solid Oxide Fuel Cells, *J. Power Sources*, 2003, **115**, 44–48.

250 J. G. Li, T. Ikegami, Y. Wang and T. Mori, 10-mol%-$Gd_2O_3$-Doped $CeO_2$ Solid Solutions Via Carbonate Coprecipitation: A Comparative Study, *J. Am. Ceram. Soc.*, 2003, **86**, 915–921.

251 Y. Ma, M. Moliere, Z. Yu, N. Fenineche and O. Elkedim, Novel Chemical Reaction Co-Precipitation Method for the Synthesis of Apatite-Type Lanthanum Silicate as an Electrolyte in SOFC, *J. Alloys Compd.*, 2017, **723**, 418–424.

252 O. Porat, C. Heremans and H. Tuller, Stability and Mixed Ionic Electronic Conduction in $Gd_2(Ti_{1-x}Mo_x)_2O_7$ under Anodic Conditions, *Solid State Ionics*, 1997, **94**, 75–83.

253 M. J. Iqbal and M. N. Ashiq, Physical and Electrical Properties of Zr–Cu Substituted Strontium Hexaferrite Nanoparticles Synthesized by Co-Precipitation Method, *Chem. Eng. J.*, 2008, **136**, 383–389.

254 C. Herring, Effect of Change of Scale on Sintering Phenomena, *J. Appl. Phys.*, 1950, **21**, 301–303.

255 G. Christie and F. Van Berkel, Microstructure—Ionic Conductivity Relationships in Ceria-Gadolinia Electrolytes, *Solid State Ionics*, 1996, **83**, 17–27.

256 C. C. Keong, Y. S. Vivek, B. Salamatinia and B. A. Horri, *Green Synthesis of Zno Nanoparticles by an Alginate Mediated Ion-Exchange Process and a Case Study for Photocatalysis of Methylene Blue Dye*, Journal of Physics: Conference Series, IOP Publishing, 2017, p. 012014.

257 C. K. Choo, T. L. Goh, L. Shahcheraghi, G. C. Ngoh, A. Z. Abdullah, B. Amini Horri and B. Salamatinia, Synthesis and Characterization of Nio Nano-Spheres by Templating on Chitosan as a Green Precursor, *J. Am. Ceram. Soc.*, 2016, **99**, 3874–3882.

258 T. Andelman, S. Gordonov, G. Busto, P. V. Moghe and R. E. Riman, Synthesis and Cytotoxicity of $Y_2O_3$ Nanoparticles of Various Morphologies, *Nanoscale Res. Lett.*, 2010, **5**, 263–273.

259 Y. T. Foo, A. Z. Abdullah, B. A. Horri and B. Salamatinia, Synthesis and Characterisation of $Y_2O_3$ Using Ammonia Oxalate as a Precipitant in Distillate Pack Co-Precipitation Process, *Ceram. Int.*, 2018, **44**, 18693–18702.

260 R. Mann, K. Laishram and N. Malhan, Synthesis of Highly Sinterable Neodymium Ion Doped Yttrium Oxide Nanopowders by Microwave Assisted Nitrate-Alanine Gel Combustion, *Trans. Indian Ceram. Soc.*, 2011, **70**, 87–91.

261 Q. Tang, H. Shen, J. Jiao and W. Chen, Microwave-Assisted Synthesis of Erbium-Doped Yttrium Oxide Nanoparticles

and Their Upconversion Properties, *Micro Nano Lett.*, 2015, **10**, 40–44.

262 N. Takahashi, A. Gubarevich, J. Sakurai, S. Hata, T. Tsuge, Y. Kitamoto, Y. Yamazaki, O. Odawara and H. Wada, *Preparation and Optical Properties of Rare Earth Doped $Y_2O_3$ Nanoparticles Synthesized by Thermal Decomposition with Oleic Acid, Advanced Materials Research,* Trans Tech Publ, 2011, pp. 1974–1978.

263 X. Sun, A. Tok, F. Boey, C. Gan and M. Schreyer, Solvent and Plasma Gas Influence on the Synthesis of $Y_2O_3$ Nanoparticles by Suspension Plasma Spraying, *J. Mater. Res.*, 2007, **22**, 1306–1313.

264 G. Dhamale, A. Tak, V. Mathe and S. Ghorui, Nucleation and Growth of $Y_2O_3$ Nanoparticles in a RF-ICTP Reactor: A Discrete Sectional Study Based on CFD Simulation Supported with Experiments, *J. Phys. D: Appl. Phys.*, 2018, **51**, 255202.

265 G. Dezanneau, C. Estournès and C. Bogicevic, Influence of Synthesis Route and Composition on Electrical Properties of $La_{9.33+x}Si_6O_{26+3x/2}$ oxy-Apatite Compounds, *Solid State Ionics*, 2008, **179**, 1929–1939.

266 A. Tarancón, G. Dezanneau, J. Arbiol, F. Peiró and J. Morante, Synthesis of Nanocrystalline Materials for SOFC Applications by Acrylamide Polymerisation, *J. Power Sources*, 2003, **118**, 256–264.

267 R. Raza, G. Abbas, X. Wang, Y. Ma and B. Zhu, Electrochemical Study of the Composite Electrolyte Based on Samaria-Doped Ceria and Containing Yttria as a Second Phase, *Solid State Ionics*, 2011, **188**, 58–63.

268 S. Jo, B. Sharma, D.-H. Park and J.-H. Myung, Materials and Nano-Structural Processes for Use in Solid Oxide Fuel Cells: A Review, *J. Korean Ceram. Soc.*, 2020, **57**, 135–151.

269 L. Fan, B. Zhu, P.-C. Su and C. He, Nanomaterials and Technologies for Low Temperature Solid Oxide Fuel Cells: Recent Advances, Challenges and Opportunities, *Nano Energy*, 2018, **45**, 148–176.

270 C.-C. Chao, Y. B. Kim and F. B. Prinz, Surface Modification of Yttria-Stabilized Zirconia Electrolyte by Atomic Layer Deposition, *Nano Lett.*, 2009, **9**, 3626–3628.

271 E. O. Oh, C. M. Whang, Y. R. Lee, S. Y. Park, D. H. Prasad, K. J. Yoon, J. W. Son, J. H. Lee and H. W. Lee, Extremely Thin Bilayer Electrolyte for Solid Oxide Fuel Cells (SOFCs) Fabricated by Chemical Solution Deposition (CSD), *Adv. Mater.*, 2012, **24**, 3373–3377.

272 D. Rubio, C. Suciu, I. Waernhus, A. Vik and A. C. Hoffmann, Tape Casting of Lanthanum Chromite for Solid Oxide Fuel Cell Interconnects, *J. Mater. Process. Technol.*, 2017, **250**, 270–279.

273 L. Mahmud, A. Muchtar and M. Somalu, Challenges in Fabricating Planar Solid Oxide Fuel Cells: A Review, *Renewable Sustainable Energy Rev.*, 2017, **72**, 105–116.

274 F. C. Krebs, Fabrication and Processing of Polymer Solar Cells: A Review of Printing and Coating Techniques, *Sol. Energy Mater. Sol. Cells*, 2009, **93**, 394–412.

275 H. Tikkanen, C. Suciu, I. Wærnhus and A. C. Hoffmann, Dip-Coating of 8YSZ Nanopowder for SOFC Applications, *Ceram. Int.*, 2011, **37**, 2869–2877.

276 M. R. Somalu, A. Muchtar, W. R. W. Daud and N. P. Brandon, Screen-Printing Inks for the Fabrication of Solid Oxide Fuel Cell Films: A Review, *Renewable Sustainable Energy Rev.*, 2017, **75**, 426–439.

277 H.-W. Lin, C.-P. Chang, W.-H. Hwu and M.-D. Ger, The Rheological Behaviors of Screen-Printing Pastes, *J. Mater. Process. Technol.*, 2008, **197**, 284–291.

278 S. Thibert, J. Jourdan, B. Bechevet, D. Chaussy, N. Reverdy-Bruas and D. Beneventi, Influence of Silver Paste Rheology and Screen Parameters on the Front Side Metallization of Silicon Solar Cell, *Mater. Sci. Semicond. Process.*, 2014, **27**, 790–799.

279 M. R. Somalu and N. P. Brandon, Rheological Studies of Nickel/Scandia-Stabilized-Zirconia Screen Printing Inks for Solid Oxide Fuel Cell Anode Fabrication, *J. Am. Ceram. Soc.*, 2012, **95**, 1220–1228.

280 R. Rudež, J. Pavlič and S. Bernik, Preparation and Influence of Highly Concentrated Screen-Printing Inks on the Development and Characteristics of Thick-Film Varistors, *J. Eur. Ceram. Soc.*, 2015, **35**, 3013–3023.

281 P. Von Dollen and S. Barnett, A Study of Screen Printed Yttria-Stabilized Zirconia Layers for Solid Oxide Fuel Cells, *J. Am. Ceram. Soc.*, 2005, **88**, 3361–3368.

282 F. Lefebvre-Joud, G. Gauthier and J. Mougin, Current Status of Proton-Conducting Solid Oxide Fuel Cells Development, *J. Appl. Electrochem.*, 2009, **39**, 535–543.

283 D. Marani, C. Gadea, J. Hjelm, P. Hjalmarsson, M. Wandel and R. Kiebach, Influence of Hydroxyl Content of Binders on Rheological Properties of Cerium–Gadolinium Oxide (CGO) Screen Printing Inks, *J. Eur. Ceram. Soc.*, 2015, **35**, 1495–1504.

284 P. Ried, C. Lorenz, A. Brönstrup, T. Graule, N. H. Menzler, W. Sitte and P. Holtappels, Processing of YSZ Screen Printing Pastes and the Characterization of the Electrolyte Layers for Anode Supported SOFC, *J. Eur. Ceram. Soc.*, 2008, **28**, 1801–1808.

285 J. W. Phair, M. Lundberg and A. Kaiser, Leveling and Thixotropic Characteristics of Concentrated Zirconia Inks for Screen-Printing, *Rheol. Acta*, 2009, **48**, 121–133.

286 M. R. Somalu, *Fabrication and Characterization of Ni/Scsz Cermet Anodes for Intermediate Temperature SOFCs*, Imperial College, London, 2012.

287 X. Ge, X. Huang, Y. Zhang, Z. Lu, J. Xu, K. Chen, D. Dong, Z. Liu, J. Miao and W. Su, Screen-Printed Thin YSZ Films Used as Electrolytes for Solid Oxide Fuel Cells, *J. Power Sources*, 2006, **159**, 1048–1050.

288 Y. Zhang, X. Huang, Z. Lu, Z. Liu, X. Ge, J. Xu, X. Xin, X. Sha and W. Su, A Study of the Process Parameters for Yttria-Stabilized Zirconia Electrolyte Films Prepared by Screen-Printing, *J. Power Sources*, 2006, **160**, 1065–1073.

289 J. W. Phair, Rheological Analysis of Concentrated Zirconia Pastes with Ethyl Cellulose for Screen Printing SOFC Electrolyte Films, *J. Am. Ceram. Soc.*, 2008, **91**, 2130–2137.

290 R. Mücke, O. Büchler, N. Menzler, B. Lindl, R. Vaßen and H. Buchkremer, High-Precision Green Densities of Thick Films and Their Correlation with Powder, Ink, and Film Properties, *J. Eur. Ceram. Soc.*, 2014, **34**, 3897–3916.

291 A. Nascimento, R. Basaglia, F. Cunha, C. Fonseca, M. Brant, T. Matencio and R. Domingues, Correlation between Yttria Stabilized Zirconia Particle Size and Morphological Properties of Nio–YSZ Films Prepared by Spray Coating Process, *Ceram. Int.*, 2009, **35**, 3421–3425.

292 W. J. Tseng and C.-N. Chen, Effect of Polymeric Dispersant on Rheological Behavior of Nickel–Terpineol Suspensions, *Mater. Sci. Eng., A*, 2003, **347**, 145–153.

293 C. Xia, F. Chen and M. Liu, Reduced-Temperature Solid Oxide Fuel Cells Fabricated by Screen Printing, *Electrochem. Solid-State Lett.*, 2001, **4**, A52.

294 J. Fergus, R. Hui, X. Li, D. P. Wilkinson and J. Zhang, *Solid Oxide Fuel Cells: Materials Properties and Performance*, CRC Press, 2016.

295 D. Beckel, A. Bieberle-Hütter, A. Harvey, A. Infortuna, U. P. Muecke, M. Prestat, J. L. Rupp and L. J. Gauckler, Thin Films for Micro Solid Oxide Fuel Cells, *J. Power Sources*, 2007, **173**, 325–345.

296 X. Xu, C. Xia, S. Huang and D. Peng, YSZ Thin Films Deposited by Spin-Coating for IT-SOFCs, *Ceram. Int.*, 2005, **31**, 1061–1064.

297 J. Wang, Z. Lü, K. Chen, X. Huang, N. Ai, J. Hu, Y. Zhang and W. Su, Study of Slurry Spin Coating Technique Parameters for the Fabrication of Anode-Supported YSZ Films for SOFCs, *J. Power Sources*, 2007, **164**, 17–23.

298 M. Chen, B. H. Kim, Q. Xu, B. G. Ahn and D. P. Huang, Fabrication and Performance of Anode-Supported Solid Oxide Fuel Cells Via Slurry Spin Coating, *J. Membr. Sci.*, 2010, **360**, 461–468.

299 H. J. Kim, M. Kim, K. C. Neoh, G. D. Han, K. Bae, J. M. Shin, G.-T. Kim and J. H. Shim, Slurry Spin Coating of Thin Film Yttria Stabilized Zirconia/Gadolinia Doped Ceria Bi-Layer Electrolytes for Solid Oxide Fuel Cells, *J. Power Sources*, 2016, **327**, 401–407.

300 Z. Wang, K. Sun, S. Shen, N. Zhang, J. Qiao and P. Xu, Preparation of YSZ Thin Films for Intermediate Temperature Solid Oxide Fuel Cells by Dip-Coating Method, *J. Membr. Sci.*, 2008, **320**, 500–504.

301 S.-D. Kim, J.-J. Lee, H. Moon, S.-H. Hyun, J. Moon, J. Kim and H.-W. Lee, Effects of Anode and Electrolyte Microstructures on Performance of Solid Oxide Fuel Cells, *J. Power Sources*, 2007, **169**, 265–270.

302 B. Bitterlich, C. Lutz and A. Roosen, Rheological Characterization of Water-Based Slurries for the Tape Casting Process, *Ceram. Int.*, 2002, **28**, 675–683.

303 T. Baquero, J. Escobar, J. Frade and D. Hotza, Aqueous Tape Casting of Micro and Nano YSZ for SOFC Electrolytes, *Ceram. Int.*, 2013, **39**, 8279–8285.

304 J. Will, A. Mitterdorfer, C. Kleinlogel, D. Perednis and L. Gauckler, Fabrication of Thin Electrolytes for Second-Generation Solid Oxide Fuel Cells, *Solid State Ionics*, 2000, **131**, 79–96.

305 C. Fu, X. Ge, S. Chan and Q. Liu, Fabrication and Characterization of Anode-Supported Low-Temperature SOFC Based on Gd-Doped Ceria Electrolyte, *Fuel Cells*, 2012, **12**, 450–456.

306 P. Coddet, H.-l Liao and C. Coddet, A Review on High Power SOFC Electrolyte Layer Manufacturing Using Thermal Spray and Physical Vapour Deposition Technologies, *Adv. Manuf.*, 2014, **2**, 212–221.

307 Y. Hong, S. Kim, W. Kim and H. Yoon, Fabrication and Characterization GDC Electrolyte Thin Films by E-Beam Technique for IT-SOFC, *Curr. Appl. Phys.*, 2011, **11**, S163–S168.

308 G. Laukaitis, J. Dudonis and D. Milcius, YSZ Thin Films Deposited by E-Beam Technique, *Thin Solid Films*, 2006, **515**, 678–682.

309 M. K. Baig, S. Atiq, S. Bashir, S. Riaz, S. Naseem, H. Soleimani and N. Yahya, Pulsed Laser Deposition of Smco Thin Films for Mems Applications, *J. Appl. Res. Technol.*, 2016, **14**, 287–292.

310 Y.-L. Kuo, Y.-S. Chen and C. Lee, Growth of 20 mol% Gd-Doped Ceria Thin Films by RF Reactive Sputtering: The $O_2$/Ar Flow Ratio Effect, *J. Eur. Ceram. Soc.*, 2011, **31**, 3127–3135.

311 L. Wang and S. Barnett, Sputter-Deposited Medium-Temperature Solid Oxide Fuel Cells with Multi-Layer Electrolytes, *Solid State Ionics*, 1993, **61**, 273–276.

312 E. Rezugina, A.-L. Thomann, H. Hidalgo, P. Brault, V. Dolique and Y. Tessier, Ni-YSZ Films Deposited by Reactive Magnetron Sputtering for SOFC Applications, *Surf. Coat. Technol.*, 2010, **204**, 2376–2380.

313 K. Hayashi, O. Yamamoto, Y. Nishigaki and H. Minoura, Sputtered $La_{0.5}Sr_{0.5}MnO_3$–Yttria Stabilized Zirconia Composite Film Electrodes for SOFC, *Solid State Ionics*, 1997, **98**, 49–55.

314 S. Hong, D. Lee, Y. Lim, J. Bae and Y.-B. Kim, Yttria-Stabilized Zirconia Thin Films with Restrained Columnar Grains for Oxygen Ion Conducting Electrolytes, *Ceram. Int.*, 2016, **42**, 16703–16709.

315 A. Nagata and H. Okayama, Characterization of Solid Oxide Fuel Cell Device Having a Three-Layer Film Structure Grown by RF Magnetron Sputtering, *Vacuum*, 2002, **66**, 523–529.

316 K. Sasaki, M. Muranaka, A. Suzuki and T. Terai, Synthesis and Characterization of Lsgm Thin Film Electrolyte by RF Magnetron Sputtering for LT-SOFCs, *Solid State Ionics*, 2008, **179**, 1268–1272.

317 M. Vieira, J. Oliveira, A. Shaula, A. Cavaleiro and B. Trindade, Lanthanum Silicate Thin Films for SOFC Electrolytes Synthesized by Magnetron Sputtering and Subsequent Annealing, *Surf. Coat. Technol.*, 2012, **206**, 3316–3322.

318 J. H. Joo and G. M. Choi, Electrical Conductivity of YSZ Film Grown by Pulsed Laser Deposition, *Solid State Ionics*, 2006, **177**, 1053–1057.

319 R. Eason, *Pulsed Laser Deposition of Thin Films: Applications-Led Growth of Functional Materials*, John Wiley & Sons, 2007.

320 H. M. Christen and G. Eres, Recent Advances in Pulsed-Laser Deposition of Complex Oxides, *J. Phys.: Condens. Matter*, 2008, **20**, 264005.

321 F. Saporiti, R. Juarez, F. Audebert and M. Boudard, Yttria and Ceria Doped Zirconia Thin Films Grown by Pulsed Laser Deposition, *Mater. Res.*, 2013, **16**, 655–660.

322 X.-F. Ding, J.-Y. Shen, X.-J. Gao and J. Wang, Enhanced Electrochemical Properties of $Sm_{0.2}Ce_{0.8}O_{1.9}$ Film for SOFC Electrolyte Fabricated by Pulsed Laser Deposition, *Rare Met.*, 2021, **40**, 1294–1299.

323 N. Shaigan, W. Qu, D. G. Ivey and W. Chen, A Review of Recent Progress in Coatings, Surface Modifications and Alloy Developments for Solid Oxide Fuel Cell Ferritic Stainless Steel Interconnects, *J. Power Sources*, 2010, **195**, 1529–1542.

324 D. A. Glocker, S. I. Shah and C. A. Morgan, *Handbook of Thin Film Process Technology*, Institute of Physics Bristol, 1995, vol. 2.

325 K.-W. Chour, J. Chen and R. Xu, Metal-Organic Vapor Deposition of YSZ Electrolyte Layers for Solid Oxide Fuel Cell Applications, *Thin Solid Films*, 1997, **304**, 106–112.

326 N. Gelfond, O. Bobrenok, M. Predtechensky, N. Morozova, K. Zherikova and I. Igumenov, Chemical Vapor Deposition of Electrolyte Thin Films Based on Yttria-Stabilized Zirconia, *Inorg. Mater.*, 2009, **45**, 659–665.

327 E. Hermawan, G. S. Lee, G. S. Kim, H. C. Ham, J. Han and S. P. Yoon, Densification of an YSZ Electrolyte Layer Prepared by Chemical/Electrochemical Vapor Deposition for Metal-Supported Solid Oxide Fuel Cells, *Ceram. Int.*, 2017, **43**, 10450–10459.

328 J. D. Baek, K.-Y. Liu and P.-C. Su, A Functional Micro-Solid Oxide Fuel Cell with a 10 N m-Thick Freestanding Electrolyte, *J. Mater. Chem. A*, 2017, **5**, 18414–18419.

329 E. Gourba, A. Ringuede, M. Cassir, A. Billard, J. Päiväsaari, J. Niinistö, M. Putkonen and L. Niinistö, Characterisation of Thin Films of Ceria-Based Electrolytes for Intermediatetemperature—Solid Oxide Fuel Cells (IT-SOFC), *Ionics*, 2003, **9**, 15–20.

330 W. Schafbauer, N. H. Menzler and H. P. Buchkremer, Tape Casting of Anode Supports for Solid Oxide Fuel Cells at Forschungszentrum Jülich, *Int. J. Appl. Ceram. Technol.*, 2014, **11**, 125–135.

331 C. Ye, S. Bi, P. Liao, Y. Huang, X. Lin, Y. Wang, L. Zhang and J.-Q. Wang, Rational Design of NiO-8YSZ Screen-Printing Slurry for High-Performance Large-Area Solid Oxide Cells, *J. Phys. Chem. C*, 2023, **127**, 6629–6637.

332 Z. Tan and T. Ishihara, Redox Stability of Tubular Solid Oxide Cell Using $LaGaO_3$ Electrolyte Film Prepared by Dip-Coating, *ECS Trans.*, 2021, **103**, 1685.

333 S. Zhang, L. Bi, L. Zhang, C. Yang, H. Wang and W. Liu, Fabrication of Cathode Supported Solid Oxide Fuel Cell by Multi-Layer Tape Casting and Co-Firing Method, *Int. J. Hydrogen Energy*, 2009, **34**, 7789–7794.

334 X. Chen, H. Zhang, Y. Li, J. Xing, Z. Zhang, X. Ding, B. Zhang, J. Zhou and S. Wang, Fabrication and Performance of Anode-Supported Proton Conducting Solid Oxide Fuel Cells Based on $BaZr_{0.1}Ce_{0.7}Y_{0.1}Yb_{0.1}O_{3-\Delta}$ Electrolyte by Multi-Layer Aqueous-Based Co-Tape Casting, *J. Power Sources*, 2021, **506**, 229922.

335 P. Coddet, M. C. Pera and A. Billard, Planar Solid Oxide Fuel Cell: Electrolyte Deposited by Reactive Magnetron Sputtering and Cell Test, *Fuel Cells*, 2011, **11**, 158–164.

336 H. Y. Jung, K.-S. Hong, H. Kim, J.-K. Park, J.-W. Son, J. Kim, H.-W. Lee and J.-H. Lee, Characterization of Thin-Film YSZ Deposited Via EB-PVD Technique in Anode-Supported SOFCs, *J. Electrochem. Soc.*, 2006, **153**, A961.

337 F. Han, M. Riegraf, N. Sata, I. Bombarda, T. Liensdorf, C. Sitzmann, N. Langhof, S. Schafföner, C. Walter and C. Geipel, Properties and Performance of Electrolyte Supported SOFCs with Eb-Pvd Gd-Doped Ceria Thin-Films, *ECS Trans.*, 2021, **103**, 139.

338 T. H. Shin, M. Shin, G.-W. Park, S. Lee, S.-K. Woo and J. Yu, Fabrication and Characterization of Oxide Ion Conducting Films, $Zr_{1-x}M_xO_{2-\Delta}$ (M = Y, Sc) on Porous SOFC Anodes, Prepared by Electron Beam Physical Vapor Deposition, *Sustainable Energy Fuels*, 2017, **1**, 103–111.

339 S. Majhi, S. Behura, S. Bhattacharjee, B. Singh, T. Chongdar, N. Gokhale and L. Besra, Anode Supported Solid Oxide Fuel Cells (SOFC) by Electrophoretic Deposition, *Int. J. Hydrogen Energy*, 2011, **36**, 14930–14935.

340 J. H. Shim, C.-C. Chao, H. Huang and F. B. Prinz, Atomic Layer Deposition of Yttria-Stabilized Zirconia for Solid Oxide Fuel Cells, *Chem. Mater.*, 2007, **19**, 3850–3854.

341 S. A. Kumar, P. Kuppusami, S. Amirthapandian and Y.-P. Fu, Effect of Sm Co-Doping on Structural, Mechanical and Electrical Properties of Gd Doped Ceria Solid Electrolytes for Intermediate Temperature Solid Oxide Fuel Cells, *Int. J. Hydrogen Energy*, 2020, **45**, 29690–29704.

342 M. Y. Shah, Z. Tayyab, S. Rauf, M. Yousaf, N. Mushtaq, M. A. Imran, P. D. Lund, M. I. Asghar and B. Zhu, Interface Engineering of Bi-Layer Semiconductor $SrCoSnO_{3-\Delta}$–$CeO_{2-\Delta}$ Heterojunction Electrolyte for Boosting the Electrochemical Performance of Low-Temperature Ceramic Fuel Cell, *Int. J. Hydrogen Energy*, 2021, **46**, 33969–33977.

343 Y. Gao, L. Huang, B. Zhang, J. Gao, C.-J. Li and C.-X. Li, Enhanced Sintering Ability and Electrochemical Performance of $Gd_{0.1}Ce_{0.9}O_{1.95}$ Composited with $(Dy_{0.2}Zr_{0.05}Bi_{0.75})_2O_3$ for Low-Temperature Solid Oxide Fuel Cells, *Electrochim. Acta*, 2024, **475**, 143614.

344 C. Gaudillere, L. Navarrete and J. M. Serra, Syngas Production at Intermediate Temperature through $H_2O$ and $CO_2$ Electrolysis with a Cu-Based Solid Oxide Electrolyzer Cell, *Int. J. Hydrogen Energy*, 2014, **39**, 3047–3054.

345 A. Mahmood, S. Bano, J. H. Yu and K.-H. Lee, High-Performance Solid Oxide Electrolysis Cell Based on ScSZ/GDC (Scandia-Stabilized Zirconia/Gadolinium-Doped Ceria) Bi-Layered Electrolyte and LSCF (Lanthanum Strontium Cobalt Ferrite) Oxygen Electrode, *Energy*, 2015, **90**, 344–350.

346 S. Choi, C. J. Kucharczyk, Y. Liang, X. Zhang, I. Takeuchi, H.-I. Ji and S. M. Haile, Exceptional Power Density and Stability at Intermediate Temperatures in Protonic Ceramic Fuel Cells, *Nat. Energy*, 2018, **3**, 202–210.

347 D.-H. Myung, J. Hong, K. Yoon, B.-K. Kim, H.-W. Lee, J.-H. Lee and J.-W. Son, The Effect of an Ultra-Thin Zirconia Blocking Layer on the Performance of a 1-Mm-Thick

Gadolinia-Doped Ceria Electrolyte Solid-Oxide Fuel Cell, *J. Power Sources*, 2012, **206**, 91–96.

348 J.-Y. Park and E. D. Wachsman, Stable and High Conductivity Ceria/Bismuth Oxide Bilayer Electrolytes for Lower Temperature Solid Oxide Fuel Cells, *Ionics*, 2006, **12**, 15–20.

349 J. S. Ahn, D. Pergolesi, M. A. Camaratta, H. Yoon, B. W. Lee, K. T. Lee, D. W. Jung, E. Traversa and E. D. Wachsman, High-Performance Bilayered Electrolyte Intermediate Temperature Solid Oxide Fuel Cells, *Electrochem. Commun.*, 2009, **11**, 1504–1507.

350 S. R. Hui, J. Roller, S. Yick, X. Zhang, C. Decès-Petit, Y. Xie, R. Maric and D. Ghosh, A Brief Review of the Ionic Conductivity Enhancement for Selected Oxide Electrolytes, *J. Power Sources*, 2007, **172**, 493–502.

351 O. T. Sørensen, *Nonstoichiometric Oxides*, Elsevier, 2012.

352 S. V. Fedorov, M. S. Sedov and V. V. Belousov, Functionally Graded IT-MOFC Electrolytes Based on Highly Conductive $\Delta$-$Bi_2O_3$–0.2 wt% $B_2O_3$ Composite with Molten Grain Boundaries, *ACS Appl. Energy Mater.*, 2019, **2**, 6860–6865.

353 L. Miao, J. Hou, K. Dong and W. Liu, A Strategy for Improving the Sinterability and Electrochemical Properties of Ceria-Based LT-SOFCs Using Bismuth Oxide Additive, *Int. J. Hydrogen Energy*, 2019, **44**, 5447–5453.

354 H. Ding, T. Wu, S. Zhao, H. Sun, J. Li, X. Guo and P. Wang, Grain Boundary Conduction Behaviors of Ultra-Fine Grained $CeO_2$/$BaCeO_3$ Based Electrolytes, *Ceram. Int.*, 2022, **48**, 25314–25321.

355 R. Maric, S. Seward, P. W. Faguy and M. Oljaca, Electrolyte Materials for Intermediate Temperature Fuel Cells Produced Via Combustion Chemical Vapor Condensation, *Electrochem. Solid-State Lett.*, 2003, **6**, A91.

356 S. Ryu, I. W. Choi, Y. J. Kim, S. Lee, W. Jeong, W. Yu, G. Y. Cho and S. W. Cha, Nanocrystal Engineering of Thin-Film Yttria-Stabilized Zirconia Electrolytes for Low-Temperature Solid-Oxide Fuel Cells, *ACS Appl. Mater. Interfaces*, 2023, **15**, 42659–42666.

357 H. Li, *et al.*, Ampere-Hour-Scale Soft-Package Potassium-Ion Hybrid Capacitors Enabling 6-Minute Fast-Charging, *Nat. Commun.*, 2023, **14**, 6407.

358 A. Akbari-Fakhrabadi, R. Mangalaraja, M. Jamshidijam, S. Ananthakumar and S. Chan, Mechanical Properties of Gd–$CeO_2$ Electrolyte for SOFC Prepared by Aqueous Tape Casting, *Fuel Cells*, 2013, **13**, 682–688.

359 J. Antunes, A. Cavaleiro, L. Menezes, M. Simoes and J. Fernandes, Ultra-Microhardness Testing Procedure with Vickers Indenter, *Surf. Coat. Technol.*, 2002, **149**, 27–35.

360 M. Santos, C. Alves, F. A. C. Oliveira, T. Marcelo, J. Mascarenhas, J. Fernandes and B. Trindade, Mechanical Properties of Sintered $La_{9.33}Si_2Ge_4O_{26}$ Oxyapatite Materials for SOFC Electrolytes, *Ceram. Int.*, 2012, **38**, 6151–6156.

361 X. Xiong, K. Liang, G. Ma and L. Ba, Three-Dimensional Multi-Physics Modelling and Structural Optimization of SOFC Large-Scale Stack and Stack Tower, *Int. J. Hydrogen Energy*, 2023, **48**, 2742–2761.

362 J. Ma, S. Ma, X. Zhang, D. Chen and J. He, Development of Large-Scale and Quasi Multi-Physics Model for Whole Structure of the Typical Solid Oxide Fuel Cell Stacks, *Sustainability*, 2018, **10**, 3094.

363 C. Gong, X. Luo and Z. Tu, Thermal Management of Bypass Valves for Temperature Difference Elimination in a 5 kW Multi-Stack Solid Oxide Fuel Cell System, *Appl. Therm. Eng.*, 2023, **229**, 120590.

364 N. Christiansen, J. B. Hansen, H. H. Larsen, S. Linderoth, P. H. Larsen, P. V. Hendriksen and A. Hagen, Solid Oxide Fuel Cell Development at Topsoe Fuel Cell A/S and Risø National Laboratory, *ECS Trans.*, 2007, **7**, 31.

365 D. Chen, Y. Xu, B. Hu, C. Yan and L. Lu, Investigation of Proper External Air Flow Path for Tubular Fuel Cell Stacks with an Anode Support Feature, *Energy Convers. Manage.*, 2018, **171**, 807–814.

366 Y. Zheng, T. Chen, Q. Li, W. Wu, H. Miao, C. Xu and W. Wang, Achieving 360 N L $h^{-1}$ Hydrogen Production Rate through 30-Cell Solid Oxide Electrolysis Stack with LSCF–GDC Composite Oxygen Electrode, *Fuel Cells*, 2014, **14**, 1066–1070.

367 C. M. Stoots, J. E. O'Brien, K. G. Condie and J. J. Hartvigsen, High-Temperature Electrolysis for Large-Scale Hydrogen Production from Nuclear Energy–Experimental Investigations, *Int. J. Hydrogen Energy*, 2010, **35**, 4861–4870.

368 L. Blum, S. M. Groß, J. Malzbender, U. Pabst, M. Peksen, R. Peters and I. C. Vinke, Investigation of Solid Oxide Fuel Cell Sealing Behavior under Stack Relevant Conditions at Forschungszentrum Jülich, *J. Power Sources*, 2011, **196**, 7175–7181.

369 Y. Choi, S. Byun, D. W. Seo, H. J. Hwang, T. W. Kim and S.-D. Kim, New Design and Performance Evaluation of 1 kW-Class Reversible Solid Oxide Electrolysis-Fuel Cell Stack Using Flat-Tubular Cells, *J. Power Sources*, 2022, **542**, 231744.

370 V. Subotić, A. Baldinelli, L. Barelli, R. Scharler, G. Pongratz, C. Hochenauer and A. Anca-Couce, Applicability of the SOFC Technology for Coupling with Biomass-Gasifier Systems: Short-and Long-Term Experimental Study on SOFC Performance and Degradation Behaviour, *Appl. Energy*, 2019, **256**, 113904.

371 F. Tietz, D. Sebold, A. Brisse and J. Schefold, Degradation Phenomena in a Solid Oxide Electrolysis Cell after 9000 h of Operation, *J. Power Sources*, 2013, **223**, 129–135.

372 Q. Fang, L. Blum and N. H. Menzler, Performance and Degradation of Solid Oxide Electrolysis Cells in Stack, *J. Electrochem. Soc.*, 2015, **162**, F907.

373 B. Königshofer, P. Boškoski, G. Nusev, M. Koroschetz, M. Hochfellner, M. Schwaiger, Đ. Juričić, C. Hochenauer and V. Subotić, Performance Assessment and Evaluation of Soc Stacks Designed for Application in a Reversible Operated 150 kW rSOC Power Plant, *Appl. Energy*, 2021, **283**, 116372.